INFORMATION TO USERS

This manuscript has been reproduced from the microfilm master. UMI films the text directly from the original or copy submitted. Thus, some thesis and dissertation copies are in typewriter face, while others may be from any type of computer printer.

The quality of this reproduction is dependent upon the quality of the copy submitted. Broken or indistinct print, colored or poor quality illustrations and photographs, print bleedthrough, substandard margins, and improper alignment can adversely affect reproduction.

In the unlikely event that the author did not send UMI a complete manuscript and there are missing pages, these will be noted. Also, if unauthorized copyright material had to be removed, a note will indicate the deletion.

Oversize materials (e.g., maps, drawings, charts) are reproduced by sectioning the original, beginning at the upper left-hand corner and continuing from left to right in equal sections with small overlaps. Each original is also photographed in one exposure and is included in reduced form at the back of the book.

Photographs included in the original manuscript have been reproduced xerographically in this copy. Higher quality 6" x 9" black and white photographic prints are available for any photographs or illustrations appearing in this copy for an additional charge. Contact UMI directly to order.

UMI®

Bell & Howell Information and Learning
300 North Zeeb Road, Ann Arbor, MI 48106-1346 USA
800-521-0600

Stochastic models for surface adsorption and reaction processes

by

Edna Wright James

A dissertation submitted to the graduate faculty

in partial fulfillment of the requirements for the degree of

DOCTOR OF PHILOSOPHY

Major: Applied Mathematics

Major Professor: James W. Evans

Iowa State University

Ames, Iowa

1999

Graduate College

Iowa State University

This is to certify that the Doctoral dissertation of

Edna Wright James

has met the dissertation requirements of Iowa State University

Signature was redacted for privacy.

Committee Member

Signature was redacted for privacy.

Committee Member

Signature was redacted for privacy.

Committee Member

Signature was redacted for privacy.

Committee Member

Signature was redacted for privacy.

Major Professor

Signature was redacted for privacy.

For the Major Program

Signature was redacted for privacy.

For the Graduate College

To: Mimi & Didi:
Ever my inspiration and shining
example.
Thank you, for your loving care
of
my daughter Farrah and
my sons Hewlett & Fractals;
for your boundless generosity &
patience;
for your helpful guidance; but
most of all,
for being you.

Ah-luh-Bee!!

♥

TABLE OF CONTENTS

CHAPTER 1. INTRODUCTION

General Background

In the Statistical Mechanics community, there has long been interest in so called Lattice-Gas Models wherein particles (atoms, molecules) occupy some distribution of sites on a periodic lattice [1]. Originally, interest focused on equilibrium systems where the energy of various configurations is described by a Hamiltonian, H, and the probability, P, that the system is in some state is given by the Gibb's formula, $P \propto e^{-\beta H}$, where $\beta = \frac{1}{k_B T}$. Here, k_B is Boltzmann's constant, and T is the system temperature. In these studies, a phenomenon of primary interest is the occurrence of "phase transitions" where the state of the system changes in some non-analytic way as some parameter is varied. There is also a long history of analysis of the approach to this equilibrium state of systems "slightly perturbed" from equilibrium [2]. In these studies of time evolution, the rates which describe transitions between different configurations must satisfy a detailed-balance condition to be consistent with H, and the dynamics is stochastic. In the models considered in the above studies, the particles arranged on a periodic array of sites have most commonly represented atoms or magnetic spins in a crystalline solid, or atoms or molecules adsorbed on a crystalline surface.

More recently, attention has shifted to the time evolution of lattice-gas systems far-from-equilibrium, and often for models where the long-time "equilibrium" or steady state cannot be described by the Gibb's formula, the rates do not necessarily satisfy detailed-balance condition [3]. Such models have a diverse array of applications beyond those

mentioned above, to such areas as population dynamics, the spread of information or disease, reactive systems, and etc.

A parallel effort was initiated in the Probability community, or more specifically the Mathematical Statistics community, starting in the late 1960's. This was motivated by the classical statistical mechanical problems involving Hamiltonian systems, but soon was extended to consider non-Hamiltonian or far-from-equilibrium systems of the type described in the above paragraph. In this community, such models are called Interacting (or Infinite) Particle Systems, rather than lattice-gas models [4].

Lattice-Gas Models for Surface Reactions and their Usefulness

Not only can these models be used to try to explain real-life problems posed in surface chemistry, and catalysis, but they display interesting mathematical characteristics as well: the non-integer dimension and the self-similarity of fractal objects; and the "rich nonlinear dynamics [such as] multi-stability, self-sustained oscillations, and chaos...."[5] found in the stochastic models, are a couple examples.

While it may be possible to write down exact equations to describe the model, these equations suffer several drawbacks:

(a) they may come in the form of an infinite and nontrivial coupled system of equations;

(b) approximations to the equations are necessary, causing the numerical solutions to be inaccurate; and

(c) even if exact solutions were possible, these solutions may only yield average spatial behavior, thus overlooking the finer details of the actual model.

We circumvent the above problems by using Monte Carlo simulations.

We use Monte Carlo simulations of suitable lattice gas models to model catalytic surface reactions. We compare our results with physical experiment to test how well the Monte Carlo simulations model reality and to elucidate the experimental findings [6]. We are also interested in the mathematical properties which can be observed from these simulations but which may not be easily seen in physical experiments.

One motivation for studying heterogenous catalysis is the need for the removal of poisonous gases such as carbon monoxide found in automobile exhaust which contribute to urban air pollution. "Even with the most careful attention to engine design and fuel characteristics, it is not possible under normal driving conditions to reduce the contents of these pollutants to an acceptable level in the exhaust gases coming from the engine." [7]. These poisonous gases are thus removed by your catalytic converter.

Modified Monomer-Dimer ($A+B_2$) Surface Reaction Model

The particular lattice-gas model studied here uses a square lattice of adsorption sites to model the metal catalytic surface. We include the following four rules in this general model:

(i) CO(gas) molecules adsorb onto the lattice at single empty sites at a rate P_{CO}. O_2(gas) dimers adsorb dissociatively at nearest neighbor (NN) sites at a rate P_{O2}. In this model, the deposition rates are related by the equation $P_{CO} + P_{O2} = 1$.

(ii) CO molecules diffuse across the lattice with an infinite hop-rate, so they are assumed to be randomly distributed over the sites not occupied by adsorbed O atoms—O(ads), for short.

(iii) The CO(ads) desorb off the lattice at a rate d. Thus, increasing d is similar to increasing the temperature in the physical experiments.

(iv) Finally, each adjacent pair of CO(ads) and O_2(ads) can react at a rate k to form CO_2(gas).

Most previous LG modeling of CO-oxidation allowed the adsorption of O_2 gas to occur on nearest neighbor sites [8–12]. Some exceptions can be found in Ref[6,13]. In order to better describe reality, our new model which we presently study imposes the following additional rule upon the deposition of O_2(gas):

(v) O_2(gas) dimers adsorb at *diagonal* NN (nearest neighbor) sites, rather than at *adjacent* NN sites. Further, this deposition may take place *only* if the *additional* six adjacent sites are not occupied by O(ads)—this is known as the 8-site model. In other words, no two O(ads) atoms may occupy adjacent NN sites.

Questions Which Naturally Arise for this Model (and their Corresponding Mathematical Context)

In the study of this model, we find several questions arise naturally, concerning the fractional coverages θ_{CO} and θ_O of CO(ads) and O(ads), respectively:

(a) What is the steady-state behavior of θ_{CO} and θ_O ? (bifurcation theory)

(b) What is the behavior of the quantities θ_{CO} and θ_O , over time? (non-linear dynamics)

(c) In what way do θ_{CO} and θ_O fluctuate about their steady-state values as time, $t\to\infty$? (stochastic dynamics)

(d) What spatial arrangements are formed by the adsorbed species? (stochastic geometry)

Some Corresponding Answers to the Above Questions

(a) In order to address the issue of steady-state behavior of coverages, we construct a steady-state bifurcation or phase diagram. It turns out that, for small d, there is a range of pressures P_{CO}, wherein the model is bistable. We observe a transition from bistability to monostability as d increases towards a critical value denoted by d_c.

(b) The fractional coverage of either CO(ads) or O(ads) fluctuates in time about its steady-state value, θ_{SS}. The amplitude of these fluctuations are proportional to $1/\sqrt{N}$, where N is the size of the lattice. Thus, in the ideal case of an infinite lattice, the coverage converges to θ_{SS}. However, since it is physically possible to model only finite lattices, these oscillatons or fluctuations never vanish completely, even as $t \rightarrow \infty$.

(c) The size, N, of the lattice is not the only parameter which affects the fluctuations in the coverages. We also observe a rapid increase in the magnitude of the fluctuations as $d \rightarrow d_c$.

(d) The intriguing spatial patterns formed by adsorbed species is one of my favorite issues. For most of the values of P_{CO}, we have found that the spatial patterns formed by O(ads) are rather sparse and/or quite random. However, as P_{CO} decreases toward zero, the corresponding deposition rate P_{O2} increases, and the

lattice tends to become jammed with O(ads) atoms. Because of the 8-site deposition rule, the O(ads) atoms tend to cluster into only one of the two possible types of "red" or "black" almost perfect checkerboard subdomains, which grow in size as $t \rightarrow \infty$.

Two New Features Resulting from Eight-Site Rule

The first new feature of our model is the *symmetry-breaking*, described in part d of the above section, which occurs for low P_{CO}. (In fact, finding the critical value of P_{CO} near zero, where this symmetry breaking starts to occur is one of the issues we address in Chapter 3.) In the old model where O-atoms were allowed to occupy NN sites, the system had no cause to favor only even or only odd sites. However, because of the 8-site rule, for high O(ads) concentration levels, our new system becomes "more comfortable" and less crowded by breaking symmetry.

Secondly, in the traditional model, for low P_{CO} and low CO(ads) concentration levels, there existed a transition point for P_{CO}, below which the system became entirely poisoned with O(ads). Ref[10]. The eight-site rule removes this difficulty, as this unrealistic feature is not present in our new model.

Dissertation Organization

This thesis is a compilation of work that either has been published, submitted for publication, or is in preparation for submission. Each paper is a separate chapter. Chapter 2 is the first of two papers, submitted to the Journal of Chemical Physics, which analyzes a simple model for CO-oxidation on surfaces, incorporating the new eight-site rule into the old

AB_2 lattice-gas model. Chapter 3 is the second part of this study, analyzing the critical phenomena of symmetry-breaking and fluctuations. This third chapter is to be submitted to the Journal of Chemical Physics. Chapter 4 is a paper, published in Physical Review Letters, which compares the model's behavior against an actual experiment. This paper constitutes a collaborative effort between an experimental and a theoretical group. Both experimental and theoretical contributions are crucial to the paper and of equal significance. James was the primary contributor to the theoretical component, and Suchorski to the experimental component. This chapter is an important component of the overall thesis as it demonstrates the practical significance of the model development in the previous two chapters. Chapter 5 is a paper, accepted for publication in a Special Issue of Colloids and Surfaces A, which explores the effect of slow relaxation processes in two models for irreversible chemisorption, and which incorporate superlattice ordering of the adsorbed layer on a square lattice of adsorption sites. In Chapter 6 are some general conclusions.

References

[1] G. M. Bell and D. A. Lavis, *Statistical Mechanics of Lattice-Gas Models* (Wiley, London, 1989)

[2] K. Binder, Mont-carlo Methods in Statistical Physics, Springer Current Topics in Physics; vol. 7 (Springer, Berlin, 1979)

[3] H.E. Stanley and N. Ostrowsky, *On Growth and Form* (Martinus Nijhoff, Dordrecht, 1986)

[4] T. M. Liggett, *Interacting Particle Systems* (Springer, Berlin, 1985)

[5] J. Evans & M. Sabella; "Mean-field, lattice-gas, and monomer-dimer surface reaction"; Trends in Stat. Phys., 1 (1994)

[6] Yu Suchorski, J. Beben, E. W. James, J. W. Evans, and R. Imbihl; "Fluctuation-induced transitions in a bistable surface reaction: catalytic CO oxidation on a Pt field emitter tip; Phys. Rev. Letters; Vol. 82, No. 9, pp. 1907–1910 (1999)

[7] Brown & Lemay; *Chemistry the Central Science*; p.508; Prentice Hall; 1998

[8] E.V. Albano, Hetero. Chem. Rev. **3**, 389 (1996); V.P. Zhdanov and B. Kasemo, Surf. Sci. Rep. **20**, 111 (1994); J.W. Evans, Langmuir **7**, 2514 (1991).

[9] J.W. Evans and T.R. Ray, Phys. Rev. E **50**, 4301 (1994).

[10] M. Tammaro, M. Sabella, and J.W. Evans, J. Chem. Phys. **103**, 10277 (1995).

[11] M. Tammaro and J.W. Evans, J. Chem. Phys. **108**, 762 (1998).

[12] R.M. Ziff, E. Gulari, and Y. Barshad, Phys. Rev. Lett. **50**, 2553 (1986).

[13] V.P. Zhdanov and B. Kasemo, Surf. Sci. **412/413**, 527 (1998).

CHAPTER 2. CO-OXIDATION MODEL WITH SUPERLATTICE ORDERING OF ADSORBED OXYGEN

I. STEADY-STATE BIFURCATIONS

A paper accepted by the Journal of Chemical Physics

E.W. James,[1,2] C. Song,[1] and J.W. Evans[1,2]

Ames Laboratory[1] and Department of Mathematics[2],

Iowa State University, Ames, Iowa 50011

ABSTRACT

We analyze a simple model for CO-oxidation on surfaces which incorporates both rapid diffusion of adsorbed CO, and superlattice ordering of adsorbed immobile oxygen. The adsorption sites are assumed to form a square lattice, and the superlattice ordering derives from an "eight-site adsorption rule", wherein diatomic oxygen adsorbs dissociatively on diagonally adjacent empty sites, provided that none of the six additional neighboring sites are occupied by oxygen. A "hybrid" formalism is applied to implement the model. Adsorbed CO is assumed randomly distributed on sites not occupied by oxygen (which is justified if one neglects CO-CO and CO-O adspecies interactions), and is thus treated within a mean-field framework. In contrast, the distribution of adsorbed oxygen is described within a lattice-gas framework. A comprehensive description of steady-state bifurcation behavior is provided using both conventional and "constant-coverage ensemble" Monte Carlo simulations. This behavior is compared with predictions of a suitable analytic pair-approximation. We show

that the oxygen superlattice ordering produces symmetry-breaking and coarsening phenomena not present in conventional Ziff-Gulari-Barshad-type reaction models.

PACS numbers: 82.65.Jv, 64.60.Cn, 82.20.Mj,

1. INTRODUCTION

In recent years, a rich variety of non-linear dynamics, steady-state bifurcation behavior, and spatial pattern formation, has been observed in catalytic surface reactions under ultra-high vacuum conditions on single crystal substrates. Furthermore, suitably tailored mean-field rate equation and reaction-diffusion equation treatments have been extremely successful in elucidating this behavior [1]. However, it is recognized that these treatments cannot precisely describe the influence of adlayer ordering on the reaction kinetics [2]. Furthermore, it was also recently noted that the conventional description of chemical diffusion used in reaction-diffusion equation treatments is overly simplistic. Diffusion of individual reactants in mixed adlayers is not independent, and "interference effects" may significantly affect chemical wave propagation [3]. Lattice-gas (LG) models can naturally address these complications. As a result, they have been invoked in an attempt to describe behavior in these reactive systems [4] with the same level of sophistication applied to treat the equilibrium properties of unreactive adlayers [5].

However, there have been two primary and common shortcomings of most previous LG-model studies. First, there has been a general lack of appreciation of the important role of rapid surface diffusion of reactant species (at least some of which have hop rates many orders of magnitude greater than other relevant rates). This rapid mobility produces strong

metastability and hysteresis in the reaction kinetics, and also controls length scale of spatial pattern formation [6-8]. Many studies have completely neglected surface mobility, whereas in fact it is effectively the "hydrodynamic regime" of rapid surface mobility for these reaction models which is of physical relevance. It should be noted that some "hybrid" models and simulation procedures have been developed to directly assess this regime [7,8]. Second, there has been little attempt to incorporate into LG-models realistic adspecies interactions, which produce significant adlayer ordering, and thus must strongly influence the reaction kinetics.

As a result of these two failings, here we are motivated to introduce a new "canonical" model for CO-oxidation. This model introduces commonly observed superlattice ordering of adsorbed oxygen, and also incorporates very rapid CO-diffusion. Here, we have adopted the surface chemistry terminology "superlattice ordering", which means that adspecies are locally ordered in a periodic array with unit cell larger than that of the array of adsorption sites. (This feature typically reflects strong repulsive short-range adspecies interactions.) Although our model is still rather simplistic, it does incorporate some basic features of real systems neglected in previous models, the consequences of which we discuss in detail in this paper. We forgo comparison with experiment here, as such comparison could be facilitated by further refinement of the model. However, we do note that our model has already been successfully applied to elucidate fluctuation behavior observed in CO-oxidation on a nanoscale Pt field emitter tip [9].

Our new "canonical" CO-oxidation model is described in detail in Sec.2, together with its exact master equations, and some exact relationships which apply for the reaction rate and for the steady-state coverages. Simulation procedures and analytic approximations to

the master equations are discussed in Sec.3. The basic properties of the model including its steady-state bifurcation and critical behavior are analyzed in detail in Sec.4. In Sec.5, we focus on a specific consequence of the introduction of superlattice ordering of adsorbed oxygen. We show that the model exhibits a symmetry-breaking order-disorder transition in the reactive steady-states of the model (akin to behavior in equilibrium models). We also observe a novel domain coarsening phenomenon associated with symmetry-breaking, and analyze its kinetics. In Sec.6, we summarize our findings, and discuss some related issues and model extensions.

2. REACTION MODEL

2.1 LANGMUIR-HINSHELWOOD (LH) MECHANISM AND ADLAYER STRUCTURE

In this study, we consider exclusively surfaces characterized by a square lattice of adsorption sites. We adopt a conventional LH mechanism for CO-oxidation as indicated below, where "gas" denotes a gas phase species, and "ads" an adsorbed phase species (see also Fig.1):

(i) CO(gas) adsorbs at single empty sites at rate P_{CO}, and CO(ads) desorbs at rate d;

(ii) O_2(gas) is adsorbs dissociatively at diagonal nearest-neighbor (NN) empty sites at rate ½ P_{O2}, provided that all six additional NN sites to these are unoccupied by O(ads). Furthermore, O(ads) does not desorb and is assumed immobile. The latter feature, together with the adsorption rule, ensures that no adjacent pairs of O(ads) are created during the process.

(iii) CO(ads) is assumed highly mobile (e.g., via rapid hops to NN and diagonal NN empty sites), and is assumed randomly distributed on sites not occupied by O(ads); and

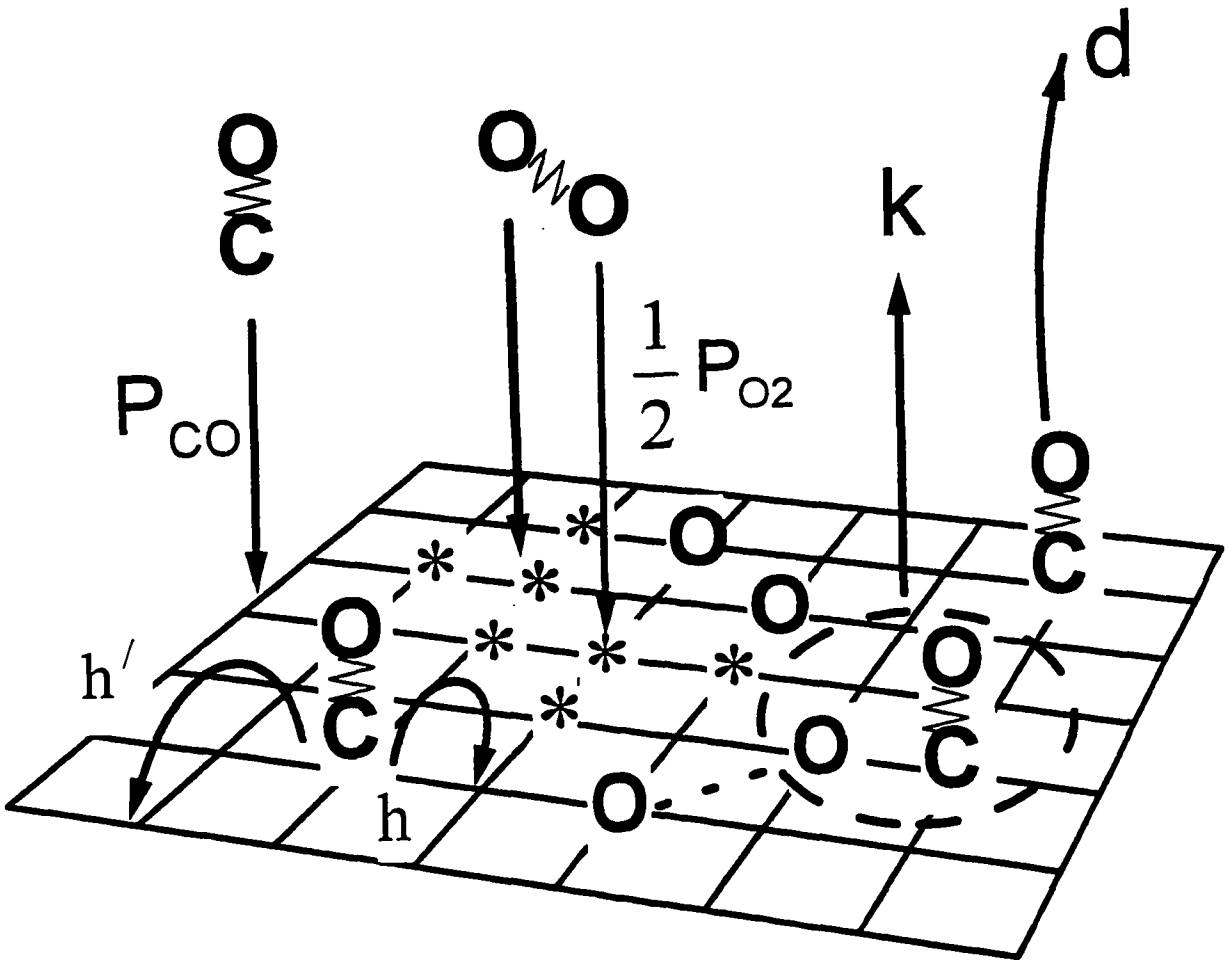

Figure 1. Schematic of the reaction model illustrating the various mechanistic steps, together with their rates. For the O_2(gas) adsorption event, the eight sites required to be unpopulated by O(ads) are indicated by *. The dotted line between two O(ads) indicates that they were associated with the same molecule. CO(ads) is shown to hop to NN empty sites at rate h, and to next NN empty sites at rate h′, where in our model both $h \to \infty$ and $h' \to \infty$ (but h′/h can have any limiting value).

(iv) Adjacent CO(ads) and O(ads) react at rate k.

Our prescription of oxygen adsorption is termed the "eight-site rule" since an ensemble of eight sites not occupied by O(ads) are required for adsorption. This rule was originally applied to describe dissociative adsorption of oxygen on Ni(100) and Pd(100) [10]. The "eight-site rule" reflects strong NN O(ads)-O(ads) repulsive interactions, resulting in superlattice ordering often observed in real systems. As indicated in Sec.1, this feature has not been incorporated into most previous LG modeling of CO-oxidation, where oxygen adsorption was assumed to occur on adjacent (NN) empty sites [4,6-8,11]. Among previous studies, two exceptions which did incorporate the "eight-site rule" are Ref.[9] which reported briefly some properties of coverage fluctuations in the above model near a cusp bifurcation or critical point, and Ref.[12] which considered some aspects of model behavior when $k=\infty$. We emphasize that implicitly our model still neglects CO(ads)-CO(ads) and CO(ads)-O(ads) interactions, since we assume that CO(ads) is randomly distributed on non-O(ads) sites. Certainly such interactions are present to some extent, and will affect behavior in real systems.

Next we discuss further the model parameters, and our assignment of their values. Note that P_{CO} corresponds to the impingement rate per site for CO(gas). Also, since there are two diagonal NN pairs of sites for each single site on the square lattice, P_{O2} corresponds to the impingement rate per site for O_2(gas). Below we choose $P_{CO}+P_{O2}=1$ (which sets the time scale), and set k=1 when presenting specific results. Behavior for other k is discussed briefly in Appendix A. We denote the coverage of CO(ads) by θ_{CO}, of O(ads) by θ_O, and the total coverage by $\theta=\theta_{CO}+\theta_O$ (where these quantities are measured in units of monolayers).

Finally, we briefly comment on and illustrate some basic features of the ordering in the oxygen adlayer. Since the kinetic rules of the reaction model preclude the formation of NN O(ads)-pairs, the oxygen adlayer tends to display "checkerboard" or centered-two-by-two [c(2×2)] ordering, especially for higher coverages of O(ads). This is analogous to behavior in an equilibrium "hard-square model" where adspecies have infinitely repulsive NN interactions [13]. As shown in Fig.2, c(2×2) domains have degeneracy two, atoms in domains of different phase residing on one of two interpenetrating "sublattices". (The latter terminology is adopted from equilibrium statistical mechanics, although it is potentially confusing here as atoms in a populated sublattice exhibit superlattice ordering!) In addition, individual domains can have "internal defects", that is sites not occupied by O(ads) which are surrounded by four diagonal adjacent O(ads). The density of these will be denoted by D.

A schematic "hard-square representation", highlighting these features, replaces the circular atoms by diamonds with side length $\sqrt{2}$ times the lattice constant. This representation is particularly useful in characterizing so called "jammed states", where there are no ensembles of sites available for further oxygen adsorption. In such states, the only uncovered regions of the surface correspond to either isolated internal defects, or to domain or anti-phase boundaries which separate adjacent domains of different phase. The latter are diagonal strips of width $1/\sqrt{2}$, occasionally decorated by isolated "external" defects. See Fig.2.

2.2 EXACT MASTER EQUATIONS AND RESULTS

Despite the feature that our model incorporates non-trivial spatial correlations in the distribution of O(ads), it is possible to write down a formally exact hierarchy of master equations describing the reaction kinetics. For notational simplicity, we denote CO(ads)

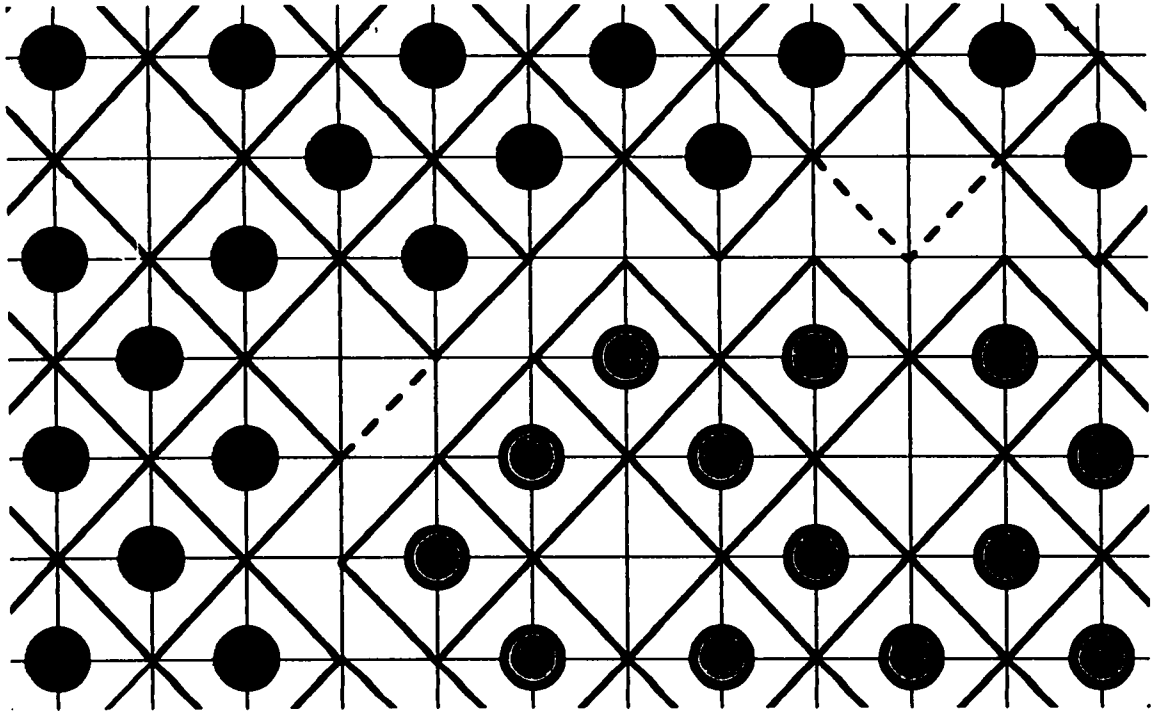

Figure 2. Schematic of the configuration of oxygen atoms in a jammed state. Atoms in two adjacent c(2×2) domains of different phase are indicated by black and gray circles. Also shown is the "hard square representation" where atoms are replaced by diamonds. This representation highlights both the three internal defects, as well as the domain boundary, which is decorated by two external defects (indicated by dashed lines). The hard square representation will be used in some subsequent figures, shading diamonds in one phase by black, and those in the other by gray.

by A, O(ads) by B, and we let E correspond to empty sites, and Z correspond to sites not occupied by B. So one could write E = not(A or B), and Z = not(B). In addition, [K] will denote the fraction of sites in state K, so $[A]=\theta_{CO}$ denotes the coverage of CO(ads), etc.. Then, from conservation of probability, one has

$$[E]=1-[A]-[B], \text{ and } [Z]=1-[B]. \tag{1}$$

Also, [K J] denotes the probability that the left site in a specific NN pair is in state K and the right one is in state J, etc.. Then from conservation of probability, one has that, e.g.,

$$[Z\ Z]+[B\ Z]+[Z\ B]+[B\ B]=1, \text{ where } [B\ B]=0 \ \&\ [B\ Z]=[Z\ B]=[B], \text{ so } [Z\ Z]=1-2[B]. \tag{2}$$

Finally, in terms of this notation, the density of "internal defects" is given by

$$D=\begin{bmatrix} B & & B \\ & Z & \\ B & & B \end{bmatrix}=\begin{bmatrix} B & Z & B \\ Z & Z & Z \\ B & Z & B \end{bmatrix} \tag{3}$$

Using this notation, the exact master equations have the form (cf. Ref.[7])

$$d/dt\ [A] = P_{CO}[E] - d[A] - 4k[A\ B], \text{ and} \tag{4a}$$

$$d/dt \cdot [B] = 2P_{O_2}\left[\begin{array}{ccc} & Z & \\ Z & E & Z \\ & Z & \end{array}\right] - 4k[A \quad B], \tag{4b}$$

where the factor of 4 corresponds to the coordination number of the square lattice. Further simplification of the above multi-site configuration probabilities is possible exploiting the feature of our model that the A's are randomly distributed on non-B or Z sites. In particular, one has (cf. Ref.[7])

$$[A \quad B] = ([A]/[Z])\,[Z \quad B] = [A][B]/(1-[B]), \tag{5}$$

providing an <u>exact</u> expression for the reaction rate terms appearing in (4). The possibility of obtaining a simple exact expression for the reaction rate in this model is perhaps not surprising. It derives from the feature that every B is assured to be surrounded by four non-B or Z-sites, and all Z-sites are occupied by A with the same probability. For the configuration probability appearing in the adsorption term in (4b), again since the A's are randomly distributed on Z-sites, one has

$$\begin{bmatrix} & Z & \\ Z & E & Z \\ & Z & \end{bmatrix} = ([E]/[Z])^2 \begin{bmatrix} & Z & \\ Z & Z & Z \\ & Z & \end{bmatrix}. \qquad (6)$$

There is no simple exact expression for the configuration of eight Z's appearing on the RHS of (6). Thus, (4) should be regarded as the lowest order equations in a hierarchy of equations for the probabilities of various multi-site configurations. However, in Sec.3, we shall discuss possible approximations for (6), which allows closure of the basic rate equations (4).

Finally, we note one important consequence of the exact expression (5) for the reaction rate. If one considers the steady-state, where d/dt [K]=0 for K=A or B, then from (4a) and (5), one obtains

$$[A] = \frac{P_{CO}(1-[B])}{P_{CO} + d + 4k[B]/(1-[B])} \qquad (7)$$

Thus, there is simple exact relationship between the steady-state values of $[A]=\theta_{CO}$ and $[B]=\theta_O$.

2.3 SPECIAL CASE $P_{CO}=0$ (EIGHT-SITE MODEL FOR DIMER ADSORPTION)

When $P_{CO}=0$ (so $P_{O2}=1$), there is no CO-adsorption. Thus, oxygen adsorbs randomly and irreversibly, subject to the eight-site rule described in Sec.2.1(ii), to form a immobile adlayer with c(2×2) short-range order. Adsorption will continue until there are no further available ensembles of eight empty sites suitable for adsorption, after which the system remains in a non-equilibrium "jammed state". These types of non-trivial adsorption processes have been studied extensively within the framework of "Random Sequential Adsorption" (RSA) [14]. Of particular interest in these models is the dependence on coverage, θ, of the "sticking probability", $S(\theta)$, that an impinging molecule will actually adsorb and remain on the surface. In general, it is possible to develop formally exact expansions for the short-time or low-coverage adsorption kinetics, and thus for $S(\theta)$. It is also possible to determine the precise way in which $S(\theta)$ vanishes on approaching jamming.

The RSA problem corresponding to our model with $P_{CO}=0$ has been studied extensively [15]. The coverage of the jammed state, $\theta_J=0.3616$, is well below the maximum value of 0.5 for perfect c(2×2) ordering. As noted in Sec.2.1, this jammed state is a collection of c(2×2) domains separated only by domain boundaries, and containing internal defects (which have a density of D=0.0098). It also follows that $S(\theta)$ equals the probability appearing in (6) (noting that [E]=[Z], when $P_{CO}=0$ and [A]=0). Specifically, one finds that

$$S(\theta) = 1 - 6\,\theta + (135/16)\,\theta^2 + O(\theta^3), \text{ and } S(\theta) \sim (\theta_J - \theta)/4, \text{ as } \theta \rightarrow \theta_J, \qquad (8)$$

from which a uniformly accurate Pade approximation can be constructed [15]. A detailed characterization of the disordered geometry of the jammed state is also available [15].

3. METHODS OF ANALYSIS

3.1 HYBRID SIMULATION PROCEDURES

Conventional kinetic Monte Carlo simulation of the above model with specified rates (for adsorption, desorption, and reaction) is possible with only minor modification to account for the randomly distributed, mean-field nature of the CO(ads) or A. Specifically, for the O(ads) or B, one performs a conventional simulation tracking the position of every particle on the lattice. However, for the CO(ads) or A, one simply tracks the total number of adsorbed particles. From this and the number of Z-sites (not occupied by B), one can calculate the instantaneous probability that any Z-site is occupied by A. This probability is then used in determining whether specific adsorption, desorption, and reaction events take place. See Ref.[7] for further discussion.

One feature of hybrid models, contrasting LG models with finite adspecies mobility [16], is that they display "true bistability", i.e., there is a range of model parameters where there a two stable steady-states coexist, akin to the behavior of mean-field models [7,8]. This feature (which is clearly illustrated in the figures in Sec.4) is due to the effective infinite mobility or randomization of the A's. The standard scenario in systems displaying bistability is that the attractive basins associated with two such stable states are separated by an unstable state. This unstable state is as easily determined as the stable states in a mean-field treatment. However, in our hybrid reaction model, it incorporates non-trivial spatial correlations, and

cannot be accessed by conventional simulation techniques. Fortunately, one can apply an unconventional "constant-coverage ensemble" simulation approach [17] to resolve this problem [7]. Here, one specifies some "target" coverage, [A]*, of CO(ads) or A, say, and performs a conventional simulation, except for the adsorption step. In that step, instead of adsorbing with fixed relative probabilities, one attempts to absorbs CO or A if [A]<[A]*, and attempts to adsorb O_2 or B_2 if [A]>[A]*. Then, one tracks the asymptotic fraction of attempts to deposit CO or A, and identifies this fraction as the P_{CO} corresponding to [A]*. These simulations recover the stable states obtained by conventional simulations, but also map out the connecting unstable states, thus allowing complete determination of the "phase diagram".

3.2 PAIR-APPROXIMATION

To close the rate equations (4) at the lowest level, one needs a reasonable approximation for the configuration probability appearing on the RHS of (6) in terms of the adspecies coverages. One can invoke the standard pair- or Kirkwood-type approximation which has the form (cf. Ref.[7])

$$\begin{bmatrix} & Z & \\ Z & Z & Z \\ & Z & \end{bmatrix} \approx [Z \quad Z]^8 / [Z]^8 = (1-2[B])^8 / (1-[B])^8. \tag{9}$$

Using (5), (6), and (9) in (4) produces closed equations for [A] and [B]. Considering the corresponding steady-state form of (4b), and using (7), yields an 11^{th}-order polynomial equation

$$2P_{O2}(1-2[B])^8\{4k[B]+d(1-[B])\}^2-4kP_{CO}[B](1-[B])^9\{(P_{CO}+d)(1-[B])+4k[B]\}=0, \quad (10)$$

to be solved for the steady-state values of [B]. Corresponding steady-state [A]-values then follow immediately from (7). We emphasize that this analysis yields estimates of both stable and unstable steady-state behavior. As a specific example, the limiting behavior where $P_{CO}\rightarrow 0$ can be analyzed directly (although not accurately) in this approximation. From (10), one obtains

$$(1-2[B])^8 \sim cP_{CO}, \text{ so } [B] \sim \tfrac{1}{2} - \tfrac{1}{2}c^{1/8}(P_{CO})^{1/8}, \text{ as } P_{CO}\rightarrow 0, \text{ where } c=2^{-10}\,4k/(4k+d). \quad (11)$$

There is no reason to expect that the approximation (9) will be particularly accurate for higher coverages of O(ads) or B. The simplest illustration of this inaccuracy is that for the RSA problem corresponding to $P_{CO}=0$, this pair-approximation predicts a coverage for the jammed state of ½, rather than the non-trivial value of 0.3616. Furthermore, we shall see in Sec.5 that the prediction (11) is also qualitatively incorrect. This failure derives in part from the feature that the pair-approximation does not account for an observed dramatic symmetry-breaking feature of the reaction model for higher [B]. This symmetry-breaking entails the development unequal populations of B on the two sublattices associated with c(2×2) ordering (see Sec.5). Consider the extreme case where only <u>one</u> sublattice is populated, except for

randomly distributed "defects". Then, the probability of the configuration on the LHS of (6) equals the average of $(1-[A]-2[B])^2$ and $(1-[A])^2(1-2[B])^6$, corresponding to choosing the central empty sites on the B-populated and B-unpopulated sublattices, respectively. These expressions yield a quite distinct dimer adsorption rate than the pair-approximation (9). The first term dominates as $P_{CO} \rightarrow 0$ yielding the steady-state behavior which is distinct from equation (11), but which is still inaccurate [18].

4. STEADY-STATE PHASE DIAGRAM

4.1 PAIR-APPROXIMATION PREDICTIONS VERSUS EXACT BEHAVIOR

We shall see that the analytic pair-approximation predicts and "exact" simulation confirms the existence of bistability in the steady-states of the reaction model for $d<d_c$, where $d=d_c$ corresponds to a cusp bifurcation or "critical" point. Specifically, for $d<d_c$, a reactive stable state with low θ_{CO} (=[A]) and high θ_O (=[B]) coexists with a relatively inactive stable state with high θ_{CO} and low θ_O, for a range of P_{CO}. These two states are "connected" by an unstable state. This range of bistability is denoted by $P_{s-}<P_{CO}<P_{s+}$, where $P_{s\pm}$ are upper and lower saddle-node bifurcations or "spinodals" (except that when $d=0$, $P_{s-}=0$ corresponds to a transcritical bifurcation). The width, $P_{s+}-P_{s-}$, of the bistable region vanishes as $d \rightarrow d_c$ from below. We recall that the conventional monomer-dimer reaction model, with dimer adsorption on adjacent empty sites, displays a continuous O(ads)- or B-poisoning transition for lower P_{CO}, both for the cases of no adspecies mobility [4,11], and for infinite mobility [7] of CO(ads) or A. In contrast, obviously the model considered here necessarily has

θ_O=[B]≤1/2, and thus cannot have an O(ads)- or B-poisoning transition, a feature consistent with experimental observations [1]. Finally, we remind the reader that model behavior for extreme values of the reaction rate, k<<1 and k>>1, is briefly discussed in Appendix A.

First, we present results for the steady-state phase diagram obtained from an approximate analytic treatment using the pair-approximation (9). Solving (10) produces the steady-state variation of θ_O versus P_{CO} shown in Fig.3a, for various d. The corresponding behavior of θ_{CO} obtained from (7) is shown in Fig.3b. The cusp bifurcation at $d_c \approx 0.048$ is apparent in both these figures. Note that for all values of d, one has $\frac{1}{2} - \theta_O \sim (P_{CO})^{1/8}$, as $P_{CO} \to 0$, as shown by (11). For d=0, the bistable region extends from $P_{s-}=0$ to $P_{s+} \approx 0.3481$. As $d \to d_c$, both P_{s-} and P_{s+} approach $P_c \approx 0.4004$.

Second, we present "exact" results for the steady-state phase diagram obtained using the constant-coverage simulations to access the unstable as well as the stable states. Fig.4a shows the behavior of θ_O versus P_{CO}, and Fig.4b shows the behavior of θ_{CO} versus P_{CO}, for various d. The behavior of these two quantities is related exactly by (7). One now finds a cusp bifurcation at $d_c \approx 0.053$, a value slightly above the prediction from the pair-approximation. For d=0, the bistable region extends from $P_{s-}=0$ to $P_{s+} \approx 0.360$. As $d \to d_c$, both P_{s-} and P_{s+} approach $P_c \approx 0.414$. A more complete comparison of exact properties at the cusp bifurcation, and predictions from the pair-approximation, is given in Table I.

Certainly, the general behavior predicted by the pair-approximation agrees qualitatively with "exact" results. This is also evident in a different comparative representation of the steady-state phase diagrams in the (P_{CO}, d)-plane shown in Fig.5. The one major difference is evident, specifically the non-trivial "exact" limiting behavior of

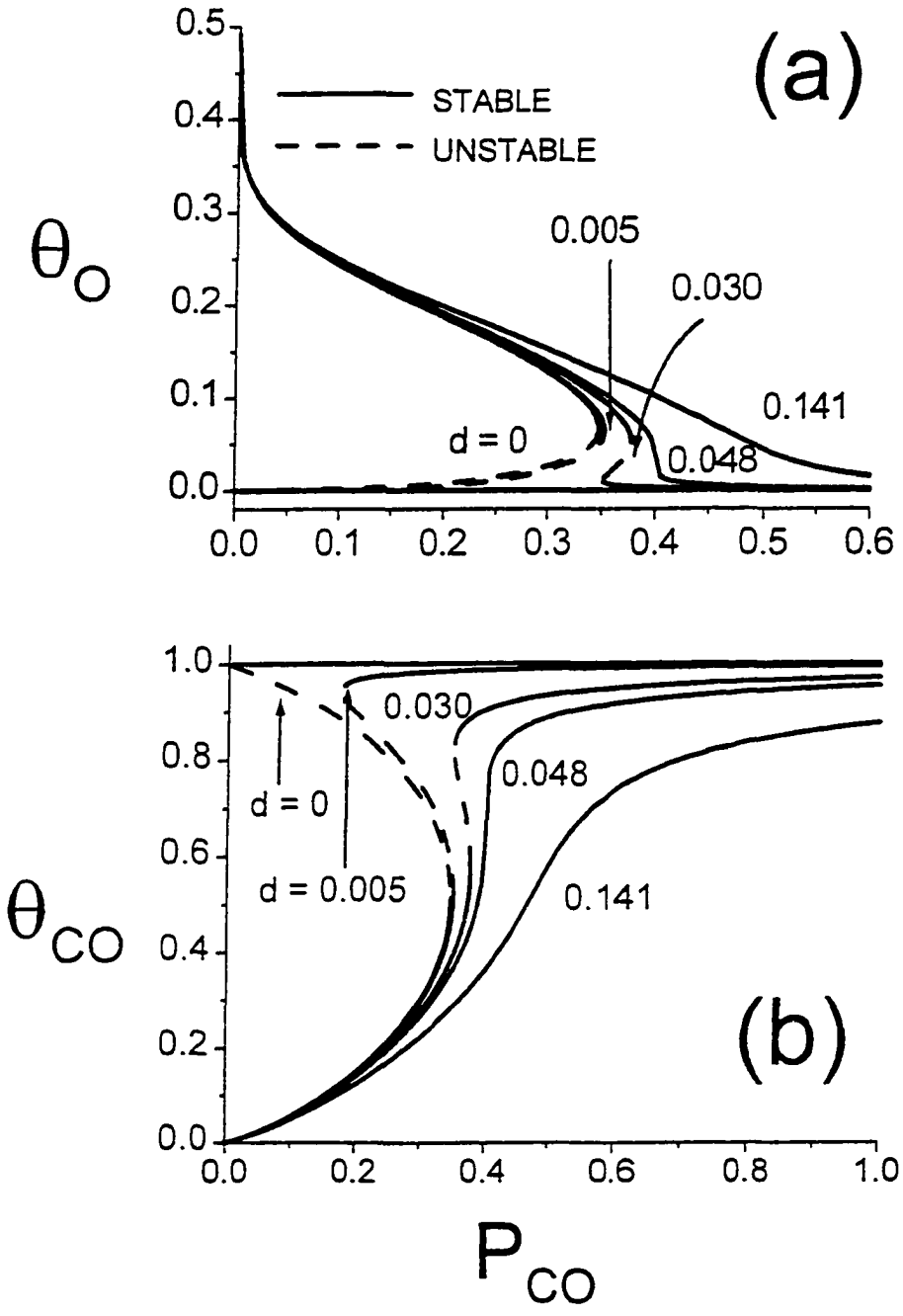

Figure 3. Steady-state "phase diagram" predicted by the pair-approximation showing the variation with P_{CO} of: (a) θ_O; and (b) θ_{CO}, for various fixed d (shown), and k=1. Stable (unstable) steady states are indicated by solid (dashed) lines.

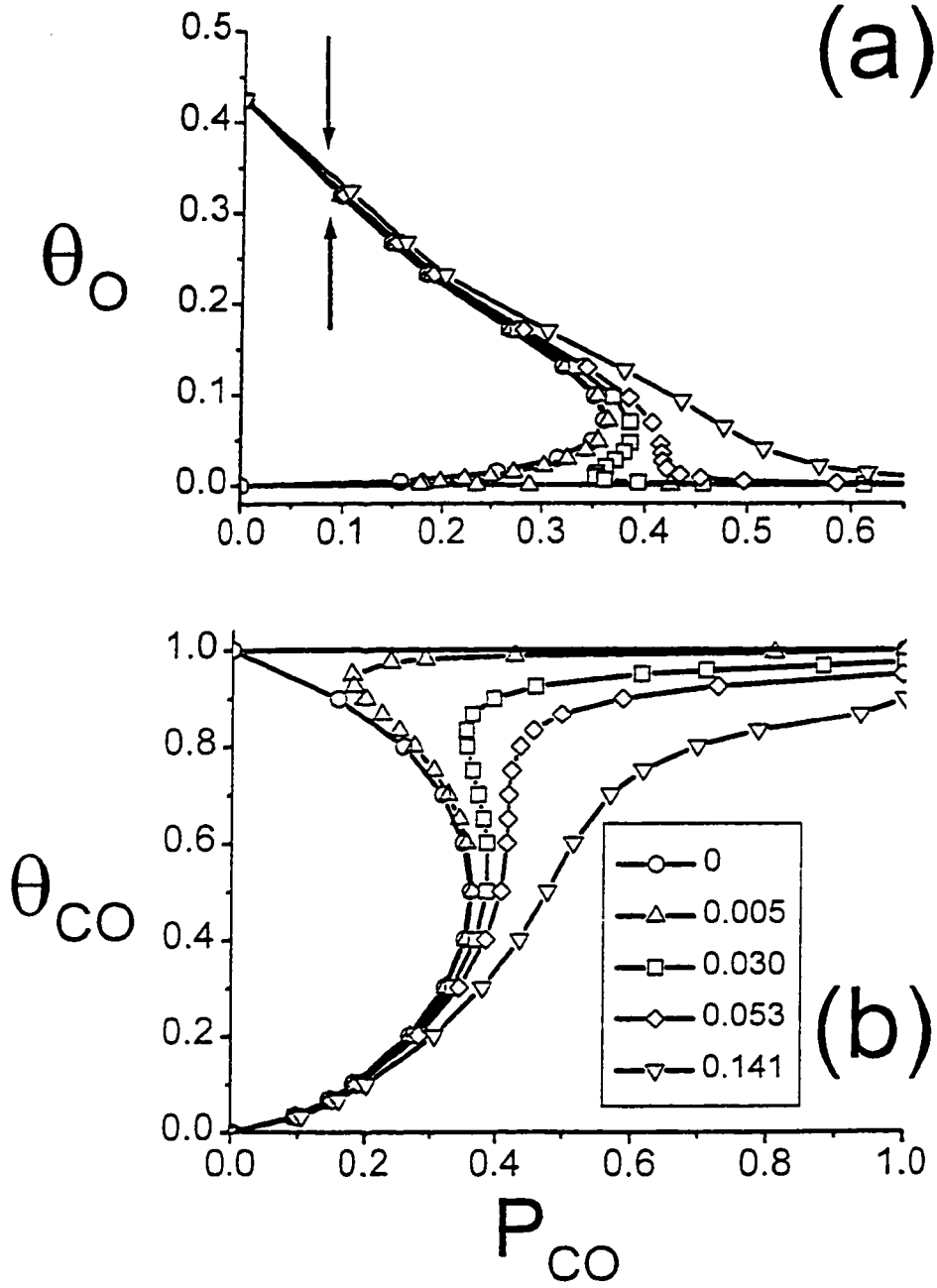

Figure 4. Steady-state "phase diagram" predicted by constant-coverage ensemble simulations showing the variation with P_{CO} of: (a) θ_O; and (b) θ_{CO}, for various fixed d (shown), and k=1. The arrows in (a) indicate the location of the symmetry-breaking transition.

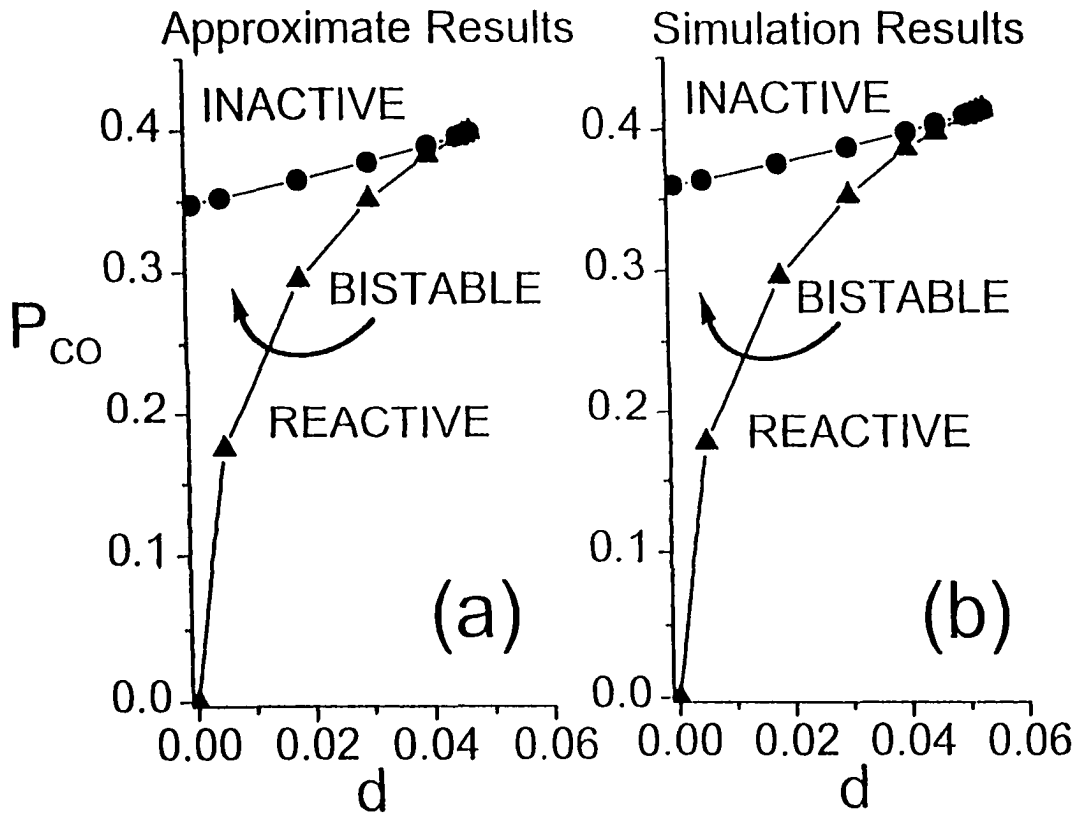

Figure 5. Steady-state "phase diagrams" in the (P_{CO},d)-plane showing the regions with a single reactive and (relatively) inactive state, as well as the bistable region obtained from: (a) the pair-approximation; (b) simulations

Table I. Comparison of "exact" properties at cusp bifurcation, and predictions from the pair-approximation.

	d_c	P_c	θ_O	θ_{CO}
Pair-Approx.	0.048	0.400	0.030	0.676
"Exact" sim.	0.053	0.414	0.033	0.663

$\theta_O \rightarrow 0.42534$, as $P_{CO} \rightarrow 0$, in contrast to the prediction of ½ in the pair-approximation. There is actually another more subtle difference between approximate and exact behavior, not evident by comparing Fig.3a and Fig.4a. In conventional simulations of model behavior, one finds a symmetry-breaking transition in the reactive steady-state (i.e., the populations of O(ads) or B on the two c(2×2) sublattices become unequal), as one decreases P_{CO} to the point where θ_O=[B] exceeds a value of about 0.31. This transition and the limiting behavior as $P_{CO} \rightarrow 0$ are discussed in some detail in the Sec.5.

Finally, we comment on one other generic issue for systems such as our reaction model which exhibit bistability. One is naturally motivated to consider the relative stability of coexisting stable states, and in particular to determine the point of equistability which should occur somewhere in the "middle" of the range of bistability. A strategy to address this non-trivial issue is presented in Appendix B.

4.2 COMPARISON WITH A SIMPLE MODEL FOR B_2-ADSORPTION & B-DESORPTION

Focusing on the dynamics of the oxygen or B's in our reaction model, there are two competing processes: dissociative dimer adsorption on suitable eight-site ensembles, and reaction-mediated random removal of adsorbed monomers. It is thus natural to compare behavior of the reaction model with that of a simple single-species model, where dissociative adsorption of dimers, B_2, occurs randomly according to the eight-site rule with attempt rate P, and adsorbed monomers, B, are removed randomly by non-reactive desorption at rate r. The steady-state of this simple model is determined solely by the ratio r/P, the steady-state value of [B] decreasing monotonically to zero with increasing r/P>0. The case r/P=0 corresponds to $P_{CO}=0$ in the reaction model (RSA of dimers). Also, behavior of the simple model as $r/P\rightarrow 0$ corresponds to that of the reactive model as $P_{CO}\rightarrow 0$ (see Sec.5.2 and 5.3). However, differences are apparent for $P_{CO}>0$. For a given [B], the reaction model has various steady-states (depending on the value of d), and some range of smaller [B] is not even accessed for $d<d_c$. Thus, the steady-states of the reaction model must differ from those of the simple model with the same [B]. This discrepancy arises since, in the reaction model, the rate of adsorption onto a specific eight-site ensemble, all sites of which are specified to be in the Z-state, equals $P_{O2}(1-[A]-[B])^2/(1-[B])^2$. The desorption rate per B equals 4k[A]. Thus, the ratio of these rates depends non-trivially on [B], in contrast to the simpler model, and can be determined explicitly using (7).

5. BEHAVIOR FOR LOW P_{CO}: SYMMETRY-BREAKING AND COARSENING

5.1 SYMMETRY-BREAKING TRANSITION

As indicated in Sec.4.1, for d=0, there is a spontaneous symmetry-breaking in the reactive steady-state of the model for P_{CO} below about 0.135, or for θ_O=[B] above about 0.314. This feature "replaces" an unphysical oxygen poisoning transition familiar in conventional reaction models with dimer adsorption on adjacent sites [4,11]. No doubt, symmetry-breaking also occurs for cases with d>0, when θ_O=[B] increases above similar values of about 0.31-0.32. To quantify symmetry-breaking, we labeled the two c(2×2)-sublattices by + and -, and let $[B_+]$ and [B.] denote the fraction of sites on the + and - sublattice occupied by B, respectively, so θ_O=[B] = ($[B_+]$+[B.])/2. Then, we introduce the order parameter,

$$S = | [B_+]-[B.] | / ([B_+]+[B.]), \qquad (12)$$

which naturally measures the imbalance in the c(2×2)-sublattice populations of B or O(ads). For an extremely large system, S is negligible above the transition where there is no symmetry-breaking, and it increases quickly below the transition achieving a value of near unity for small P_{CO}. For smaller systems, this discontinuous behavior is smoothed out. Fig.6 shows our simulation results for a 100×100 site system, where S increases quickly from a small but non-vanishing value (of the order of the inverse square root of the system size) to around unity, as P_{CO} decreases below about 0.135.

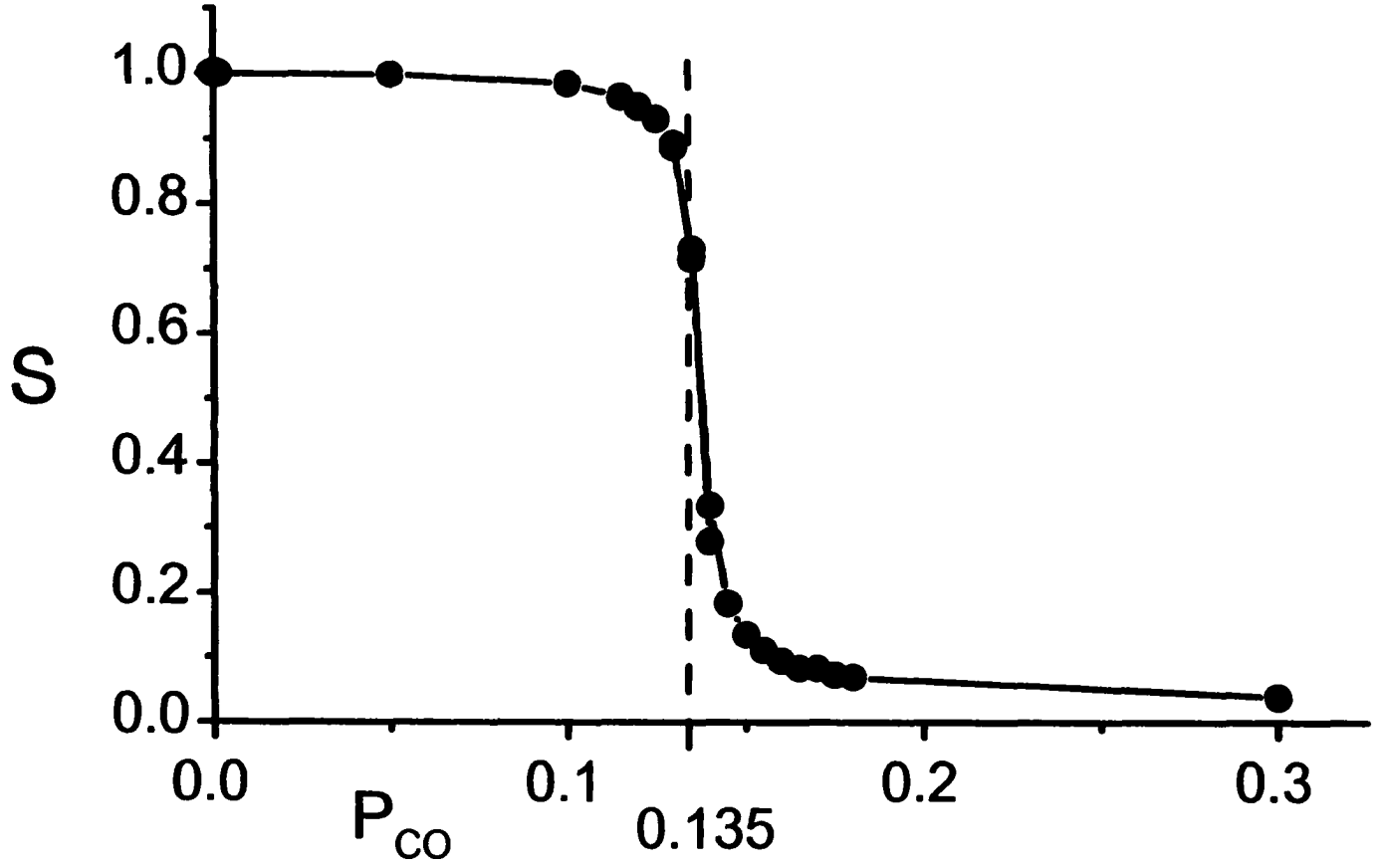

Figure 6. Variation of the order-parameter, S, with P_{CO} in the reaction model with d=0. Results are shown for a 100×100 site lattice.

This behavior is entirely analogous to that at a symmetry-breaking order-disorder transition in an equilibrium system. A natural comparison is with the equilibrium "hard-square model" where (in the language of the reaction model) O(ads) or B's randomly occupy non-neighboring sites on a square grid, and the symmetry-breaking transition occurs when θ_O=[B] increases above about 0.368 [13]. The feature that the transition value of θ_O=[B] in the hard-square model is substantially higher than in the reaction model is easily understood: the maximum value of θ_O=[B] in the hard-square model is 0.5, versus a maximum reactive steady-state value of 0.42534, as $P_{CO} \to 0$ in the reaction model. In the latter case, the typically much higher density of "internal defects" within individual c(2×2) domains induces the symmetry-breaking transition at a correspondingly lower value of θ_O= [B]. In future work [19], we shall present a detailed analysis of the transition in the reaction model, ascertaining whether it is in the same universality class as the order-disorder transition in the equilibrium hard-square model.

5.2 EVOLUTION IN THE REGIME $P_{CO} \to 0+$

Next, we focus attention on the non-trivial limiting behavior of the reaction model as $P_{CO} \to 0+$. Consider the evolution of the model starting with an initially empty lattice or surface. Since P_{CO} is negligible (compared to $P_{O2} \approx 1$), initially oxygen is deposited (effectively in the absence of CO) according to the eight-site rule until the lattice is "jammed" with a coverage of O(ads) or B of about 0.3616. At this point, a second much slower stage of the process commences (controlled by the rate P_{CO}). The effect of the slow deposition of CO is the slow removal of individual B's (at rate proportional to P_{CO}) followed

by the effectively immediate filling by O_2- or B_2-dimers at any eight-site ensembles thus created. More specifically, removal of a single O(ads) or B by reaction in a "jammed" state with no eight-site ensembles may result in the creation of zero, one, or possibly more eight-site ensembles suitable for dimer adsorption. If none are created, the process continues by random removal of another O(ads) or B. If one is created, it is immediately filled by a dimer. If more than one is created, one is chosen at random and filled by a dimer (and we note that this leaves no further eight-site ensembles available for filling). Thus, the system evolves through a sequence of jammed states, with the characteristics described previously in Sec.2.1.

From the above discussion, it is clear that one can readily simulate directly the limiting behavior as $P_{CO} \to 0+$ (on a time scale $t' \propto P_{CO}t$). Next, we report the results of these simulations. We start such a simulation with an initially jammed state obtained from dimer filling according to the eight-site rule. Implementing the above dynamics, one finds that θ_O=[B] initially decreases from the "initial" value of 0.3616. This corresponds to an initial increase (and ensuing stabilization) in the density of internal defects within the individual c(2×2) domains. Subsequently, on a somewhat slower time-scale, θ_O=[B] starts to increase again as a result of the coarsening of individual c(2×2) domains, finally reaching a value of 0.42534. This produces a decrease in the fractional area of domain boundary,

$$F = 1 - 2[B] - 2D. \qquad (13)$$

Evolution of the B-adlayer during this coarsening process is illustrated in the sequence of snapshots in Fig.7. We have quantified the coarsening process by monitoring F versus time, t', for an 800×800 lattice. The results shown in Fig.8 indicate that

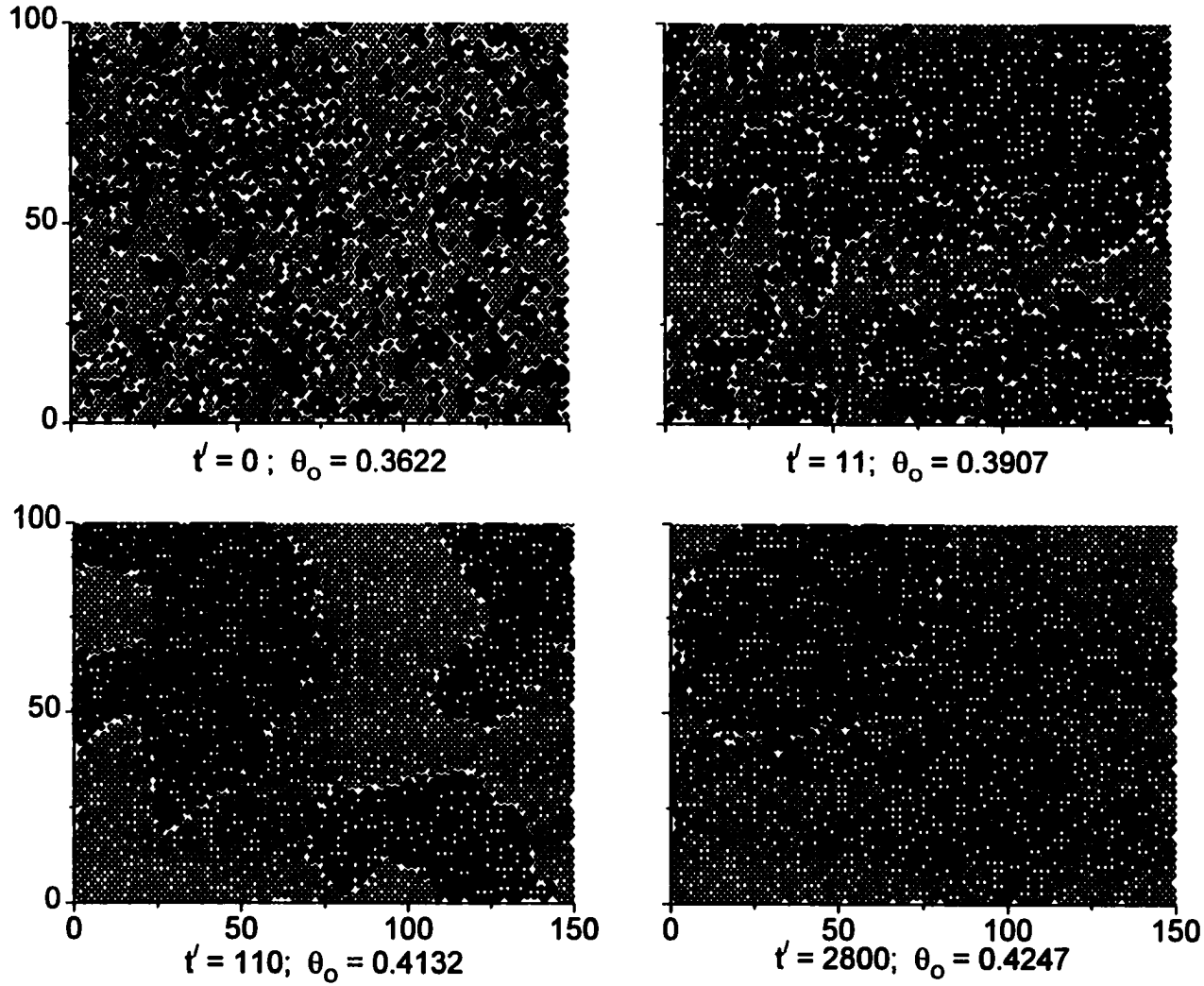

Figure 7. Snapshots (using the hard-square representation) of a time sequence of adlayer configurations for P_{CO}=0+, which reveals the coarsening process. Corresponding times (t′) and coverages (θ_O) are shown.

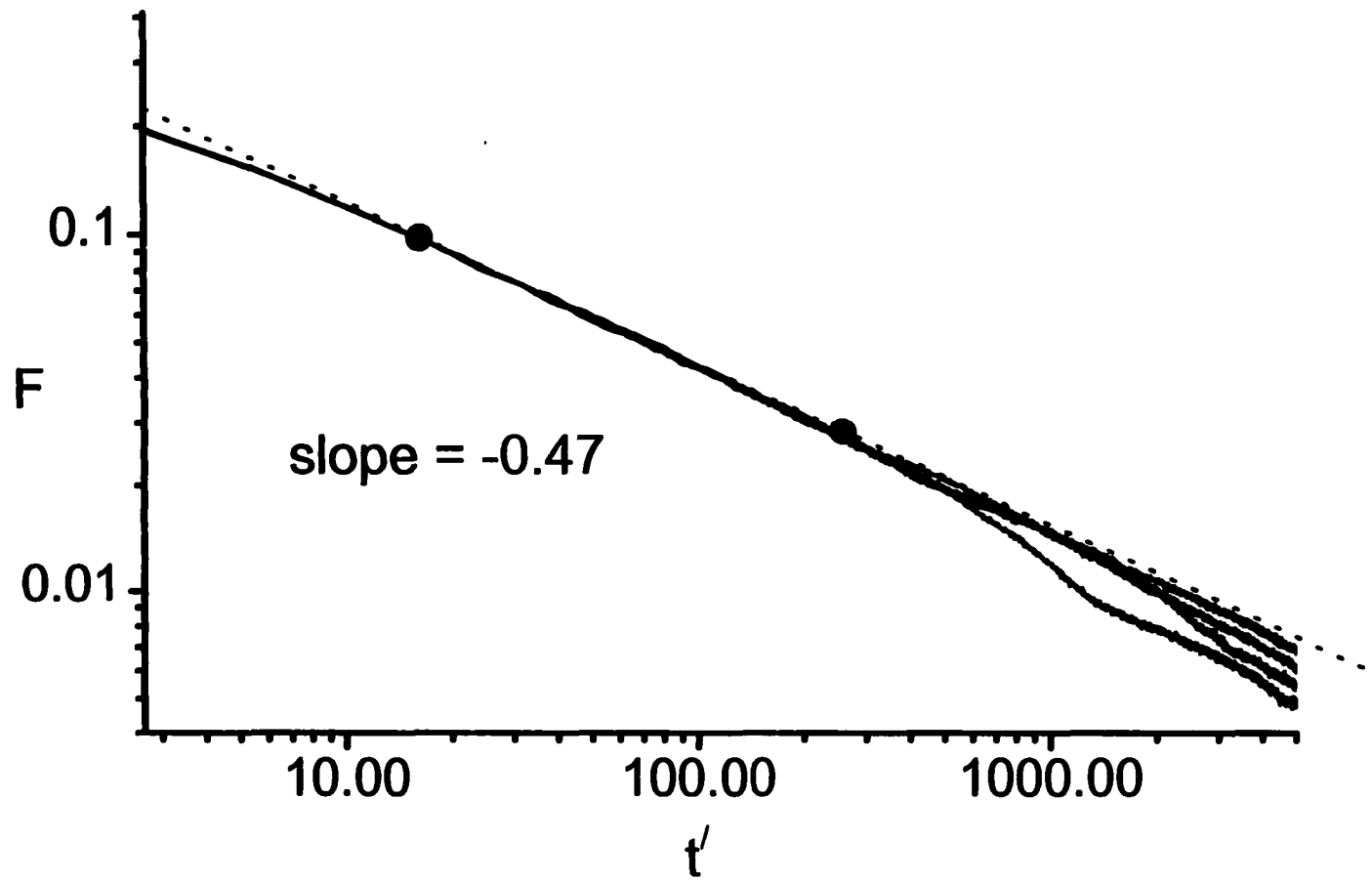

Figure 8. Log-log plot revealing the decrease with time, t′, of the fractional area of domain boundary, F, for four simulations on an 800×800 site lattice. The dots indicate the regime from which we extracted the temporal scaling exponent listed in (14).

$$F \sim (t')^{-0.47}, \text{ for } 15<t'<250, \qquad (14)$$

suggesting that for an infinite lattice $F \sim (t')^{-1/2}$, as $t' \to \infty$. The characteristic linear dimension (or chord length) of c(2×2) domains scales inversely with F, and thus increases like $(t')^{1/2}$.

The latter behavior is reminiscent of classic Lifshitz-Cahn-Allen interface-curvature-driven coarsening [20]. Indeed, it is not unreasonable that the mean propagation velocity for domain boundaries in our model should scale with curvature, noting that the velocity vanishes for zero curvature. To illustrate this feature, in Fig.9, we have shown the individual atomic steps in one pathway leading to the shrinkage by one lattice constant of a highly curved portion of domain boundary, and an associated increase in the number of adspecies. One can easily confirm that more steps are required for the similar shrinkage of a less curved portion of domain boundary. Finally, it is appropriate to note that there are broad variety of other non-equilibrium growth, evolution, or reaction models described by Kardar-Parisi-Zhang or Edwards-Wilkinson equations, where interface propagation also has a curvature dependence [6, 21, 22].

A second analysis of behavior when $P_{CO} \to 0+$ exploits the feature that eventually a single sublattice is populated. It is thus natural to instead start the simulation of random monomer removal followed by immediate dimer adsorption (if possible) with a perfect c(2×2) ordered state. In this case, we find that the coverage, θ_O=[B], decreases monotonically from 0.5 (as the defect density increases), eventually stabilizing at the value of 0.42534 consistent with that found above.

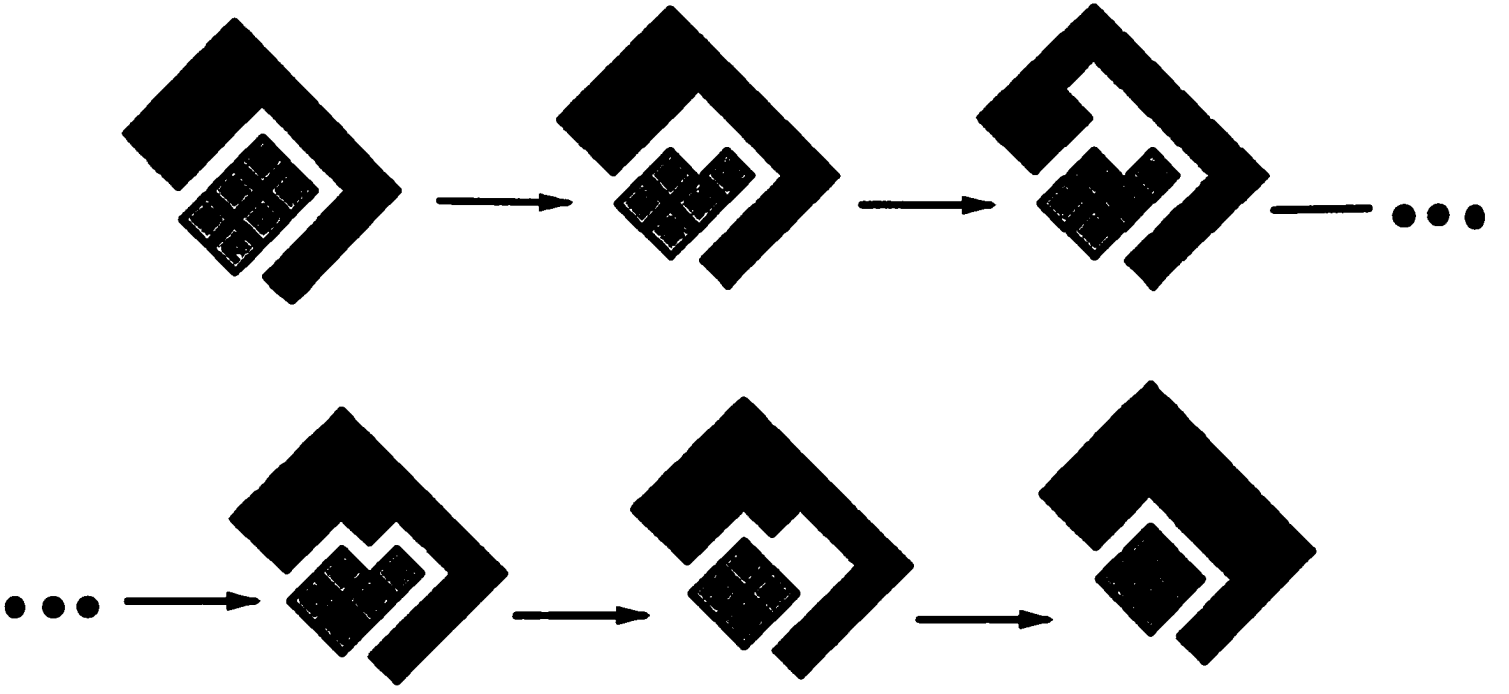

Figure 9. Schematic (using the hard-square representation) of the shrinkage of a highly curved portion of domain boundary. In this sequence, a total of three B-monomers are removed by reaction, and two B_2-dimers adsorb, yielding a net increase of one adsorbed B atom.

5.3 DIRECT ANALYSIS OF STEADY-STATE BEHAVIOR WHEN $P_{CO} \rightarrow 0+$

It is possible to develop a direct analysis for the (long-time) steady-state adlayer structure in the regime $P_{CO} \rightarrow 0+$. Here, the coarsening process yields a single domain on the + sublattice, say, so $\theta_O=[B]=[B_+]/2$ and $[B_-]=0$. This is consistent with the limiting order parameter value of $S=1$. Since the fraction of domain boundary vanishes ($F \rightarrow 0$), the limiting value of the coverage, $\theta_O=[B]= \frac{1}{2} - D \approx 0.42534$ is controlled by the density, $D \approx 0.07466$, of internal defects. Furthermore, this value of $\theta_O=[B]$ or D can be readily estimated noting that there must be a steady-state balance between the creation of defects due to removal of monomer B's, and the removal of defects via subsequent immediate deposition of dimer B_2's according to the eight-site rule. In fact, for each monomer removed, there must be a probability for dimer adsorption of 1/2, and thus also a probability for lack of adsorption of P=1/2. Furthermore, it is clear that P is given by the conditional probability, Q_+, that all four of the sites diagonally adjacent to a specific B_+ (which is removed by reaction) are occupied by B_+ (all on the + sublattice), that is

$$Q_+ = \begin{bmatrix} B_+ & & B_+ \\ & B_+ & \\ B_+ & & B_+ \end{bmatrix} / [B_+]. \qquad (15)$$

Thus, we estimate Q_+ with various assumptions regarding O(ads) or B-adlayer structure on the populated + sublattice. First, assume the defects are randomly distributed on the + sublattice. Then it follows that

$$Q_+ \approx [B_+]^4 = 2^4\,[B]^4 = P = 1/2, \qquad (16)$$

so $\theta_O=[B] \approx 2^{-5/4} \approx 0.4204$ in the steady-state. Second, we note that distribution of defects on the + sublattice must be correlated in any jammed state of the adlayer, since no two defects can be on adjacent sublattice sites (i.e., on diagonal NN sites of the square lattice of adsorption sites). Adopting a pair-type approximation, and exploiting the above observation, one obtains

$$Q_+ \approx \left[\begin{matrix} & B_+ \\ B_+ & \end{matrix}\right]^4 / [B_+]^4 = (2[B_+]-1)^4 / [B_+]^4 = (4[B]-1)^4 / (2[B]^4) = P = 1/2, \qquad (17)$$

so $\theta_O=[B] \approx (4-2^{3/4})^{-1} \approx 0.4314$ in the steady-state. Both these simple estimates are reasonably close to the "exact" simulation result of $\theta_O=[B]=0.42534$. A framework within which more sophisticated analytic determination can be made of this steady-state coverage, as well as of the kinetics discussed at the end of Sec.5.2, is presented in Appendix C.

6. SUMMARY

In this paper, we have analyzed the steady-state properties of a new "canonical" lattice-gas model for CO-oxidation which incorporates superlattice ordering of O(ads), as well as rapid mobility of CO(ads). As might be expected given the LH mechanism for this reaction, the steady-states exhibit bistability, a feature which is lost at a cusp bifurcation or "critical point" when the desorption rate d for CO(ads) exceeds a critical value. In Ref.[9], we have shown that behavior near this point is analogous to that near critical points in

equilibrium Hamiltonian systems, e.g., fluctuations in coverages are enhanced. The model also exhibits a symmetry-breaking order-disorder transition in the oxygen adlayer when θ_O exceeds a certain value. This behavior is analogous to order-disorder transitions in equilibrium systems such as the hard-square model [13]. This order-disorder transition replaces the unphysical (continuous) oxygen poisoning transition common in previous LG models for CO-oxidation without superlattice ordering [4,11]. Coarsening phenomena are also observed associated with symmetry breaking, reminiscent of Lifshitz-Cahn-Allen coarsening in Hamiltonian systems. Analogous behavior has been observed as a result of introducing relaxation processes into irreversible RSA models [23,24]. Both symmetry-breaking and coarsening will no doubt persist in more realistic and complicated reaction models which incorporate, e.g., CO(ads)-CO(ads) and CO(ads)-O(ads) interactions, in addition to strongly repulsive short-range O(ads)-O(ads) interactions.

ACKNOWLEDGEMENTS

This work was supported by the Division of Chemical Sciences, Office of Basic Energy Sciences, of the U.S. Department of Energy (USDOE). It was performed at Ames Laboratory, which is operated for the USDOE by Iowa State University under Contract No. W-7405-Eng-82.

APPENDIX A: DEPENDENCE OF STEADY-STATE BEHAVIOR ON REACTION RATE (k)

Steady-state behavior of our reaction model depends on the value of reaction rate, k. Thus, here we briefly comment on behavior for extreme regimes of low and high k, focusing on the case d=0 for which we identify the region of bistability, $0 \le P_{CO} \le P_{s+}(k)$.

First, consider the case $k \ll 1$, where the overall process is reaction-limited. The steady-state relation (7) shows immediately that $[A] \approx P_{CO}(P_{CO}+d)^{-1}(1-[B])$, so $[A]+[B] \approx 1$ when d=0. Thus, starting with an empty surface when d=0, one expects that the surface will almost completely fill on a time scale of order unity. Thereafter, each "slow" reaction event creates an empty pair of sites which are inevitably filled by A's, since the high coverage inhibits adsorption of B_2-dimers. Thus, one concludes that the surface will eventually become poisoned with A's. This suggests that $P_{s+}(k) \to 0$, as $k \to 0$. For d>0, the only possible steady-states must have sufficient O(ads) or B to create a jammed adlayer with no further eight-site adsorption ensembles (similar to behavior when $P_{CO} \to 0+$ for finite k>0). Otherwise, these ensembles would be available for B_2 adsorption with some finite probability, implying that further B_2 adsorption would occur before reaction, increasing [B], and thus contradicting the steady-state assumption. We conclude that in the steady-state for d>0, [B] must always exceed some critical value, thus yielding a rather different phase-diagram from that for k=1.

Second, consider the case $k \to \infty$ (instantaneous reaction), where the overall process is adsorption-limited. Rapid reaction, together with the infinite diffusion rate for CO(ads) or A in our hybrid model, implies that only one type of species can populate the surface

(cf. Ref.[12, 25]). If that populating species is CO(ads) or A (corresponding to a relatively inactive state), then it is randomly distributed, and as a result B_2 adsorbs at rate $2P_{O2}(1-[A])^2$ and immediately reacts. Thus, one has

$$d/dt\,[A] = P_{CO}(1-[A]) - d[A] - 2P_{O2}(1-[A])^2, \tag{18}$$

just as in the monomer-dimer model with B_2 adsorption on adjacent sites (for infinite diffusivity of A and $k\to\infty$) [25]. From equation (18), it follows that $P_{s+}(k)\to 2/3$, as $k\to\infty$. Behavior for $d>0$ can also be deduced from previous analysis of (18). See Ref.[25] for details.

If the populating species is O(ads) or B (corresponding to a reactive state), then A adsorbs at rate $P_{CO}(1-[B])=P_{CO}[Z]$, and reacts immediately removing a B. Thus, one has

$$d/dt[B] = 2P_{O2}\begin{bmatrix} & & Z & \\ & Z & Z & Z \\ Z & Z & Z & \\ & Z & & \end{bmatrix} - P_{CO}[Z]. \tag{19}$$

This is the first equation in a hierarchy, which can only be solved with further approximation to achieve closure [15]. Interestingly, this B-populated state of the adlayer is independent of d.

APPENDIX B: CHEMICAL WAVES AND RELATIVE STABILITY

Relative stability of coexisting stable states in reaction models is naturally defined in terms of the motion of planar chemical waves which separate these states: the more stable state should displace the less stable one. To apply this paradigm to our model, it is necessary to regard the hop rate(s) for CO(ads) as finite but very large, rather than being strictly infinite. Then, in spatially localized regions of the surface, the CO(ads) are randomized with a uniform coverage. However, spatial variations in coverage can occur on a macroscopic length scale controlled by the CO-diffusion coefficient. For low θ_{CO}, we denote this coefficient by D_0, and note that it scales with the hop rate(s) for an isolated CO(ads). For simplicity, let us denote the RHS of equation (4a) by R_A, and of (4b) by R_B. Then, chemical waves are described by the reaction-diffusion equations (cf. equation (4))

$$d/dt\,[A] = R_A - \nabla\cdot\underline{J}_A \text{ and } d/dt\,[B] = R_B, \text{ where } \underline{J}_A = - D_{CO,CO}\nabla[A] - D_{CO,O}\nabla[B]. \quad (20)$$

Here, ∇ denotes "grad" or "div" in the surface plane. The diffusive flux, $\underline{J}_A$, of CO(ads) or A includes a conventional term proportional to the gradient in [A] or θ_{CO}, as well as a typically neglected term proportional to the gradient in [B] or θ_O [3,8], as described below. The diffusive flux of O(ads) or B is set to zero ($\underline{J}_B=\underline{0}$) since O(ads) is immobile.

The diffusion coefficients $D_{CO,CO}$ and $D_{CO,O}$ have the specific form [8]

$$D_{CO,CO} = D_0\,F(\{B\}), \text{ and } D_{CO,O} = D_0\,[A]\,F(\{B\})/(1-[B]), \quad (21)$$

Here, we have exploited the feature that since the CO(ads) or A are non-interacting, it follows that $D_{CO,CO}$ depends only on the configuration, {B}, of the B or O(ads) adlayer, and not on [A]. Furthermore, the function F({B}) is unity for [B]=0, and F decreases with increasing [B] due to the blocking effect of B on A-diffusion (although detailed characterization of this decrease is a challenging problem [26]). We also note that $D_{CO,O}$ varies in exact proportion to the coverage of A or CO(ads). The specific form of $D_{CO,O}$ then follows from the simple observation that chemical diffusion is absent on a completely filled surface. Thus, the above form is chosen to guarantee that $\underline{J}_A=\underline{0}$ when [A]+[B]=1, which implies that $\nabla[A] = -\nabla[B]$. See Ref.[8].

General analysis of chemical waves requires detailed knowledge of F. However, near the cusp bifurcation, coexisting stable states become indistinguishable (with [B]→0.033 and [A]→0.633), as do all states across the chemical wave front. Thus, in this regime, one can perform an analysis of chemical wave propagation and relative stability treating $D_{CO,CO}$ and $D_{CO,O}$ in (20) as constants with $D_{CO,O}/D_{CO,CO} \approx 0.65$.

APPENDIX C: ANALYTIC FORMALISM FOR BEHAVIOR IN THE REGIME $P_{CO}\rightarrow 0+$

The discussion of Sec.5.3 motivates consideration of the following evolution problem. Starting from a jammed adlayer of B's on the + sublattice for c(2×2) ordering, single B's are removed at random (with rate unity on a time scale t′) followed by immediate adsorption of B_2 randomly on one of any eight-site ensembles thus created. Then, only the + sublattice is populated throughout the process, and $[B]=[B_+]/2$ evolves to about 0.42534.

We naturally consider the equivalent "sublattice problem" where one starts with a square grid filled with C's except for isolated vacancies. Then C's are randomly removed at rate unity on a time scale t′, and any adjacent empty pairs thus created are immediately filled by C_2 dimer adsorption (at adjacent empty sites). During evolution, the system remains in a "jammed" state with no adjacent pairs of vacancies. Let Q denote the conditional probability that a given C has four neighboring C's . Then, Q gives the probability that C_2 dimer adsorption does not occur following desorption of a C (yielding a net loss of one C), and 1-Q gives the probability that it does occur (yielding a net gain of one C). Thus one has,

$$d/dt' [C] = [C] \{(1-Q) - Q\} = [C] (1-2Q), \tag{22}$$

Of course, (22) is not closed, but rather the first in an infinite hierarchy. Similarly, one obtains

$$d/dt' [CC] = 2 [CC] (1-2Q), \quad \text{so } [CC] = 2[C]-1, \tag{23}$$

consistent with the lack of adjacent defect pairs in the jammed state. One can develop equations for probabilities of larger configurations of sites (e.g., the probability of finding a C surrounded by all four neighboring C's, which equals Q[C]). This hierarchy could be analyzed by various high-order truncation techniques [14]. The coverage [C] corresponds to $[B_+]$ above, and thus should evolve to about 0.85068. One can also identify Q with Q_+ in Sec.5.3, so (22) is consistent with the steady-state assignment of $Q_+=1/2$.

REFERENCES

[1] R. Imbihl and G. Ertl, Chem. Rev. **95**, 697 (1995).

[2] J. Wintterlin, S. Volkening, T.V.W. Janssens, T. Zambelli, and G. Ertl, Science **278**, 1931 (1997).

[3] M. Tammaro and J.W. Evans, Surf. Sci. Lett. **395**, L207 (1998).

[4] E.V. Albano, Hetero. Chem. Rev. **3**, 389 (1996); V.P. Zhdanov and B. Kasemo, Surf. Sci. Rep. **20**, 111 (1994); J.W. Evans, Langmuir **7**, 2514 (1991).

[5] W.H. Weinberg, Ann. Rev. Phys. Chem. **34**, 217 (1983); K. Binder and D.P. Landau, Adv. Chem. Phys. 91 (1989).

[6] J.W. Evans and T.R. Ray, Phys. Rev. E **50**, 4301 (1994).

[7] M. Tammaro, M. Sabella, and J.W. Evans, J. Chem. Phys. **103**, 10277 (1995).

[8] M. Tammaro and J.W. Evans, J. Chem. Phys. **108**, 762 (1998).

[9] Y. Suchorski, J. Beben, E.W. James, J.W. Evans, and R. Imbihl, Phys. Rev. Lett. **82**, 1907 (1999).

[10] C.R. Brundle, R.J. Behm, and J.A. Barker, J. Vac. Sci. Technol. A **2**, 1038 (1984); S.L. Chang and P.A. Thiel, Phys. Rev. Lett. **59**, 296 (1987).

[11] R.M. Ziff, E. Gulari, and Y. Barshad, Phys. Rev. Lett. **50**, 2553 (1986).

[12] V.P. Zhdanov and B. Kasemo, Surf. Sci. **412/413**, 527 (1998). The algorithm used in this study corresponds to first letting $k \to \infty$ (instantaneous reaction), and then letting the hop rate for CO-diffusion diverge. Thus, a CO(ads) reacts with the first O(ads) that it meets (which is more likely located at a protrusion rather than an indentation at oxygen islands edges). In our case, we first let the CO-hop rate diverge, so CO(ads) is always uniformly distributed, and reacts with equal probability with all O(ads)'s. One can then consider

behavior for large k (see Appendix A), but it is distinct from the above case of Zhdanov and Kasemo. Our model reflects the feature that the hop rates are far larger than all other rates, including k.

[13] F.H. Ree and D.A. Chesnut, J. Chem. Phys. **45**, 3983 (1966).

[14] J.W. Evans, Rev. Mod. Phys. **65**, 1281 (1993).

[15] J.W. Evans, J. Chem. Phys. **87**, 3038 (1987); J.W. Evans and D.E. Sanders, Phys. Rev. B **39**, 1587 (1989).

[16] LG-models with finite adspecies hop rates may mimic bistability, but can have only one stable steady state, perhaps a coexisting metastable steady state with a finite lifetime [6].

[17] R.M. Ziff and B.J. Brosilow, Phys. Rev. A **46**, 4630 (1992).

[18] Here, one finds that $[B]\sim\frac{1}{2}-\frac{1}{2}f^{1/2}(P_{CO})^{1/2}$, as $P_{CO}\rightarrow 0$, where $f=2k/(4k+d)$.

[19] E.W. James, Da-Jiang Liu, and J.W. Evans, to be submitted.

[20] S.M. Allen and J.W. Cahn, Acta. Met. **27**, 1085 (1979); I.M. Lifshitz, Sov. Phys. (JETP) **15**, 939 (1962).

[21] R.H. Goodman, D.S. Graff, L.M. Sander, P. Lerox-Hugon, and E. Clement, Phys. Rev. E **52**, 5904 (1995); H.C. Kang and W.H. Weinberg, *ibid*, **47**, 1604 (1993); **48**, 3464 (1994).

[22] A.-L. Barabasi and H.E. Stanley, "Fractal Concepts in Surface Growth" (Cambridge U.P., Cambridge, 1995).

[23] V. Privman, in *Annual Reviews of Computational Physics III*, edited by D. Stauffer (World Scientific, Singapore, 1995).

[24] E.W. James, Da-Jiang Liu, and J.W. Evans, Colloids and Surf. A., submitted for a special issue on *Adhesion of Submicron Particles on Solid Surfaces*, edited by V. Privman.

[25] J.W. Evans, J. Chem. Phys. **98**, 2463 (1993); J.W. Evans and M. Tammaro, in "Computer Simulation Studies in Condensed Matter Physics XI", edited by D.P. Landau and H.B. Schuettler (Springer, Berlin, 1998).

[26] Da-Jiang Liu and J.W. Evans, Bull. APS **44** (No.1), 1387 (1999), and in preparation.

CHAPTER 3. CO-OXIDATION MODEL WITH SUPERLATTICE ORDERING OF ADSORBED OXYGEN

II. FLUCTUATIONS AND CRITICAL PHENOMENA

A paper to be submitted to the Journal of Chemical Physics

E.W. James,[1,2] Da-Jiang Liu[1], J.W. Evans[1,2]

Ames Laboratory[1] and Department of Mathematics[2],

Iowa State University, Ames, Iowa 50011

ABSTRACT

We analyze critical phenomena in a simple reaction model for CO-oxidation on surfaces which incorporate both rapid diffusion of adsorbed CO, and superlattice ordering of adsorbed immobile oxygen (see Chapter 2). First, we show that the superlattice ordering produces a spontaneous symmetry-breaking transition for higher oxygen coverages, analogous to behavior in equilibrium systems with the corresponding superlattice ordering. We also analyze the relationship between this transition and percolation of the domains of adsorbed oxygen. Second, we show that the steady states of our model also exhibit a cusp bifurcation, from a regime of bistability to one of monostability, which is akin to a critical point in equilibrium systems. We analyze the increase in fluctuations near this transition, and elucidate the consequences for fluctuation-induced transitions.

1. INTRODUCTION

Lattice-gas models have traditionally been used to describe ordering in equilibrated chemisorbed adlayers [1], but more recently it has been recognized that they have the potential to describe analogous ordering in non-equilibrium surface reactions [2,3]. However, it is often not recognized that suitable or realistic reaction models must typically incorporate very high mobility of at least some adspecies, as well as suitable interactions between adspecies [2,4]. To this end, we recently introduced a "canonical" model for CO-oxidation which is still simplistic, but nonetheless incorporates both rapid diffusion of adsorbed CO, and superlattice ordering of adsorbed immobile oxygen [4,5] (the latter feature deriving from strong repulsive interactions between neighboring adsorbed oxygen atoms).

The most commonly studied lattice-gas reaction model for CO-oxidation [6] exhibits some features quite distinct from equilibrium systems, such as an "oxygen poisoning transition" which is in the universality class of "directed percolation". However, this feature is due to somewhat artificial simplifications in the model. Interestingly, we find that for our more realistic model with superlattice ordering, behavior is much more akin to equilibrium systems. Specifically, the superlattice ordering produces a spontaneous symmetry-breaking transition [5], analogous to behavior in equilibrium systems with superlattice ordering such as the hard-square model [7]. It is also well recognized that allowing desorption of adsorbed CO in lattice-gas reaction models for CO-oxidation produces either a cusp bifurcation (in models with highly mobile CO which exhibit bistabilility) or the disappearance of a discontinuous transition (in models with finite mobility of CO). This phenomenon is

analogous to a critical point in equilibrium systems. In this paper, we examine in some detail both these types of critical phenomena for our reaction model.

In section 2, we first specify our reaction model in more detail, and then develop exact master equations, which describe model behavior in the most general case of a spatially non-uniform distribution of adsorbed oxygen. Our Monte Carlo simulation procedures are also described. In section 3, we provide a comprehensive analysis of the spontaneous symmetry-breaking transition, and of associated percolation issues. Next, in section 4, we analyze critical phenomena associated with the cusp bifurcation point in our model. Finally, a brief summary is provided in section 5.

2. REACTION MODEL AND EXACT MASTER EQUATIONS (INCORPORATING SPATIAL INHOMOGENEITY)

2.1 LANGMUIR-HINSHELWOOD (LH) MECHANISM AND ADLAYER STRUCTURE

In this study, we consider exclusively surfaces characterized by a square lattice of adsorption sites, with periodic boundary conditions. We adopt a conventional LH mechanism for CO-oxidation as indicated below, where "gas" denotes a gas phase species, and "ads" an adsorbed phase species (see also figure 1):

(i) CO(gas) adsorbs at single empty sites at rate P_{CO}, and CO(ads) desorbs at rate d;

(ii) O_2(gas) adsorbs dissociatively at diagonal nearest-neighbor (NN) empty sites at rate $\frac{1}{2} P_{O2}$, provided that all six additional NN sites to these are unoccupied by O(ads).

Furthermore, O(ads) does not desorb and is assumed immobile. The latter feature, together

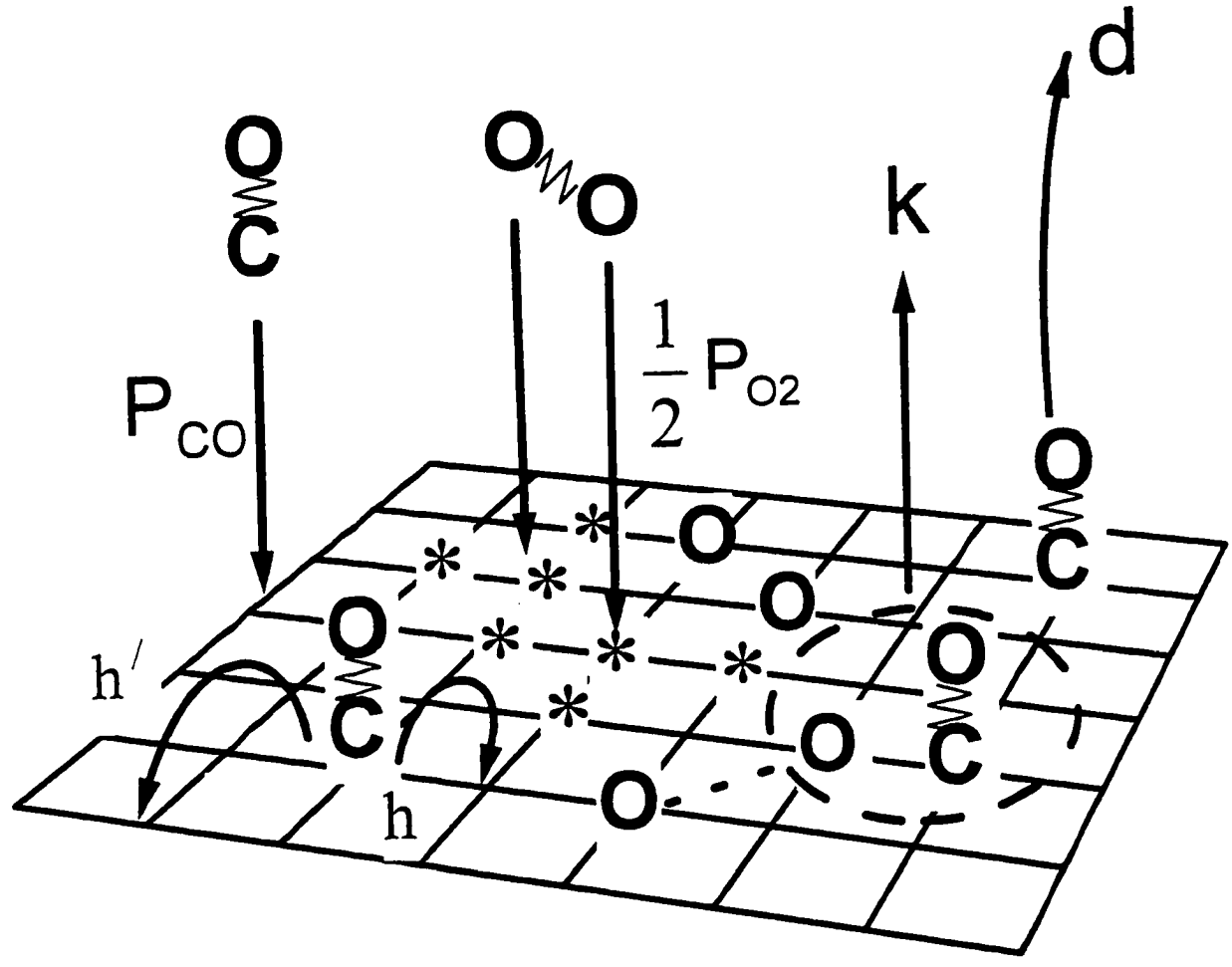

Figure 1. Schematic of the reaction model illustrating the various mechanistic steps, together with their rates. For the O_2(gas) adsorption event, the eight sites required to be unpopulated by O(ads) are indicated by *. The dotted line between two O(ads) indicates that they were associated with the same molecule. CO(ads) is shown to hop to NN empty sites at rate h, and to next NN empty sites at rate h′, where in our model both $h \to \infty$ and $h' \to \infty$ (but h′/h can have any limiting value).

with the adsorption rule, ensures that no adjacent pairs of O(ads) are created during the process.

(iii) CO(ads) is assumed highly mobile (e.g., via rapid hops to NN and diagonal NN empty sites), and is assumed randomly distributed on sites not occupied by O(ads);

(iv) Adjacent CO(ads) and O(ads) react at rate k.

Our prescription of oxygen adsorption is termed the "eight-site rule" since an ensemble of eight sites not occupied by O(ads) are required for adsorption. This rule was originally applied to describe dissociative adsorption of oxygen on Ni(100) and Pd(100) [10]. The "eight-site rule" reflects strong NN O(ads)-O(ads) repulsive interactions, resulting in superlattice ordering often observed in real systems. With rare exceptions [4,9], this feature has not been incorporated into most previous LG modeling of CO-oxidation, where oxygen adsorption was assumed to occur on adjacent (NN) empty sites [3,6,10–12]. We emphasize that implicitly our model still neglects CO(ads)-CO(ads) and CO(ads)-O(ads) interactions, since we assume that CO(ads) is randomly distributed on non-O(ads) sites. Certainly such interactions are present to some extent, and will affect behavior in real systems.

Next we discuss further the model parameters, and our assignment of their values. Note that P_{CO} corresponds to the impingement rate per site for CO(gas). Also, since there are two diagonal NN pairs of sites for each single site on the square lattice, P_{O2} corresponds to the impingement rate per site for O_2(gas). Below we choose $P_{CO}+P_{O2}=1$ (which sets the time scale), and set k=1 when presenting specific results. We denote the coverage of CO(ads) by

θ_{CO}, of O(ads) by θ_O, and the total coverage by $\theta=\theta_{CO}+\theta_O$ (where these quantities are measured in units of monolayers).

Finally, we briefly comment on and illustrate some basic features of the ordering in the oxygen adlayer. Since the kinetic rules of the reaction model preclude the formation of NN O(ads)-pairs, the oxygen adlayer tends to display "checkerboard" or centered-two-by-two [c(2×2)] ordering, especially for higher coverages of O(ads). This is analogous to behavior in an equilibrium "hard-square model" where adspecies have infinitely repulsive NN interactions [13]. As shown in figure 2, c(2×2) domains have degeneracy two, atoms in domains of different phase residing on one of two interpenetrating "sublattices". (The latter terminology is adopted from equilibrium statistical mechanics, although it is potentially confusing here as atoms in a populated sublattice exhibit superlattice ordering!) In addition, individual domains can have "internal defects", that is sites not occupied by O(ads) which are surrounded by four diagonal adjacent O(ads).

2.2 COVERAGE/CONCENTRATIONS DEFINITIONS/PRELIMINARIES

Despite the feature that our model incorporates non-trivial spatial correlations in the distribution of O(ads), it is possible to write down a formally exact hierarchy of master equations describing the reaction kinetics and the probabilities of various local configurations of O(ads). We first introduce some definitions and notations used in these equations and in later sections. For notational simplicity, we denote CO(ads) by A, O(ads) by B, and we let E correspond to empty sites, and Z correspond to sites not occupied by B.

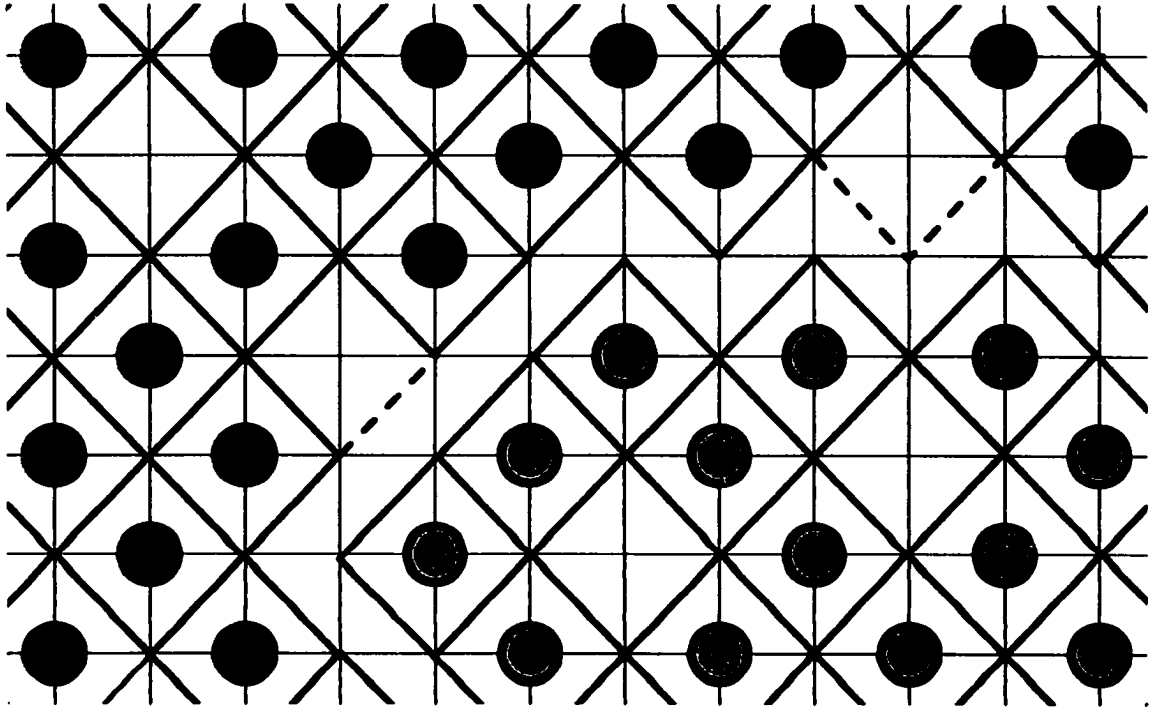

Figure 2. Schematic of the configuration of oxygen atoms in a jammed state. Atoms in two adjacent c(2×2) domains of different phase are indicated by black and gray circles. Also shown is the "hard-square representation", where atoms are replaced by diamonds. This representation highlights both the three internal defects, as well as the domain boundary, which is decorated by two external defects (indicated by dashed lines).

We consider the most general case where the distribution of B is spatially non-uniform, but A is still uniformly and randomly distributed over non-B (or Z) sites. Labelling the sites on the finite or infinite square lattice by (i,j), we then let $[A_{ij}]$, $[B_{ij}]$, $[E_{ij}]$, and $[Z_{ij}]$ denote the ensemble average of the coverage of the site (i,j) by A, B, empty, or not B, respectively. We can also represent the probabilities (ensemble averages) of more spatially complex configurations. For instance, $[A_{ij}\ B]$ denotes the probability of the event that site (i,j) is occupied by A and that its right-hand NN site (i+1,j) is occupied by B. Similarly, $[B\ A_{ij}]$ denotes the probability of the event that site (i,j) is occupied by A and that its left-hand NN site (i−1,j) is occupied by B. Probabilities of other spatial configurations are denoted in a similar manner.

We may also drop the "ij" subscript to denote spatial average probabilities by writing: $[J] = \underset{(i,j)}{\text{avg}}[J_{ij}]$, where the averages are computed over all (i,j) sites, and J = A, B, E, or Z.

Some especially useful relations, obtained by using conservation of probability, are:

$$[A_{ij}] + [B_{ij}] + [E_{ij}] = 1 \quad \& \quad [A] + [B] + [E] = 1, \qquad \text{eq. 1(a)}$$

$$\text{and} \quad [E_{ij}] = [Z_{ij}] - [A_{ij}] \quad \& \quad [E] = [Z] - [A], \qquad \text{eq. 1(b)}$$

$$\text{since} \quad [Z_{ij}] = 1 - [B_{ij}] \quad \& \quad [Z] = 1 - [B]. \qquad \text{eq. 1(c)}$$

Also, we note that, due to the spatially uniform distribution of the A's on non-B sites, the following two relations can be derived (See Appendix B):

$$\frac{[A_{ij}]}{[Z_{ij}]} = \frac{[A]}{[Z]} \quad \text{and} \quad \frac{[E_{ij}]}{[Z_{ij}]} = \frac{[E]}{[Z]}. \qquad \text{eq. 2}$$

Finally, one special case we explore, in some detail, is the "symmetry-breaking" which occurs when the populations of O(ads) or B on the two c(2×2) sublattices are uniform, but unequal. We refer to the sublattice of sites in which i + j = even as the even sublattice, and the sublattice of sites in which i + j = odd is called the odd sublattice. We then define each of the subpopulation concentrations, $[B_+]$ and $[B_-]$, as the concentration of B-atoms on the even and odd sublattice, respectively, the value of which lies between zero and one (i.e. $0 \leq [B_-], [B_+] \leq 1$). Put another way, we have:

$$[B_{ij}] = \begin{cases} [B_+], & \text{if} \quad i+j = \text{even}, \\ [B_-], & \text{if} \quad i+j = \text{odd}. \end{cases} \qquad \text{eq. 3}$$

Normally, a system is in a symmetric state, that is, one in which any possible site-configuration in the even sublattice must have the same probability as the corresponding one in the odd sublattice (e.g. $[B_-] = [B_+]$, $\begin{bmatrix} B_+ & \\ & B_+ \end{bmatrix} = \begin{bmatrix} B_- & \\ & B_- \end{bmatrix}$, and etc.). However, under certain conditions, or with the right parameters, there are systems in which some or all of these equalities do not hold, and this corresponds to the symmetry-breaking phenomenon, referred to above.

We shall find the following equalities useful, later. The average spatial coverage [B] may be expressed in terms of the subpopulation coverages $[B_+]$ and $[B_-]$ as follows:

$$[B]=\frac{1}{2}([B_+]+[B_-]). \qquad \text{eq. 4}$$

In addition, by conservation of probability, we have the following useful relation:

$$[Z_+ Z_-] + [B_+ Z_-] + [Z_+ B_-] + [B_+ B_-] = 1. \qquad \text{eq. 5}$$

Because of the exclusion of adjacent B-atoms, we have:

$$[B_+ Z_-] = [B_+], \quad \text{and} \quad [Z_+ B_-] = [B_-], \quad \text{and} \quad [B_+ B_-] = 0, \qquad \text{eq. 6}$$

which we employ to simplify eq. 5 as follows:

$$[Z_+ Z_-] = 1 - [B_+] - [B_-]. \qquad \text{eq. 7}$$

2.3 EXACT MASTER EQUATIONS AND RESULTS

Using the above notation, the exact master equations describing the reaction kinetics of our model may be written as the following two sets of coupled rate equations:

$$\frac{d}{dt}[A_{ij}]=P_A[E_{ij}]-d[A_{ij}]-k\left\{[A_{ij}B]+[BA_{ij}]+\left[\begin{matrix}B\\A_{ij}\end{matrix}\right]+\left[\begin{matrix}A_{ij}\\B\end{matrix}\right]\right\}, \text{ and} \qquad \text{eq. 8(a)}$$

$$\frac{d}{dt}[B_{ij}] = \frac{P_B}{2}\left\{\begin{bmatrix} & Z & \\ Z & E_{ij} & Z \\ & Z & \end{bmatrix} + \begin{bmatrix} & Z & \\ Z & E & Z \\ & Z & E_{ij} \end{bmatrix} + \begin{bmatrix} & & Z \\ Z & E_{ij} & Z \\ & Z & E \end{bmatrix} + \begin{bmatrix} & Z & \\ Z & E_{ij} & Z \\ & Z & E \end{bmatrix}\right\} \qquad \text{eq. 8(b)}$$

$$- k\left\{[B_{ij}\, A] + [A\, B_{ij}] + \begin{bmatrix} A \\ B_{ij} \end{bmatrix} + \begin{bmatrix} B_{ij} \\ A \end{bmatrix}\right\},$$

where the positive and negative terms indicate the rates of gain due to adsorption and loss due to reaction or desorption, respectively.

Using conditional probabilities, we can obtain refined exact expression for the reaction rate terms of eq. 8(a,b) and the adsorption terms in eq. 8(b). Below, we have demonstrated this for two such terms:

$$[A_{ij}\, B] = \frac{[A_{ij}]}{[Z_{ij}]}[Z_{ij}\, B] = \frac{[A]}{[Z]}[B_{i+1,j}] \qquad \text{eq. 9(a)}$$

$$\begin{bmatrix} & Z & \\ Z & E_{ij} & Z \\ & Z & \end{bmatrix} = \frac{[E_{ij}]}{[Z_{ij}]}\frac{[E_{i+1,j-1}]}{[Z_{i+1,j-1}]}\begin{bmatrix} & Z & \\ Z & Z_{ij} & Z \\ & Z & \end{bmatrix} = \left(\frac{[E]}{[Z]}\right)^2\begin{bmatrix} & Z & \\ Z & Z_{ij} & Z \\ & Z & \end{bmatrix} \qquad \text{eq. 9(b)}$$

Using eq. 9(a,b), the master equations reduce to the following (still exact) relations:

$$\frac{d}{dt}[A_{ij}] = P_A[E_{ij}] - d[A_{ij}] - k\frac{[A]}{[Z]}\{[B_{i+1,j}] + [B_{i-1,j}] + [B_{i,j-1}] + [B_{i,j+1}]\} \qquad \text{eq. 10(a)}$$

$$\frac{d}{dt}[B_{ij}] = \left(\frac{P_B}{2}\right)\left(\frac{[E]}{[Z]}\right)^2 \left\{ \begin{bmatrix} & Z & \\ Z & Z & Z \\ & Z & \end{bmatrix} + \begin{bmatrix} & Z & \\ Z & Z & Z \\ & Z & \end{bmatrix} + \begin{bmatrix} & Z & \\ Z & Z & Z \\ & Z & \end{bmatrix} + \begin{bmatrix} & Z & \\ Z & Z & Z \\ & Z & \end{bmatrix} \right\} \qquad \text{eq. 10(b)}$$

$$-4k\frac{[A]}{[Z]}[B_{ij}]$$

We may compute the spatial average of both eq. 10(a) and (b) over all (i,j) pairs, and obtain:

$$\frac{d}{dt}[A] = P_A[E] - d[A] - 4k\frac{[A][B]}{[Z]} \qquad \text{eq. 11(a)}$$

$$\frac{d}{dt}[B] = P_B\left(\frac{[E]}{[Z]}\right)^2 \left\{ \begin{bmatrix} & Z & \\ Z & Z & Z \\ & Z & \end{bmatrix} + \begin{bmatrix} & Z & \\ Z & Z & Z \\ & Z & \end{bmatrix} \right\} - 4k\frac{[A]}{[Z]}[B] \qquad \text{eq. 11(b)}$$

We note that eq. 11(a) is equivalent to equation (4a) of Paper I, which we obtained when we considered only a spatially uniform, rotationally invariant system. Thus, the steady-state [A] coverage, which is obtained by setting eq. 11(a) equal to zero, satisfies the same relation as the result obtained in Paper I, equation (7), namely:

$$[A] = \frac{P_A(1-[B])}{P_A + d + \dfrac{4k[B]}{1-[B]}}$$, where we eliminate [Z] by usingeq. 1(c). eq. 12

If, in addition, we assume rotational invariance of the B distribution, then eq. 11(b) also reduces to the equation obtained in Paper I. In particular, we would have:

$$\begin{bmatrix} & Z & \\ Z & Z & Z \\ Z & Z & Z \\ & Z & \end{bmatrix} = \begin{bmatrix} & Z & & \\ Z & Z & Z & \\ & Z & Z & Z \\ & & Z & \end{bmatrix}, \text{ which would reduce eq. 11(b) to} \qquad \text{eq. 13}$$

$$\frac{d}{dt}[B] = 2P_B\left(\frac{[E]}{[Z]}\right)^2 \begin{bmatrix} & Z & \\ Z & Z & Z \\ Z & Z & Z \\ & Z & \end{bmatrix} - 4k\frac{[A][B]}{[Z]}, \qquad \text{eq. 14}$$

which is precisely equivalent to equation (4b) of Paper I.

One special case of eq. 10, which we explore in section 3, is the symmetry-breaking situation defined in section 2.2. In particular, using the definition given in eq. 3, and restricting ourselves to the rotationally invariant case, the relations in eq. 10 then reduce to a set of three coupled equations which describe the symmetry-breaking of [B] coverages:

$$\frac{d}{dt}[A] = P_A[E] - d[A] - 4k\frac{[A][B]}{[Z]} \qquad \text{eq. 15(a)}$$

$$\frac{d}{dt}[B_-] = 2P_B\left(\frac{[E]}{[Z]}\right)^2 \begin{bmatrix} & Z_+ & \\ Z_+ & Z_- & Z_+ \\ & Z_+ & \end{bmatrix} - 4k\frac{[A]}{[Z]}[B_-] \qquad \text{eq. 15(b)}$$

$$\frac{d}{dt}[B_+] = 2P_B\left(\frac{[E]}{[Z]}\right)^2\left[\begin{array}{ccc} & Z_- & \\ Z_- & Z_+ & Z_- \\ & Z_- & \end{array}\right] - 4k\frac{[A]}{[Z]}[B_+] \qquad \text{eq. 15(c)}$$

We note that, despite this system's complexity, we may readily obtain the symmetric case as one solution to the system given in eq. 15. This is because of the equality $[B_+]$ and $[B_-]$ and of the eight-site configuration probabilities in eq. 15(b,c) in a symmetric system. We shall later observe (in section 3.3) that this symmetric solution is unstable for low pressure, P_A. For either the symmetric or the symmetry-breaking solution, there is, unfortunately, no simple exact expression for the configuration of eight Z's appearing in the RHS of each of eq. 15(b) and (c). However, in Section 3.2, we make some approximations to obtain a closed set of equations from eq. 15 in a similar way as treated in Paper I.

2.4 SIMULATION PROCEDURES AND PHASE DIAGRAM DESCRIPTION

We performed a hybrid simulation process to determine precisely the properties of this model. "Specifically, for O(ads) or B, one performs a conventional simulation, tracking the position of every particle on the lattice. However, for the CO(ads) or A, one simply keeps track of the total number of adsorbed particles. From this and the number of Z-sites (not occupied by B), one can calculate the instantaneous probability that any Z-site is occupied by A. This probability is then used in determining which specific adsorption, desorption, and reaction events must take place."[5]

Our lattice is a square LxL grid (L = 2K, an even number) with periodic boundary conditions and sites labeled by $\underline{\ell} = (i,j)$. It is instructive to define the occupation number for species B on site $\underline{\ell}$, by:

$$n_{\underline{\ell}}^{B} = \begin{cases} 1, & \text{if } \underline{\ell} \text{ is occupied by B;} \\ 0, & \text{else.} \end{cases} \qquad \text{eq. 16}$$

We then obtain the total number of B's (N_B) and the instantaneous concentration of B (θ_B), for a single simulation trial by:

$$N_B = \sum_{\underline{\ell}} n_{\underline{\ell}}^{B}, \qquad \text{and} \qquad \theta_B = \frac{N_B}{N}, \qquad \text{eq. 17}$$

where $N = L^2$ = lattice size, and the summation is taken over all lattice sites, $\underline{\ell} = (i,j)$. Then formally we have, for the average ensemble concentration of the B species:

$$[B] = \underset{(i,j)}{\text{avg}}\,[B_{ij}] = \frac{\sum_{\underline{\ell}} \langle n_{\underline{\ell}}^{B} \rangle}{N} = \langle \theta_B \rangle, \quad \underline{\ell} = (i,j); \qquad \text{eq. 18}$$

where the angle-brackets indicate an average computed over an ensemble simulation on LxL lattices.

In order to discuss a symmetry-breaking system, we also define N_{B_+} and N_{B_-} to be the number of B-atoms occupying the even and odd sublattices, respectively. Then, the instantaneous concentration of B atoms on even and odd sublattices are given by:

$$\theta_B^+ = \frac{N_{B_+}}{N/2}, \qquad \text{and} \qquad \theta_B^- = \frac{N_{B_-}}{N/2}. \qquad \text{eq. 19}$$

We note that the division by two in the denominator of either of these expressions is safe, since where $N = L^2$, where L is an even number. In terms of our average concentration notations, we thus have $[B_+] = \langle \theta_B^+ \rangle$, and $[B_-] = \langle \theta_B^- \rangle$, where the angle brackets denote the ensemble average.

We show the results of these simulations for the steady-state behavior or "phase diagram" in figure 3, as in Paper I. Again, we note the "existence of bistability in the steady-states of the reaction model for $d<d_c$, where $d=d_c$ corresponds to a cusp bifurcation or 'critical' point. Specifically, for $d<d_c$, a reactive stable state with low [A] and high [B] coexists with a relatively inactive stable state with high [A] and low [B], for a range of P_A. These two states are "connected" by an unstable state. This range of bistability is denoted by $P_{s-}<P_{CO}<P_{s+}$, where $P_{s\pm}$ are upper and lower saddle-node bifurcations or 'spinodals' (except that when d=0, $P_{s-}=0$ corresponds to a transcritical bifurcation)" [5]. For selected d-values, the left and right endpoints of the range of bistability for P_A, with extrapolated values at the critical point dc, are summarized in table 1, along with corresponding [A] and [B] concentrations. In particular, for d = 0, the range of bistability is given by the interval

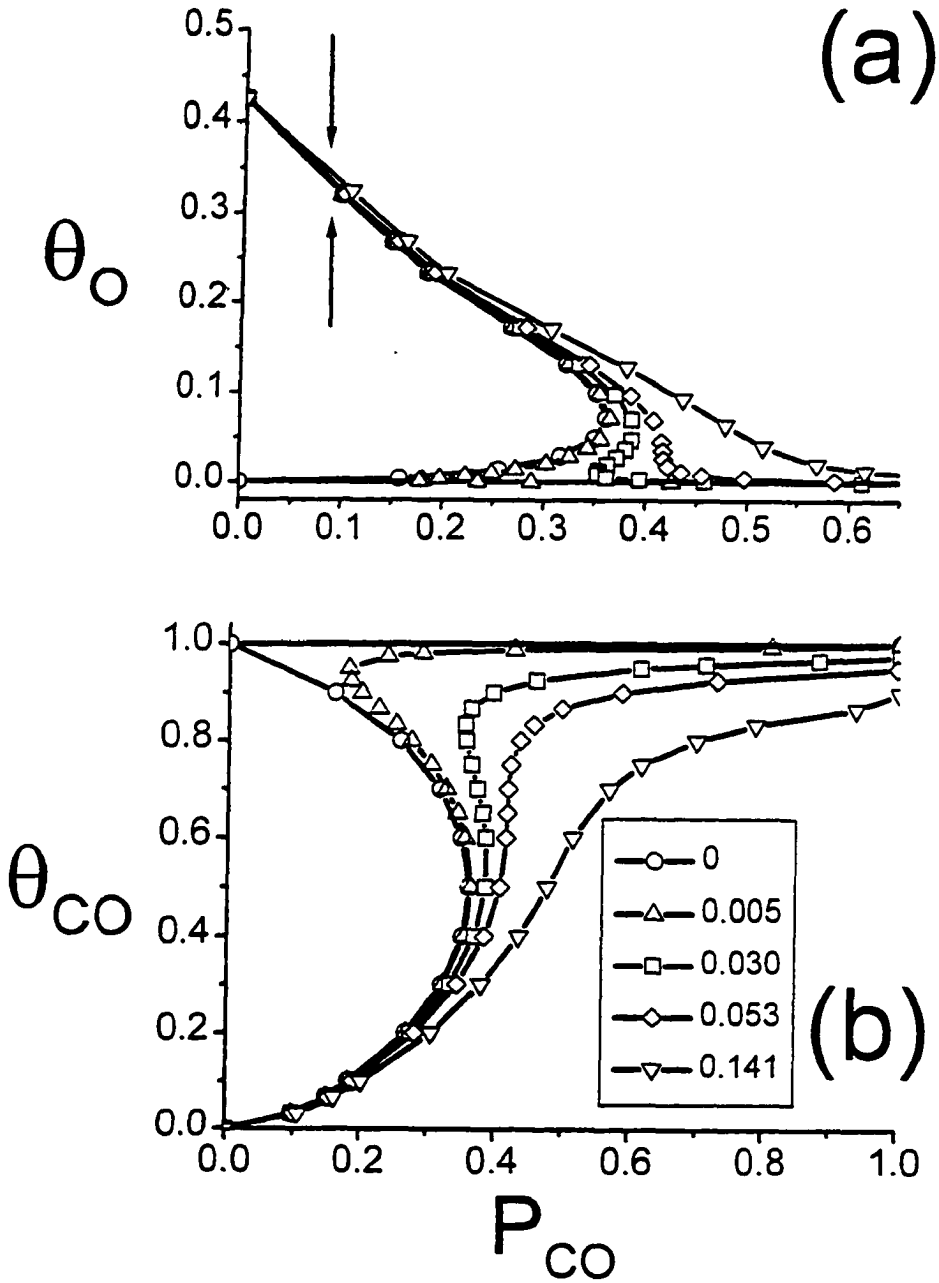

Figure 3. Steady-state "phase diagram" predicted by constant-coverage ensemble simulations showing the variation with P_{CO} of: (a) θ_O; and (b) θ_{CO}, for various fixed d (shown), and k=1. The arrows in (a) indicate the location of the symmetry-breaking transition, as discussed in section 3

Table 1. For selected d-values, the left and right endpoints of the range of bistability for P_A, with extrapolated values at the critical point, d_c, are summarized here, along with corresponding [A] and [B] concentrations.

d	$P_{CO}(+)$	[CO]	[O]
0	0.3604	0.5	0.07166
0.005	0.3642	0.5	0.07133
0.018	0.376	0.529	0.06358
0.03	0.3874	0.55	0.05797
0.04	0.3978	0.6	0.04636
0.045	0.4039	0.6	0.04608
0.05	0.4098	0.62	0.04173
0.051	0.411	0.633	0.03893
0.052	0.4124	0.65	0.03556
0.053	0.4139	0.653	0.03494

d	$P_{CO}(-)$	[CO]	[O]
0	0	1	0
0.005	0.1781	0.95	0.00104
0.018	0.2957	0.871	0.00591
0.03	0.3527	0.833	0.00913
0.04	0.3866	0.8	0.01249
0.045	0.398	0.75	0.01902
0.05	0.4087	0.704	0.02599
0.051	0.4104	0.7	0.0266
0.052	0.4123	0.684	0.02932
0.053	0.4138	0.674	0.03103
0.05327 ± 0.0005	0.4143	0.6627 ± 0.005	0.03334 ± 0.0005

(extrapolated values)

$0 \leq P_A < 0.3604$, with the saddle-node bifurcation at $P_A \cong 0.3604$, where the bistability is lost. The inactive (or poisoned branch) corresponds to concentration values of [B] = 0 and [A] = 1.

Two interesting features not displayed by the steady-state phase diagrams, are the symmetry-breaking of the B-atom concentrations for low values of P_A, and the high amplitudes of fluctuation in the instantaneous coverages concentrations θ_A and θ_B near the cusp bifurcation. In section 3, we discuss the symmetry-breaking phenomenon in some detail for the special case when d = 0, noting that we believe similar symmetry-breaking must occur for nonzero d. We leave the study of fluctuations for section 4.

3. SPONTANEOUS SYMMETRY-BREAKING TRANSITION FOR C(2×2) O(ADS)

3.1 BASIC CONCEPTS AND DEFINITIONS

On the reactive branch of the phase diagram, as we lower the impingement rate, P_A, of A-species landing on the lattice, the steady-state coverage of the B-atoms correspondingly increases (see figure 3(b)). Since the eight-site rule disallows two B-atoms to occupy NN-sites simultaneously, then once the [B] concentration gets sufficiently high, the system becomes more "comfortable" or less crowded by breaking symmetry and populating the sublattices unequally.

Previous work has shown that the model exhibits symmetry-breaking for small values of P_A near zero, and is symmetric for large values of P_A. A natural question which arises is, "as P_A decreases to zero, at what point does symmetry-breaking begin to occur?" We study three different quantities in an attempt to answer this question: (1) the symmetry-breaking

order parameter, S; (2) the fluctuations in the difference between the even and odd B-atom concentrations, θ_B^+ and θ_B^-; and (3) the 2NN-cluster size. We first define each of these quantities below, and then discuss our simulation results in section 3.2.

We recall from section 2.2 that, for a symmetry-breaking lattice, there exists a site-configuration in the even sublattice, which does not occur with the same probability as its odd sublattice counterpart. In practice, this means that the concentrations of the B-atoms on the even and odd sublattices are different (i.e. $[B_+] \neq [B_-]$). Thus, it is natural to define the symmetry-breaking order parameter, S, as follows:

$$S = \frac{|[B_+] - [B_-]|}{[B_+] + [B_-]}. \qquad \text{eq. 20}$$

The denominator normalizes S, so that $0 \leq S \leq 1$. A symmetric system would yield an order parameter value of $S \approx 0$, while a symmetry-breaking lattice should yield $S > 0$.

We next turn our attention to the second of our quantities, which can also be used to locate the symmetry-breaking point, namely the fluctuations in $\theta_B^+ - \theta_B^-$. Heuristically, as the lattice approaches symmetry-breaking point, the B-atoms form large even and odd subdomains, which compete with each other for space on the lattice. Thus, some of the time the even subpopulation dominates the odd, at other times the odd subpopulation dominates the even, with the even and odd B-atom concentrations approximately balancing each other during the transitions. This causes the fluctuations of the difference $\theta_B^+ - \theta_B^-$ about its

average value to become much bigger at the symmetry-breaking transition. To measure these fluctuations, we use the quantity:

$$S_2 = N\left\langle \left\{ \theta_B^+ - \theta_B^- - \left\langle \theta_B^+ - \theta_B^- \right\rangle \right\}^2 \right\rangle, \text{ where } N = L^2 = \text{size of lattice.} \qquad \text{eq. 21}$$

We introduce the factor of N in eq. 21 since the fluctuations should be approximately inversely proportional to the system size.

Finally, since we expect the even and odd subdomains to grow larger as the lattice approaches the symmetry breaking point, we are motivated to study suitably defined subdomain or cluster sizes. Formally, we say that two B-atoms are 2NN-connected if they are diagonally adjacent. We then define a 2NN-cluster to be a collection of B-atoms, each of which is linked to every other B-atom in the collection by a series of 2NN-connections. A key related quantity of interest is thus the percolation point (the point at which the 2NN-clusters grow large enough to span the entire lattice). We measure the average 2NN-cluster size using the following formula, which is the standard definition from percolation theory:

$$\text{Avg}_1 = \frac{\sum_\sigma \sigma^2 N_\sigma}{\sum_\sigma \sigma N_\sigma}, \quad \sigma = \text{2NN-cluster size}, \qquad \text{eq. 22}$$

where each sum in eq. 22 is taken over all possible 2NN-cluster sizes, σ, and N_σ refers to the number of 2NN-clusters of size σ.

For a finite lattice, we recall from Paper I that, as $P_A \rightarrow 0^+$, the B-atoms form one large 2NN-cluster with a concentration of [B]→0.425, from the left. Thus, as P_A decreases to zero, we have that Avg_1 increases toward a value of about $0.425*L^2$, where L is the length of the side of the square lattice. In contrast, if we disregard the largest 2NN-cluster, then the average 2NN-cluster size tends to zero, independently of side length, L. Hence, we find it useful to define the <u>average 2NN-cluster size without the largest cluster</u>:

$$Avg_2 = \frac{\sum_{\sigma}^{*} \sigma^2 N_\sigma}{\sum_{\sigma}^{*} \sigma N_\sigma}, \quad \sigma = \text{2NN–cluster size}, \qquad \text{eq. 23}$$

where $\sum^{*}$ indicates that the summation is taken over all clusters, excluding a single largest one.

For a finite system, symmetry-breaking is not well-defined, and there is no precise relation to percolation. However, for a very large or infinite lattice, there are well-defined symmetry-breaking and percolation points which we denote by P_A^{Sym} and P_A^{Perc}, respectively. It turns out that these two quantities are not necessarily the same. In fact, we now argue that $P_A^{Perc} \leq P_A^{Sym}$.

First, we claim that, for a very large (or infinite lattice), 2NN-percolation <u>does</u> imply symmetry-breaking. We give the following topological argument. Assume the system percolates, but that there is no symmetry-breaking. For a very large system which percolates, say, with an even 2NN-cluster from left to right, then from a statistical standpoint, the same

even cluster must also percolate up and down. The result is that, either no B-atoms remain on the odd sublattice, or else the odd 2NN-clusters have been divided into at least one piece, none of the pieces of which can possibly span the lattice, or percolate (see figure 4). In either case, since the even sublattice percolates while the odd sublattice does not, this contradicts our assumption of no symmetry-breaking. Therefore, it is not possible to have percolation and not have symmetry-breaking. In other words, percolation implies symmetry-breaking, for a very large lattice (or infinite lattice).

Thus, we have struck out the last arrangement in the list of the three possibilities in figure 5. The remaining two possibilities lead us to conclude that $P_A^{Perc} \leq P_A^{Sym}$. The simulation results of section 3.2 will suggest that, perhaps, this inequality is strict.

3.2 SIMULATION RESULTS (d = 0):

In figures 6–9, we have plotted each of the four quantities S, S_2, Avg_1, and Avg_2, versus P_{CO}, for each of four different lattice sizes: 16×16, 32×32, 64×64, 128×128. Each data point is a time-averaged quantity, with the average computed over a range from 4,000 to 128,000 physical time units in the model. As the size of the lattice increases, we observe the peaks becoming sharper and the "jumps" becoming steeper, thus yielding an insight into the limiting behavior of these quantities for a very large or infinite lattice.

We have found that for lower values of P_A, it takes a very long time (more than 4,000 time units) for a large system to evolve from an initially empty lattice into its naturally symmetry-broken steady-state. In fact, it is more advantageous, for low P_A, to start with an initial lattice consisting of a perfect checkerboard configuration of B-atoms (say, $[B_+] = 1$ and

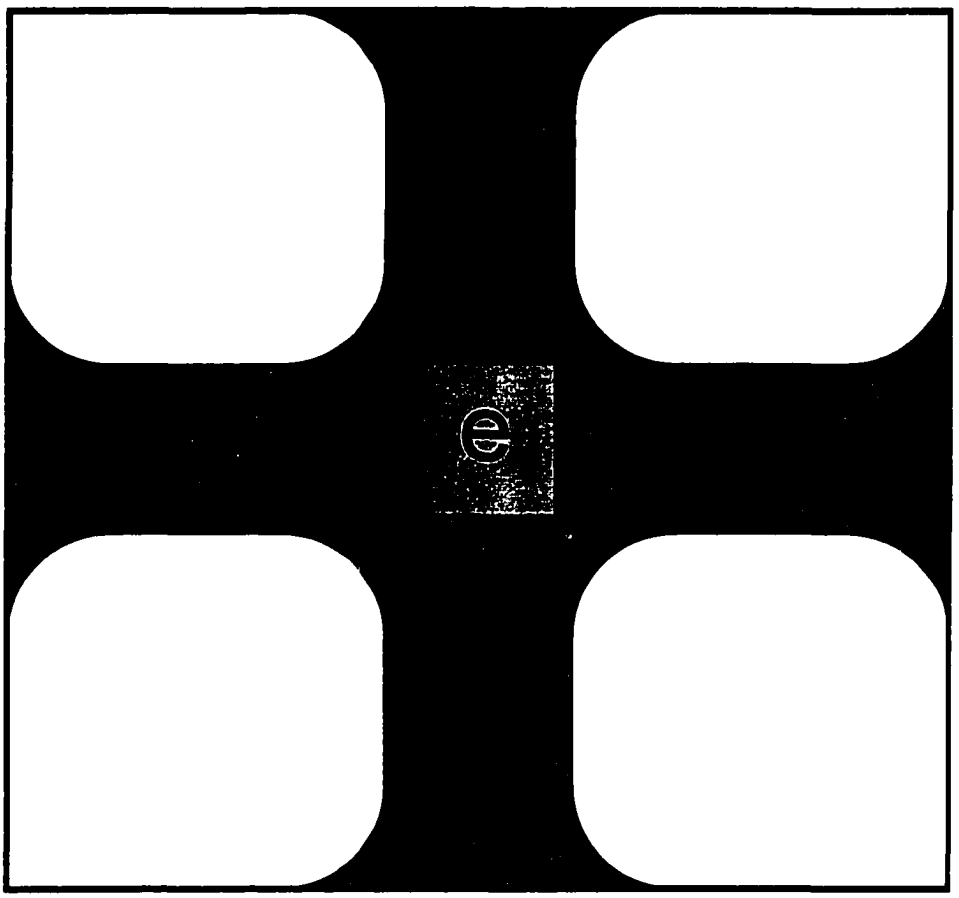

Figure 4. Schematic of a very large lattice, which percolates with an even 2NN-cluster both from left to right, and also up and down, as indicated by the grey area. The white area illustrates that, either no B-atoms remain on the odd sublattice, or else the odd 2NN-clusters have been divided into at least one piece, none of the pieces of which can possibly span the lattice, or percolate. The result is symmetry-breaking lattice.

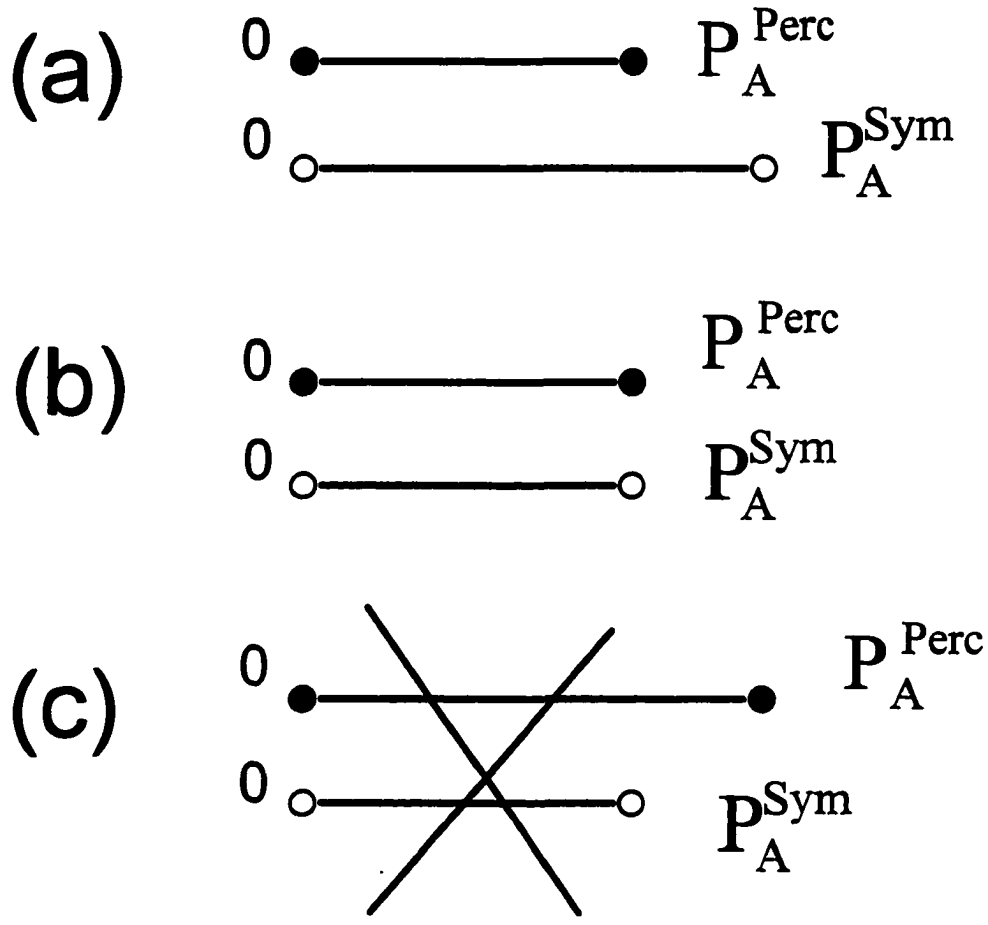

Figure 5. Both percolation and symmetry-breaking occur for a large lattice as $P_A \to 0^+$. If $[0, P_A^P]$ and $[0, P_A^S]$ represent the intervals on which percolation and symmetry-breaking occur, respectively, then diagrams (a)–(c) illustrate the three possible arrangements of this pair of intervals. Since percolation implies symmetry-breaking, the last arrangement (c) is impossible and has been struck out. The two remaining possibilities lead us to conclude that $P_A^P \leq P_A^S$.

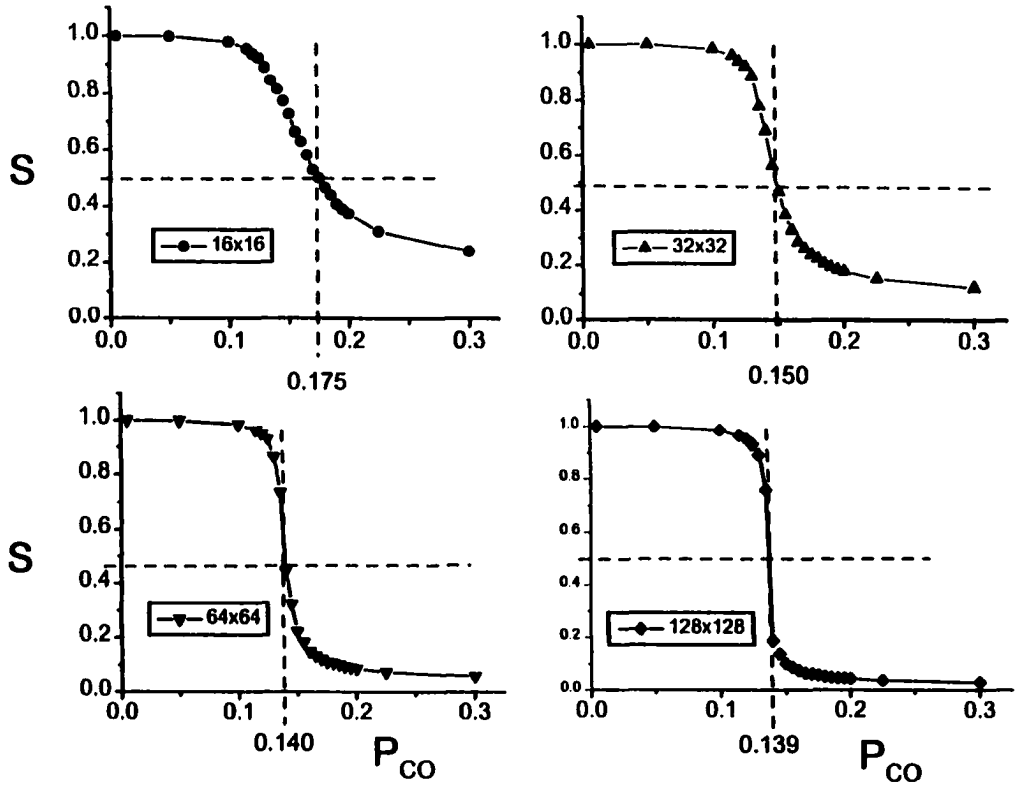

Figure 6. Plot of S versus P_A (=P_{CO}) for lattice of size (a) 16×16, (b) 32×32, (c) 64×64, and (d) 128×128. For a general square lattice with side of length L, the shape of the S-plot is similar to that of a step-function, with a "jump" at a value $P_A^{Sym}(L)$, depending on L. The value of S is close to one to the left of $P_A^{Sym}(L)$, and close to zero to the right. Note that as L increases, the "jump" becomes steeper and more well-defined. While the S-plots provide a helpful insight into the symmetry-breaking problem, still the location of the critical symmetry-breaking point, $P_A^{Sym}(L)$, for any given lattice is open to interpretation. Here, we indicate one of our tactics, namely the quantity of P_A where S = 0.5.

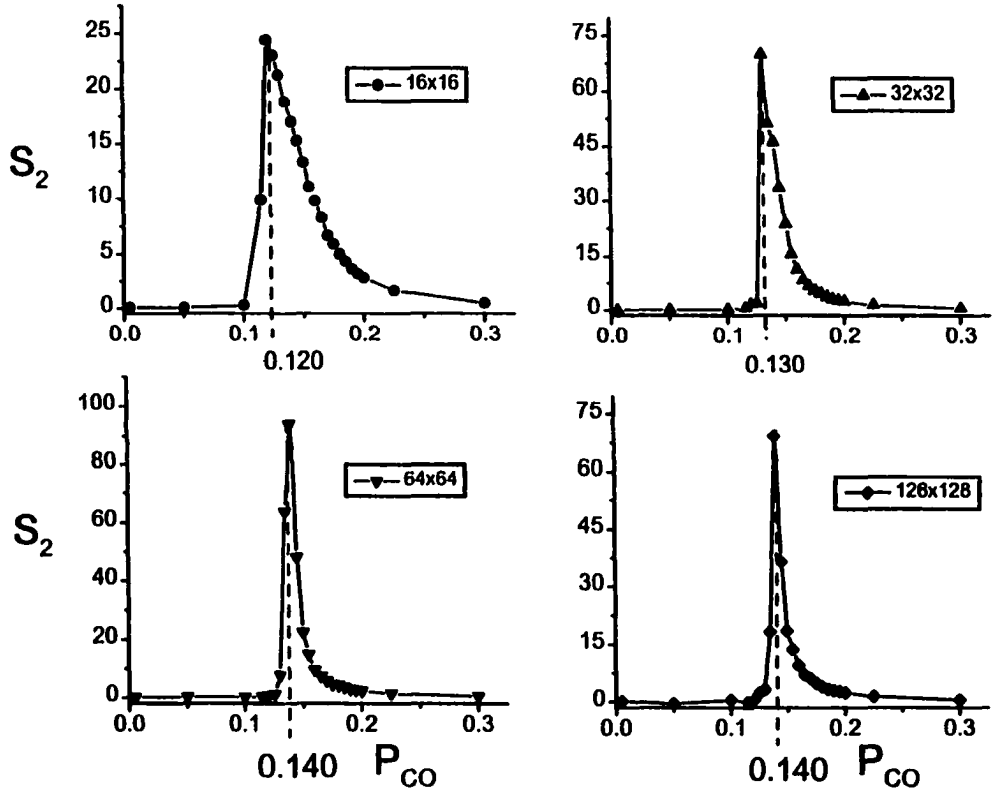

Figure 7. Plot of S_2 versus P_A (= P_{CO}) for lattice of size (a) 16×16, (b) 32×32, (c) 64×64, and (d) 128×128. The S_2-plot has the advantage over the S-plot, in that it provides a relatively smooth graph with a sharp peak occurring at a point $P_A^{Sym3}(L)$. Note how the peak becomes higher and sharper, as L increases. The unfortunate disadvantage, which does not manifest itself in the S-plots, is that as $P_A \rightarrow P_A^{Sym3}(L)$, the correlation time of the fluctuations increases. Thus, near the critical point, it is necessary to run the simulations for very long times, in order to obtain statistics good enough to provide a smooth graph with a well-defined sharp peak. Thus, narrowing down the accuracy of $P_A^{Sym3}(L)$ is quite a challenge.

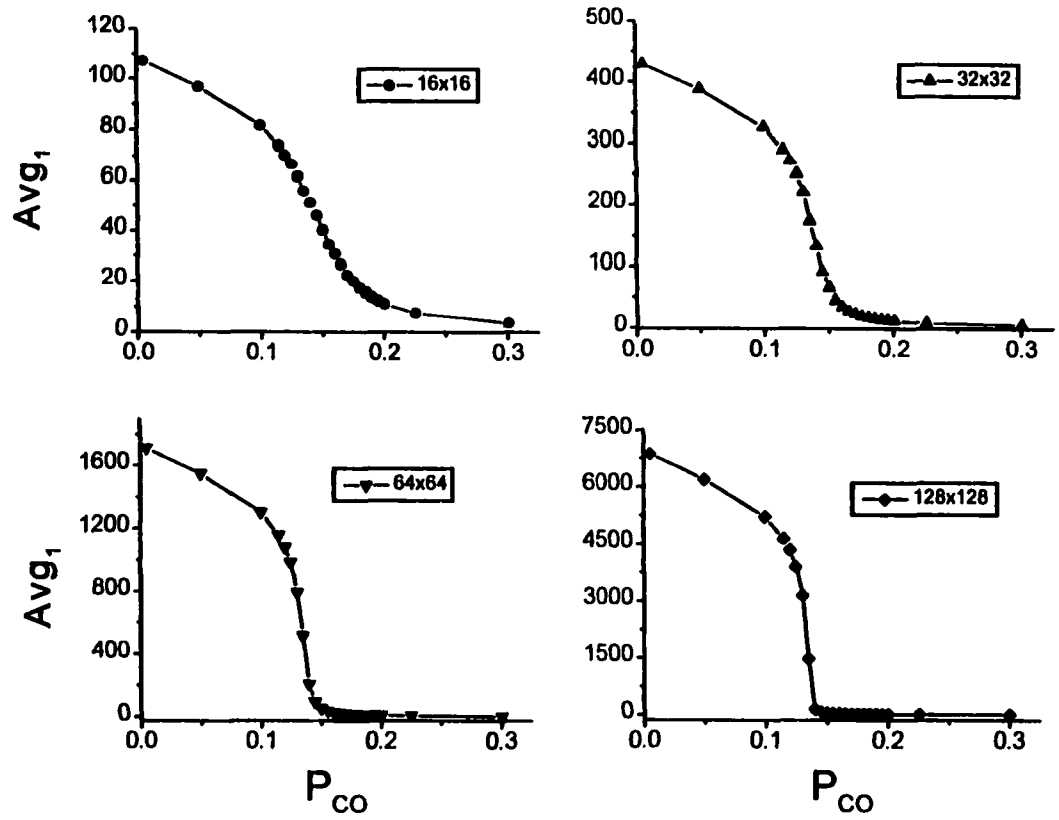

Figure 8. Plot of Avg_l versus P_A (= P_{CO}) for lattice of size (a) 16×16, (b) 32×32, (c) 64×64, and (d) 128×128. The quantity, Avg_l (= 2NN-cluster size including largest cluster) is a monotone decreasing function, and so for the same reason as with the S-plots, it is not clear how to choose the location of the critical percolation point. Note how, as L increases, the graphs develop a sharper L-shaped turn, suggesting a possible method of locating the percolation point, provided the lattices are large enough.

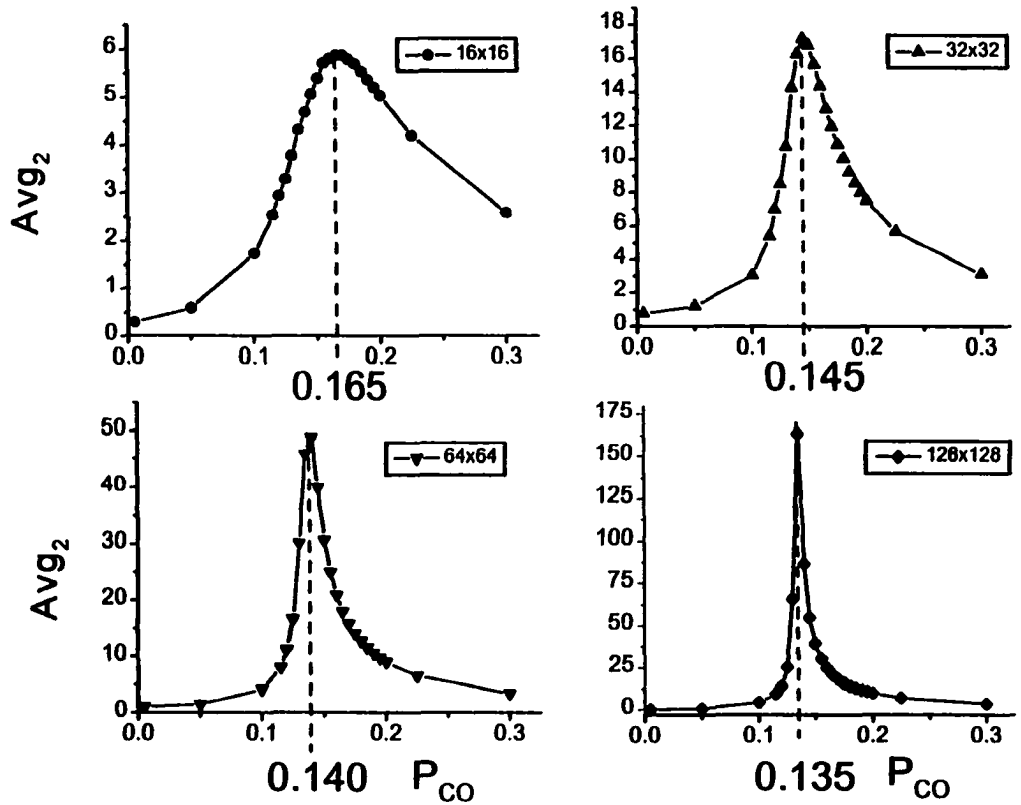

Figure 9. Plot of Avg_2 versus P_A (= P_{CO}) for lattice of size (a) 16x16, (b) 32x32, (c) 64x64, and (d) 128x128. The quantity, Avg_2 = 2NN-cluster size excluding largest cluster) is a smooth and nicely peaked graph, with a maximum at P_A^{Perc} , which is easily located. Note how the peak becomes higher and sharper, as L increases. Unlike the S_2-plots, the Avg_2-plots do not suffer unfortunate disadvantage of the simulations needing to run for very long times, as P_A nears the critical point.

$[B_-] = 0$). On the other hand, even though the natural steady-state for higher P_A consists of relatively high [A] and low [B] concentrations, the system does not take very long to break down an initially perfect checkerboard configuration of B-atoms, and subsequently to evolve into its preferred steady-state. Consequently, almost all of the plots in figures 6–9 were obtained by setting the initial lattice configuration to a perfect checkerboard of B-atoms.

What follows is a discussion of the behavior of each of the four quantities, S, S_2, Avg_1, and Avg_2, in turn. We find the estimates of the symmetry-breaking or percolation point for each quantity and system size, and describe two methods for extrapolating this data to an infinite system size. The first method employs a best-fit line technique, while the second is a method called finite-size scaling.

3.2.1 ORDER PARAMETER ANALYSIS

Firstly, we analyze the S-plots in figure 6. For a large square lattice with side of length L, the shape of the S-plot is similar to that of a step-function, with a "jump" at a value $P_A^{Sym}(L)$, depending on L. The value of S is close to one to the left of $P_A^{Sym}(L)$, and close to zero to the right. Again, we note that as L increases, the "jump" becomes steeper and more well-defined.

While the S-plots provide a helpful insight into the symmetry-breaking problem, still the best estimate of the critical symmetry-breaking point, $P_A^{Sym}(L)$, for any finite lattice size is open to interpretation. For a given L, there are several ways to choose $P_A^{Sym}(L)$, and it is not clear which method ought to yield the best answer. We have tried two tactics: (1) we chose $P_A^{Sym1}(L)$ as the value of P_A at the steepest slope, and (2) we chose $P_A^{Sym2}(L)$ as the

value of P_A where $S = 0.5$. We summarize these values in the first and second columns of table 2, respectively.

We extrapolate the value of the symmetry-breaking point, $P_A^{Sym1}(\infty)$, for an infinite lattice by plotting $P_A^{Sym1}(L)$ versus $1/L$. Using a best-fit line technique, our extrapolated value is $P_A^{Sym1}(\infty) \cong 0.1353$, (see figure 10(a)). This corresponds to a B-atom concentration of $[B] \cong 0.2989$. For $P_A^{Sym2}(\infty)$, we found a more linear trend by plotting $P_A^{Sym2}(L)$ versus $1/L^2$. We computed this extrapolated value, $P_A^{Sym2}(\infty) \cong 0.1379$ (see figure 10(b)). This corresponds to a B-atom concentration of $[B] \cong 0.3104$.

3.2.2 FLUCTUATION PARAMETER ANALYSIS

Our second quantity, the B-atom fluctuation parameter S_2, has the advantage over the symmetry-breaking parameter S, in that it provides a relatively smooth graph with a sharp

Table 2. Four critical points for various lattices of side length, L. The points P_A where: (1) the S-plot attains its steepest slope; (2) $S = 0.5$; (3) the S_2-plot attains its maximum; and (4) the Avg_2–plot attains its maximum are denoted by $P_A^{Sym1}(L)$, $P_A^{Sym2}(L)$, $P_A^{Sym3}(L)$, and $P_A^{Perc}(L)$, respectively.

L	$P_A^{Sym1}(L)$ (steepest slope)	$P_A^{Sym2}(L)$ (S = 0.5)	$P_A^{Sym3}(L)$	$P_A^{Perc}(L)$
16	0.155	0.175	0.120	0.165
32	0.145	0.148	0.130	0.145
64	0.140	0.140	0.140	0.140
128	0.138	0.138	0.140	0.135

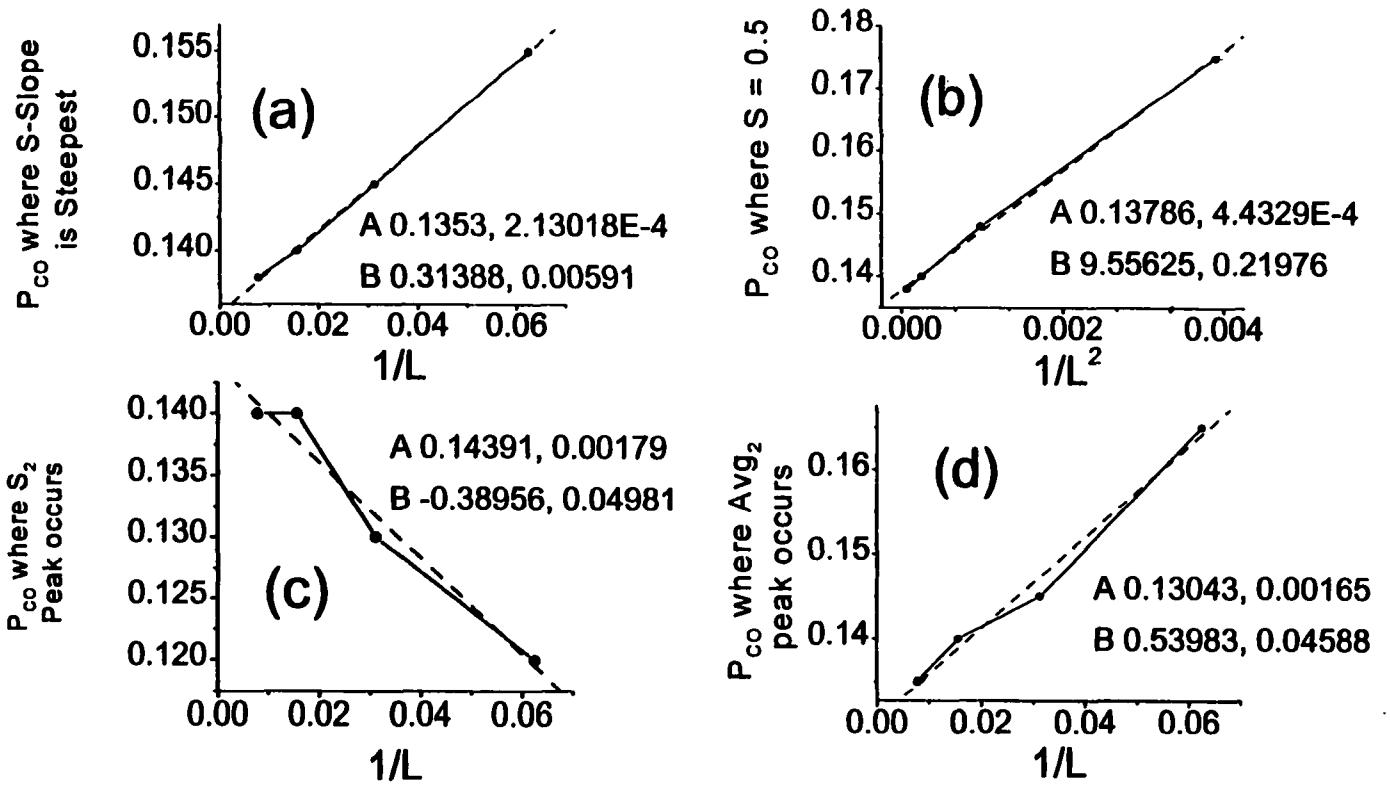

Figure 10. We extrapolate the value of (a)–(c): the symmetry-breaking point, and (d): the percolation point for an infinite lattice, using a best-fit line technique. In graphs (a), (c), and (d) we plot the quantities P_A^{Sym1}, P_A^{Sym3}, and P_A^{Perc}, respectively, versus 1/L, while, in graph (b) we plot the quantity P_A^{Sym2} versus $1/L^2$. The extrapolated values are: (a) $P_A^{Sym1}(\infty) \cong 0.1353$, (b) $P_A^{Sym2}(\infty) \cong 0.1379$, (c) $P_A^{Sym3}(\infty) \cong 0.1439$, and (d) $P_A^{Perc}(\infty) \cong 0.1304$. This data is summarized in the "best-fit line extrapolation" column of table 3.

peak occurring at a point $P_A^{Sym3}(L)$, providing an estimate of $P_A^{Sym}(L)$. (This is not exactly the same as the numbers $P_A^{Sym1}(L)$ and $P_A^{Sym2}(L)$, provided by the S-plots.) See figure 7 for these S_2-plots. We summarize these peak values in the third column of table 2, and in the same way as with the S-plots, we extrapolated the critical point, $P_A^{Sym3}(\infty)$, for an infinite lattice (see figure 10(c)). Our result is $P_A^{Sym3}(\infty) \cong 0.1439$, which corresponds to a B-atom concentration of $[B] \cong 0.2731$. Unfortunately, this is not in very good agreement with the values obtained using the S- and S_2-plot. Nor does it agree with the results of the more sophisticated finite-size scaling method, which we describe later.

Using the S_2–parameter, no guesswork is needed to determine the point of interest, $P_A^{Sym3}(L)$, due to the peaked nature of the S_2-plots. There is, unfortunately, a disadvantage. One might suppose that to pinpoint $P_A^{Sym3}(L)$ with more precision, we should need only to collect data on a finer subdivision of the interval containing $P_A^{Sym3}(L)$. However, as $P_A \rightarrow P_A^{Sym3}(L)$, the correlation time of the fluctuations increases. Thus, near the critical point, it is necessary to run the simulations for very long times, in order to obtain statistics good enough to provide a smooth graph with a well-defined sharp peak. This problem does not manifest itself in the S-plots.

3.2.3 DOMAIN SIZE ANALYSIS

The above mentioned problem with long correlation times does not arise while plotting our third and fourth quantities of interest, namely, the 2NN-cluster size, both

including and not including the largest cluster. In figures 8–9, we plotted both Avg_1 and Avg_2, as defined in eq. 22 and eq. 23. The former quantity, Avg_1, is a monotone decreasing function, and so for the same reason as with the S-plots, it is not clear how to choose the location of the critical percolation point. On the other hand, the latter quantity, Avg_2, provides a smooth and nicely peaked graph, with a maximum at $P_A^{Perc}(L)$, which is easily and unambiguously located. Thus, in the same way as in the S_2-plots, we extrapolated the critical point, $P_A^{Perc}(\infty) \cong 0.1304$, which corresponds to B-atom coverage of $[B] \cong 0.3104$. This suggests that $P_A^{Perc}(\infty)$ is slightly below $P_A^{Sym}(\infty)$ (see also below).

3.2.4 FINITE SIZE SCALING

One might wonder if the difference between the extrapolated values for the percolation point, P_A^{Perc}, and the symmetry-breaking point, P_A^{Sym} (as summarized in the "best-fit line" column of table 3) might be explained by statistical uncertainty or inadequacies in our extrapolation procedure. From section 3.1, we already know that $P_A^{Perc} \leq P_A^{Sym}$, but is it really true that $P_A^{Perc} < P_A^{Sym}$? In an attempt to improve our results, we extrapolated the values of P_A^{Perc} and P_A^{Sym} for an infinite lattice by using a different method, namely, finite-size scaling.

The finite-size scaling method requires consideration of behavior for a sequence of lattice sizes, selected in a systematic way. In fact, we have chosen our lattices to have side length $L = 2^i$, for at least four consecutive integers, i. Then, in order to obtain the finite-size

Table 3. We use two methods to extrapolate the symmetry-breaking and percolation points in an infinite lattice. The first method employs a best-fit line technique, while the second is a method called finite-size scaling. The results of both methods, summarized here, lead us to conclude that, not only is $P_A^P \leq P_A^S$, but it is highly likely that this inequality is a strict one.

Critical value for infinite lattice		best-fit line	finite-size scaling
Symmetry-Breaking P_A^{Sym}	$P_A^{Sym1}(\infty)$	0.1353 ± 0.0003	0.1360 ± 0.0010
	$P_A^{Sym2}(\infty)$	0.1379 ± 0.0005	
	$P_A^{Sym3}(\infty)$	0.1439 ± 0.0020	
Percolation P_A^{Perc}	$P_A^{Perc}(\infty)$	0.1304 ± 0.0020	0.1315 ± 0.0015

scaling plots, we graph the ratios of plots of the quantity in question. For example, we first label S for the lattice of side length 2^i, by $S_{2^i} = S_{2^i}(P_A)$. For instance, for the 16×16 lattice, the value of the S at $P_A = 0.10$ is written $S_{16}(0.10)$. Next, for each value P_A, we define $R_i(P_A)$ to be the ratio:

$$R_i(P_A) = \frac{S_{2^{i+1}}(P_A)}{S_{2^i}(P_A)}. \qquad \text{eq. 24}$$

Finally, we plot the $R_i(P_A)$ versus P_A for i = 3, 4, 5,and 6, all on the same graph, and use their "common" point of intersection to estimate the value of the critical point (either

symmetry-breaking or percolation point). The justification for this procedure is based on rather universal finite-size scaling properties of quantities which diverge at continuous transitons.

We show these R_i–plots in figure 11(a). The plots all meet at a value of $P_A^{Sym} \cong 0.1360$, with an error of about ± 0.0010. In a similar manner, the graph in figure 11(b) was obtained by plotting the ratios of the cluster sizes shown in figure 9. The point of intersection, in this case, gives an estimate of $P_A^{Perc} \cong 0.1315$, with an error of about ± 0.0015. These finite-size scaling results are summarized in the "finite-size scaling" column of table 3. From table 3, we see that the finite-size scaling method is in fairly good agreement with the best-fit line extrapolation, both for the symmetry-breaking point and for the percolation point, with a bigger error-bar in the latter case. Either method leads us to conclude that, not only is $P_A^{Perc} \leq P_A^{Sym}$, but it is highly likely that this inequality is a strict one.

3.3 APPROXIMATE ANALYTIC TREATMENT

Our next goal is to use an approximate analytic treatment to obtain an estimate for the symmetry-breaking point P_A^{Sym} from the rate equations given in eq. 15 (of sec.2.3). In order to close this system of equations, we need a reasonable approximation for the eight-site configuration probabilities appearing on the RHS of each of eq. 15(b) and (c) in terms of the adspecies coverages. As in Paper I, we invoke the standard pair- or Kirkwood-type approximation, based on decomposition of the multi-site configurations into constituent pairs. Thus,

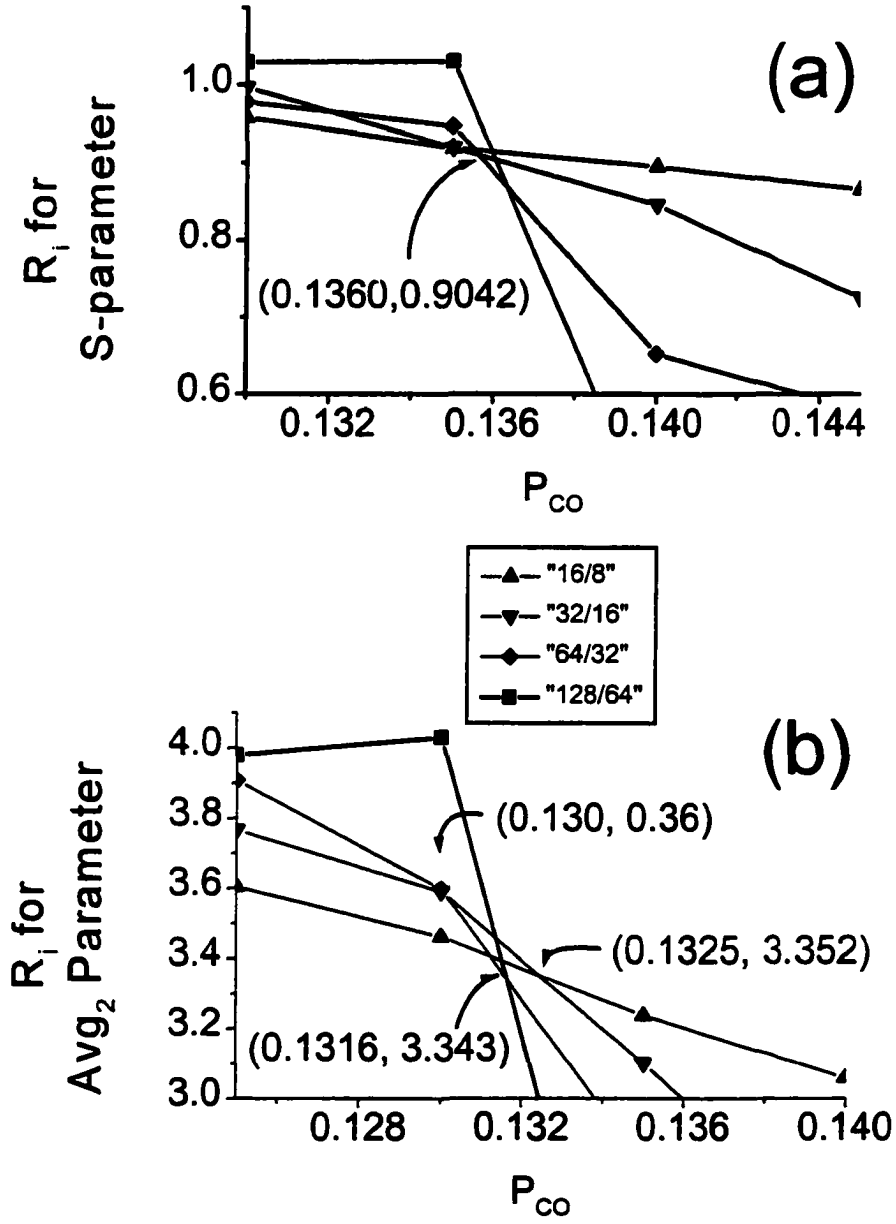

Figure 11. We have plotted the graphs of R_i for (a) the symmetry-breaking parameter, S; and (b) the 2NN cluster size; for i = 8, 16, 32, and 64. The values of the symmetry-breaking and percolation points are approximated using the points of intersection: $P_A^S \cong 0.1360 \pm 0.0010$, and $P_A^P \cong 0.1315 \pm 0.0015$, respectively. This data is summarized in "finite-size scaling" column of table 3.

the eight-site configuration in eq. 15(b) becomes:

$$\begin{bmatrix} & Z_+ & \\ Z_+ & Z_- & Z_+ \\ & Z_+ & \end{bmatrix} \approx \frac{[Z_+Z_-]^8}{[Z_+]^2[Z_-]^6} = \frac{(1-[B_+]-[B_-])^8}{(1-[B_+])^2(1-[B_-])^6} \quad , \qquad \text{eq. 25}$$

where the equality in eq. 25 is found by employing eq. 1(c) and eq. 7. A similar expression holds for the eight-site configuration in eq. 15(c). Using eq. 1(a,c), eq. 4, and the pair approximations suggested in eq. 25, we have that eq. 15 reduces to the following closed set of three rate equations, in terms of only the three adspecies coverages [A], [B_], and [B_+]:

$$\frac{d}{dt}[A] = P_A\left(1-[A]-\frac{[B_+]}{2}-\frac{[B_-]}{2}\right) - d[A] - 4k[A]\frac{\left(\frac{[B_+]}{2}+\frac{[B_-]}{2}\right)}{1-\frac{[B_+]}{2}-\frac{[B_-]}{2}} \qquad \text{eq. 26(a)}$$

$$\frac{d}{dt}[B_-] = 2P_B\left(\frac{1-[A]-\frac{[B_+]}{2}-\frac{[B_-]}{2}}{1-\frac{[B_+]}{2}-\frac{[B_-]}{2}}\right)^2 \frac{(1-[B_+]-[B_-])^8}{(1-[B_-])^6(1-[B_+])^2} - 4k[A]\frac{[B_-]}{1-\frac{[B_+]}{2}-\frac{[B_-]}{2}} \qquad \text{eq. 26(b)}$$

$$\frac{d}{dt}[B_+] = 2P_B\left(\frac{1-[A]-\frac{[B_+]}{2}-\frac{[B_-]}{2}}{1-\frac{[B_+]}{2}-\frac{[B_-]}{2}}\right)^2 \frac{(1-[B_+]-[B_-])^8}{(1-[B_+])^6(1-[B_-])^2} - 4k[A]\frac{[B_+]}{1-\frac{[B_+]}{2}-\frac{[B_-]}{2}} \qquad \text{eq. 26(c)}$$

We used Mathematica to find the steady-state solution of [A] and [B], in the case when d = 0. This steady-state solution can be found by setting each of the equations in eq. 26 equal to zero, and solving the system of equations for the three unknowns [A], [B_], and [B+]. However, some preliminary rearrangement helps to greatly simplify the analysis.

First, we set eq. 26(a) equal to zero and solved for [A] in terms of [B+] and [B_]. For the case d = 0, we get:

$$[A]=\frac{P_A\left(1-\frac{[B_+]}{2}-\frac{[B_-]}{2}\right)^2}{P_A\left(1-\frac{[B_+]}{2}-\frac{[B_-]}{2}\right)+4k\left(\frac{[B_+]}{2}+\frac{[B_-]}{2}\right)}. \qquad \text{eq. 27}$$

We note that, since the coverage [A] is independent of whether or not the lattice is spatially uniform and rotationally invariant, eq. 27 could also have been obtained by plugging eq. 4 into eq. 12, and setting d = 0. Next, we recall from section 1 that $P_B = 1 - P_A$, and plug eq. 27 into eq. 26(b) and (c), and after some algebraic simplifications, we obtain the following two equations in the two unknowns [B+] and [B_]:

$$0 = 8k(1-P_A)(1-[B_+]-[B_-])^8\left(\frac{[B_+]}{2}+\frac{[B_-]}{2}\right)^2$$
$$-[B_-]P_A\left(1-\frac{[B_+]}{2}-\frac{[B_-]}{2}\right)(1-[B_-])^6(1-[B_+])^2\left\{P_A\left(1-\frac{[B_+]}{2}-\frac{[B_-]}{2}\right)+4k\left(\frac{[B_+]}{2}+\frac{[B_-]}{2}\right)\right\} \qquad \text{eq. 28(a)}$$

$$0 = 8k(1-P_A)(1-[B_+]-[B_-])^8\left(\frac{[B_+]}{2}+\frac{[B_-]}{2}\right)^2$$
$$-[B_+]P_A\left(1-\frac{[B_+]}{2}-\frac{[B_-]}{2}\right)(1-[B_+])^6(1-[B_-])^2\left\{P_A\left(1-\frac{[B_+]}{2}-\frac{[B_-]}{2}\right)+4k\left(\frac{[B_+]}{2}+\frac{[B_-]}{2}\right)\right\} \quad \text{eq. 28(b)}$$

A much more simplified fifth-degree polynomial relating the two variables $[B_+]$ and $[B_-]$ results from subtracting the former equation from the latter:

$$[B_+](1-[B_+])^4 - [B_-](1-[B_-])^4 = 0 \quad \text{eq. 29}$$

Thus, there are five solutions of $[B_-]$ in terms of $[B_+]$, only two of which are physically possible; that is, $0 \le [B_-], [B_+] \le 1$. Of the three nonphysical solutions, one is real, but $[B_-] \ge 1$, and the remaining two solutions are complex. Of the two physically possible solutions, one is the symmetric solution $[B_-] = [B_+]$, as predicted in section 2.3. The remaining physically possible solution for $[B_-]$ in terms of $[B_+]$, is our new, symmetry-breaking solution, which we plugged into eq. 28(b) to solve for P_A. There are two possible solutions for P_A, only one of which is positive and, thus, physically possible.

We show the graphs of both the old non-symmetry-breaking solution and the new symmetry-breaking result in figure 12(a). We, further, performed a standard linear stability analysis to determine the stability of the solutions, also indicated in the figure 12(a). The result is a stable symmetry-breaking solution and unstable symmetric $P_A < 0.1758$.

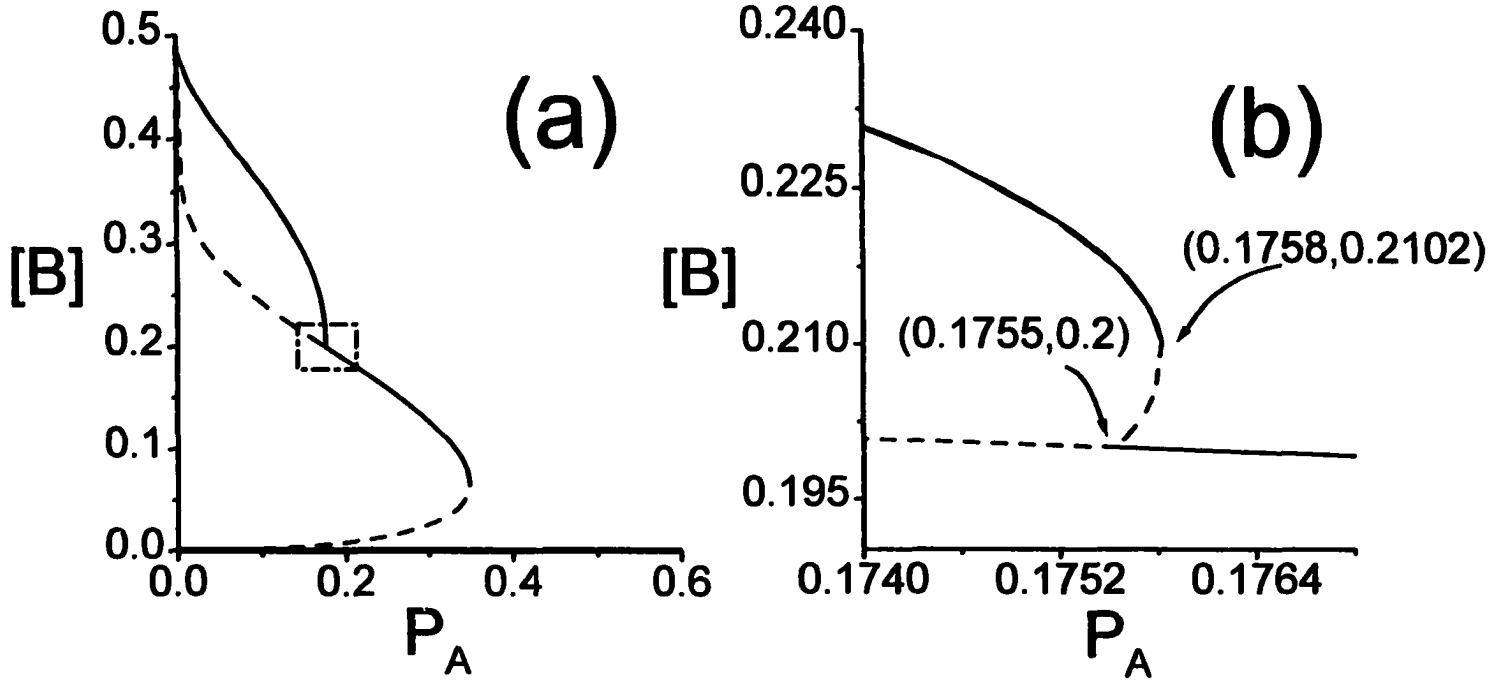

Figure 12. (a) Analytic solution of concentration [B] versus P_A. A solid curve indicates a stable solution while a dashed curve indicates an unstable one. The new, symmetry-breaking solution, which is a result of solving equations (1)–(3), rides "piggy-back" on the old non-symmetry-breaking solution obtained in Ref. [5], when it was assumed that $[B_+] = [B_-]$. (b) Surprisingly, the symmetry-breaking analytical solution is not entirely monotonic. Enlarging (a) for a small window of P_A values, $0.1755 \leq P_A \leq 0.1758$, we find the solution doubles back on itself, yielding four stable steady-state values for $[B_+]$ (or $[B_-]$) in this region and three unstable ones. Of the stable solutions, two occur on the upper solid curve, where $[B_+] \neq [B_-]$; one occurs on the lower solid curve, where $[B_+] = [B_-] \neq 0$, and the third is $[B_+] = [B_-] = 0$. For the unstable solutions, two occur on the dashed curve, where $[B_+] \neq [B_-]$, and the third is the old non-symmetry-breaking solution $[B_+] = [B_-]$, close to, but not equal to zero.

Surprisingly, the symmetry-breaking analytical solution is not entirely monotonic. For a small window of P_A values, $0.1755 \leq P_A \leq 0.1758$, we find the solution, doubles back on itself, yielding 4 stable steady-state values for $[B_+]$ (or $[B_-]$) in this region, as illustrated in figure 12(b). It is highly likely, however, that this phenomenon is an artifact of the pair approximations made in eq. 25, since such behavior does not occur in a simplified version for this reaction model, or in classic equilibrium models exhibiting symmetry-breaking. While quantitative disagreement with the simulation results is to be expected when making the necessary pair approximations to close the set of three relations given in eq. 15, we may still conclude that the analytical treatment, is able, qualitatively, to reproduce the symmetry-breaking behavior.

Finally, we present a direct analysis of the behavior of the symmetry-breaking solution for low P_A. Here, we let $[B_+] = 1 - \delta$, and $[B_-] = \varepsilon$, for some very small δ and ε. We plug these values into eq. 26(b) and (c), and try to determine the behavior of δ and ε in relation to P_A. Using the following substitutions

$$1-[B_+]-[B_-] \equiv \delta - \varepsilon \text{, and} \qquad \text{eq. 30(a)}$$

$$P_B \equiv 1, \qquad \text{eq. 30(b)}$$

In the steady-state, eq. 26(b), (c), and eq. 27 become:

$$0 \cong \frac{2(\delta-\varepsilon)^8}{\delta^2(1-\varepsilon)^6}\frac{\left(\frac{1}{2}(1-2[A]+\delta-\varepsilon)\right)^2}{\left(\frac{1}{2}(1+\delta-\varepsilon)\right)^2} - 4k[A]\frac{\varepsilon}{\frac{1}{2}(1+\delta-\varepsilon)}, \qquad \text{eq. 31(a)}$$

$$0 \cong \frac{2(\delta-\varepsilon)^8}{\delta^6(1-\varepsilon)^2}\frac{\left(\frac{1}{2}(1-2[A]+\delta-\varepsilon)\right)^2}{\left(\frac{1}{2}(1+\delta-\varepsilon)\right)^2} - 4k[A]\frac{1-\delta}{\frac{1}{2}(1+\delta-\varepsilon)}, \text{ and} \qquad \text{eq. 31(b)}$$

$$[A] \cong \frac{\frac{P_A}{4}(1+\delta-\varepsilon)^2}{\frac{P_A}{2}(1+\delta-\varepsilon)+\frac{4k}{2}(1-\delta+\varepsilon)} \cong \frac{\frac{P_A}{4}}{0+2k} \cong \frac{P_A}{8k}. \qquad \text{eq. 31(c)}$$

where P_A has been replaced by 0 in the denominator of eq. 31(c). Next, since δ, ε and [A] are very close to zero, we replace each of the following quantities in eq. 31 by 1: the ratio of the squares, $1 - \varepsilon$, $1 - \delta$ and $1 + \delta - \varepsilon$, and we get the following pair of approximations:

$$0 \cong \frac{2(\delta-\varepsilon)^8}{\delta^2} - 8k[A]\varepsilon = \frac{2(\delta-\varepsilon)^8}{\delta^6} - \frac{8k[A]\varepsilon}{\delta^4}, \text{ and} \qquad \text{eq. 32(a)}$$

$$0 \cong \frac{2(\delta-\varepsilon)^8}{\delta^6} - 8k[A]. \qquad \text{eq. 32(b)}$$

By setting eq. 32(a) and eq. 32(b) equal to each other, we have $\varepsilon \cong \delta^4$, and plugging this into eq. 32(b), we get:

$$8k[A] \cong \frac{2(\delta - \delta^4)^8}{\delta^6} \cong 2\delta^2. \qquad \text{eq. 33}$$

Finally, using eq. 31(c) and eq. 33, we find:

$$\delta \cong \sqrt{\frac{P_A}{2}}, \qquad \text{so that} \qquad \varepsilon \cong \delta^4 \cong \frac{P_A^2}{4}. \qquad \text{eq. 34}$$

Therefore, for P_A very close to zero, the corresponding [B+] and [B–] behavior is by:

$$[B_+] \cong 1 - \sqrt{\frac{P_A}{2}}, \qquad \text{and} \qquad [B_-] \cong \frac{P_A^2}{4}, \qquad \text{eq. 35}$$

as can be seen in figure 13.

4. CRITICAL BEHAVIOR AT THE CUSP BIFURCATION POINT

4.1 BASIC CONCEPTS & DEFINITIONS

As noted in section 2.4, an interesting phenomenon which does not evidence itself in the steady-state phase diagrams (figure 3), is the high amplitude of fluctuations in the concentrations θ_A and θ_B as near the cusp bifurcation.

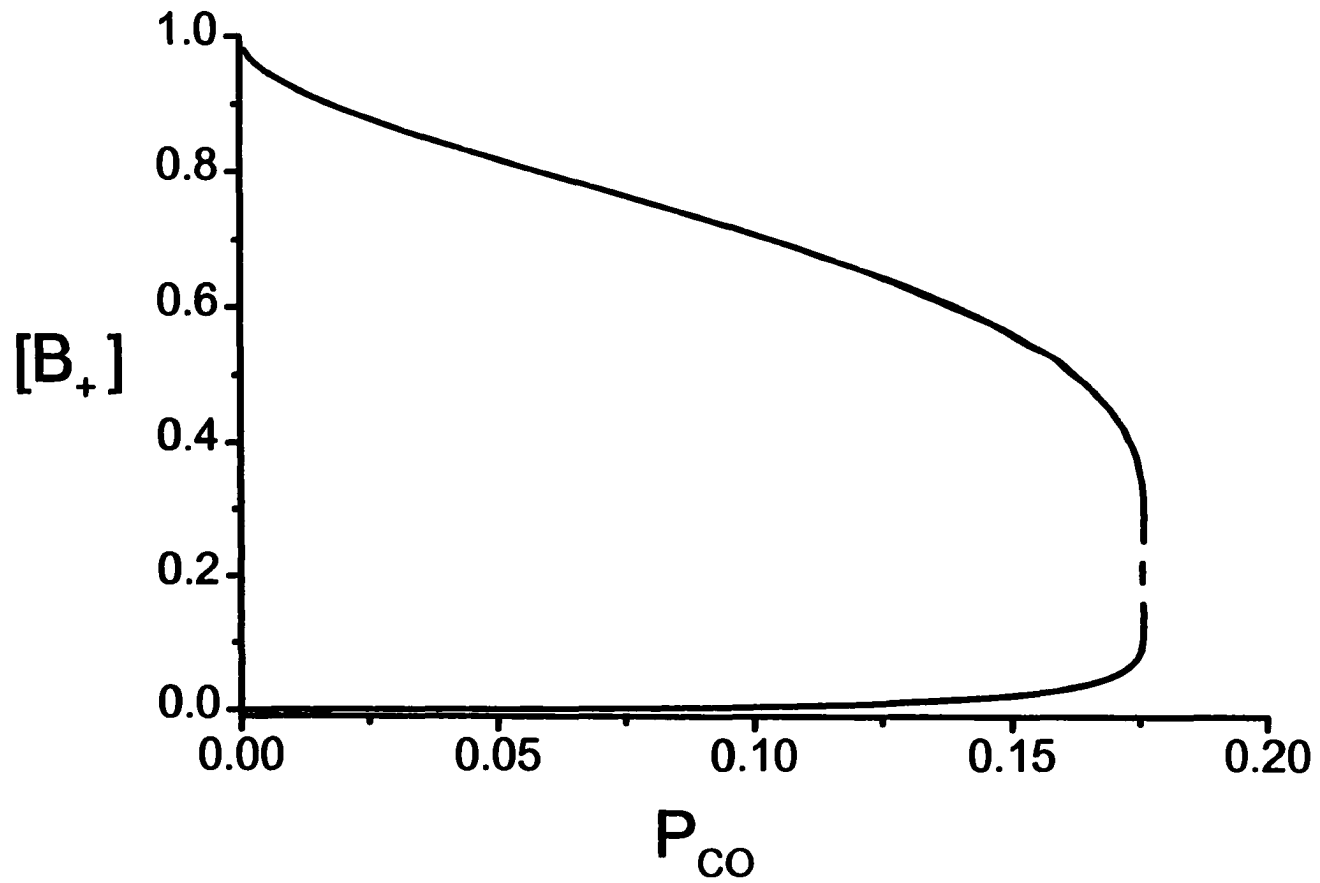

Figure 13. Plot of analytic solution for $[B_+]$ and $[B_-]$, using pair-approximation, in the symmetry-breaking case. For a given P_A, the graph yields two values. If the higher value gives $[B_+]$, then the lower value gives $[B_-]$, and vise versa. A direct analysis of the behavior of the symmetry-breaking solution, for low P_A, yields: $[B_+] \cong 1 - \sqrt{(P_A/2)}$, while $[B_-] \cong P_A^2/4$.

If we observe, say, the concentration θ_A over time, t, using our standard simulation code, we see that the average of θ_A settles to a steady-state value $[A]_S$. At any given time, however, θ_A is not necessarily equal to $[A]_S$. Rather, θ_A fluctuates about $[A]_S$, as indicated in figure 14. Three questions, which arise naturally, are: (1) "what is the amplitude of the fluctuations?" (2) "what is the spatial correlation of the adspecies?" and (3) "how long is a fluctuation 'cycle' "? We consider the same questions for the θ_B–fluctuations. The answers depend on the system parameters.

The first quantities we wish to study are: the average amplitude of the concentration fluctuations given by $\left\langle \left(\theta_J - \langle\theta_J\rangle\right)^2 \right\rangle$, with J = A or B; the anticorrelation data $\left\langle \left(\theta_A - \langle\theta_A\rangle\right)\left(\theta_B - \langle\theta_B\rangle\right) \right\rangle$; and the spatial correlation, $C_{JJ'}(\underline{\ell} - \underline{\ell}')$, between two adspecies J and J′ (not necessarily the same), located at the lattice sites $\underline{\ell}$ and $\underline{\ell}'$, respectively, for a translation-invariant system. This last quantity, which we discuss in detail in Appendix A, is related to the fluctuations by the following general formula:

$$\left\langle \left(\theta_J - \langle\theta_J\rangle\right)\left(\theta_{J'} - \langle\theta_{J'}\rangle\right) \right\rangle = \frac{1}{N}\sum_{\underline{\ell}} C_{JJ'}(\underline{\ell}) \; . \qquad \text{eq. 36}$$

Therefore, the fluctuations of the concentration θ_J about its steady-state value are approximately proportional to the spatial correlations and inversely proportional to the system size.

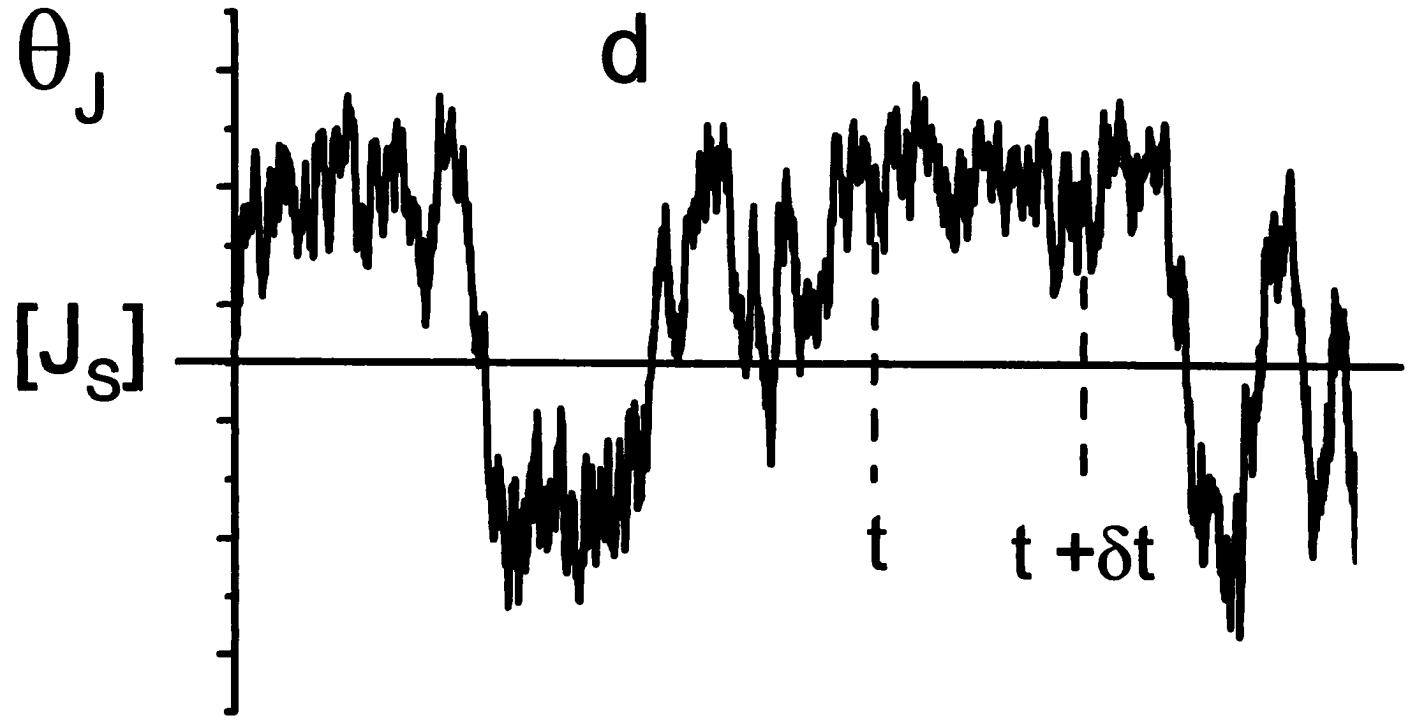

Figure 14. Three key features of θ_J-fluctuations over time, t: (1) the steady-state value $[J]_S$, (2) the fluctuation amplitude, and (3) the length of the fluctuation 'cycle'. It is also natural to ask, "what is the spatial correlation of the adspecies?" It turns out there is a relation between the spatial correlation and the fluctuation amplitude.

Finally, our last quantity of interest is the time auto-correlation function and the associated correlation time. Denoting the instantaneous J-particle concentration at time, t, by $\theta_J(t)$, we determine the average correlation between the fluctuation amplitudes at two times, δt apart, as follows:

$$C(\delta t) = \frac{\left\langle (\theta_J(t) - \langle \theta_J \rangle)(\theta_J(t+\delta t) - \langle \theta_J \rangle) \right\rangle}{\left\langle (\theta_J(t) - \langle \theta_J \rangle)^2 \right\rangle}. \qquad \text{eq. 37}$$

We define the correlation time, T_{corr}, as the value of δt at which $C(\delta t)$ has dropped (from its value of unity for $\delta t = 0$) down to 0.5.

4.2 SIMULATION RESULTS FOR COVERAGE FLUCTUATIONS

To study the fluctuation amplitudes and time correlations, we consider a range of d-values $0 \leq d < 0.053$, for which we know there is a region of bistability for [A] (also for [B]). We fix d and run the simulation for the corresponding midpoint of the bistability range, P_A^{MidPt}, as indicated in figure 15, until a steady-state is "reached".

4.2.1 FLUCTUATION AMPLITUDE

A series of θ_A-fluctuation and θ_B-fluctuation plots is shown in figure 16, for selected values of d, for a 150×150 lattice, with simulations begun initially in the inactive branch. Two features, which immediately call attention to themselves, are the amplitude of the fluctuations, which increases as $d \rightarrow d_c$, and the anti-correlation θ_A- and θ_B-fluctuations.

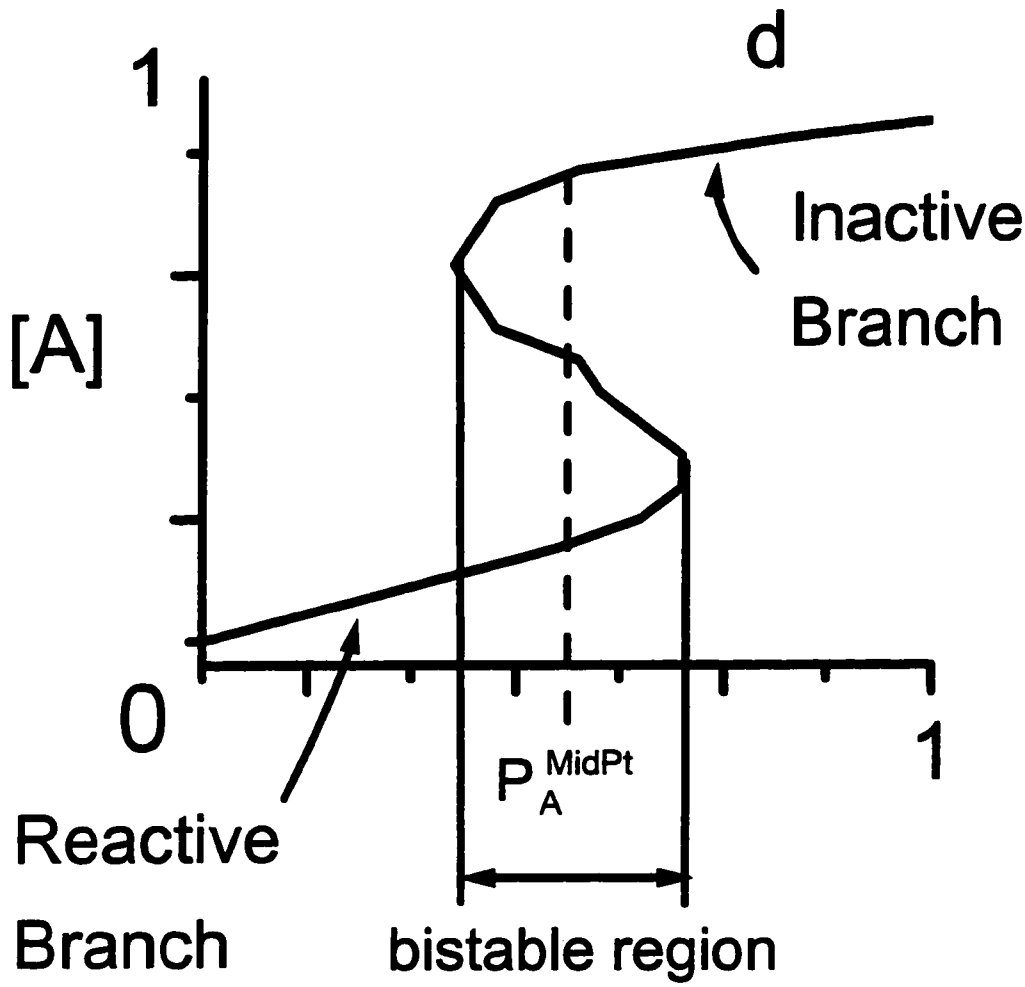

Figure 15. To study the fluctuation amplitudes and time correlations, we consider a range of d-values $0 \leq d < 0.053$, for which we know there is a region of bistability for [A] (also for [B]). We fix d and run the simulation for the corresponding midpoint of the bistability range, P_A^{MidPt}, as indicated here, until a steady-state is "reached".

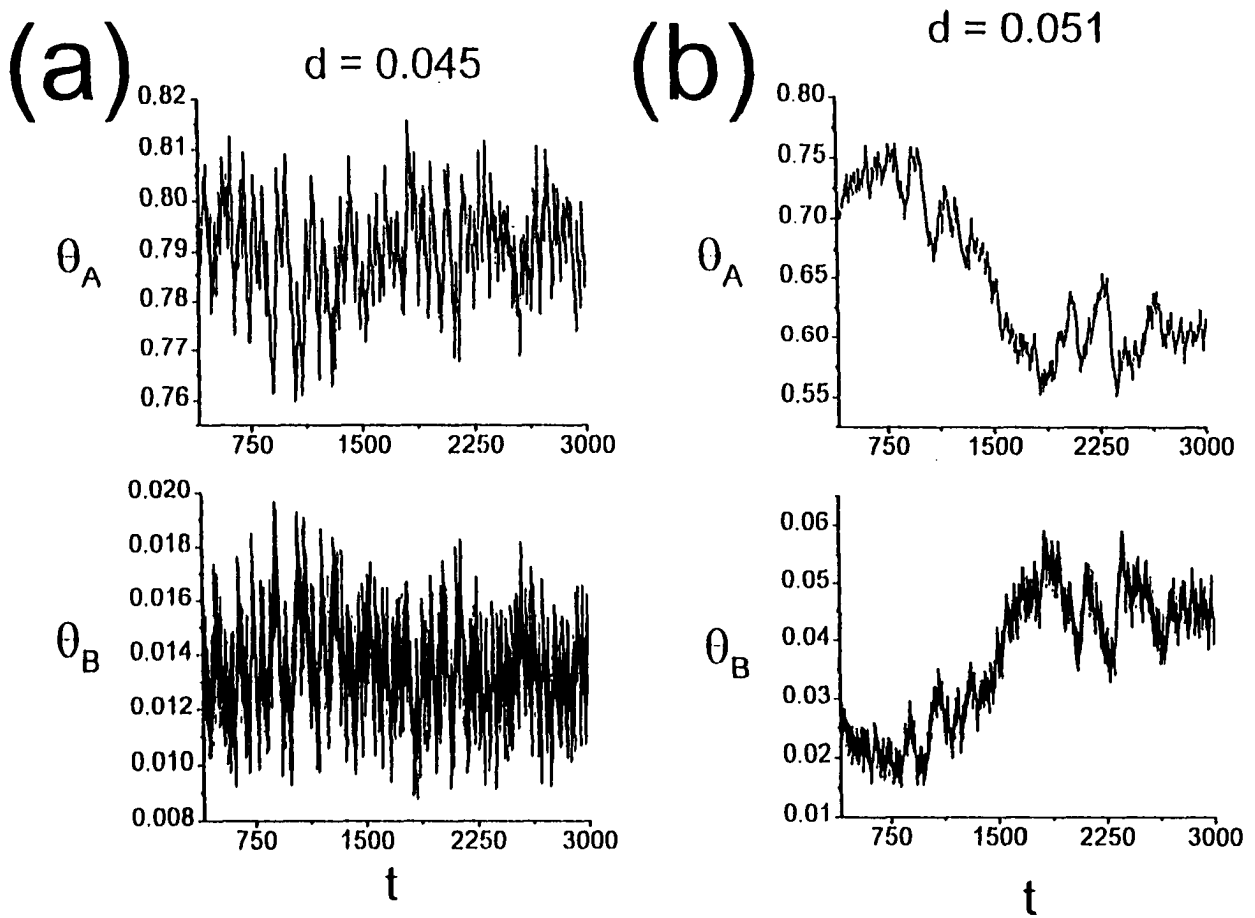

Figure 16. A series of θ_A-fluctuation and θ_B-fluctuation plots, for selected values of d, for 150×150 lattice, with simulations begun initially in the inactive branch. Two features, which immediately call attention to themselves, are the amplitude of the fluctuations, which increases as $d \rightarrow d_c$, and the anti-correlation θ_A- and θ_B-fluctuations.

The amplitudes of the θ_A-fluctuations for the inactive branch are smaller than for the reactive branch. A plot of the θ_B-fluctuations versus d looks similar. For a fixed d, we fix J = J′ = A, in eq. 36 and obtain:

$$\left\langle \left(\theta_A - \langle\theta_A\rangle\right)^2 \right\rangle = \frac{K_{d,N}}{N} , \qquad \text{eq. 38}$$

where $K_{d,n}$ depends on d and weakly depends on the system size N. Thus, in figure 17, we plot $K_{d,n}$, which increases as d increases toward d_c. A similar expression holds for the [B] fluctuations. These fluctuation amplitudes and the anti-correlation data, $\left(\left\langle \left(\theta_A - \langle\theta_A\rangle\right)\left(\theta_B - \langle\theta_B\rangle\right)\right\rangle\right)$, are summarized in tables 4 and 5.

4.2.2 TEMPORAL CORRELATIONS

A third feature apparent in figure 16 is the increasing correlation time as $d \rightarrow d_c$. In figure 18, we show the plots of the function $C(\delta t)$ (as defined in eq. 37), versus δt for selected values of d, and for both the reactive and inactive branches for a 150x150 lattice. For each value of d, the $C(\delta t)$-plot decreases in size, from its maximum value $C(\delta t) = 1$ at $\delta t = 0$. As can be seen in figure 19, this correlation time increases as $d \rightarrow d_c$, from the left; in particular, it would approach infinity for an infinite lattice. Thus, as $d \rightarrow d_c$, the simulations must run for longer and longer times in order to get reliable statistics for the steady-state lattice.

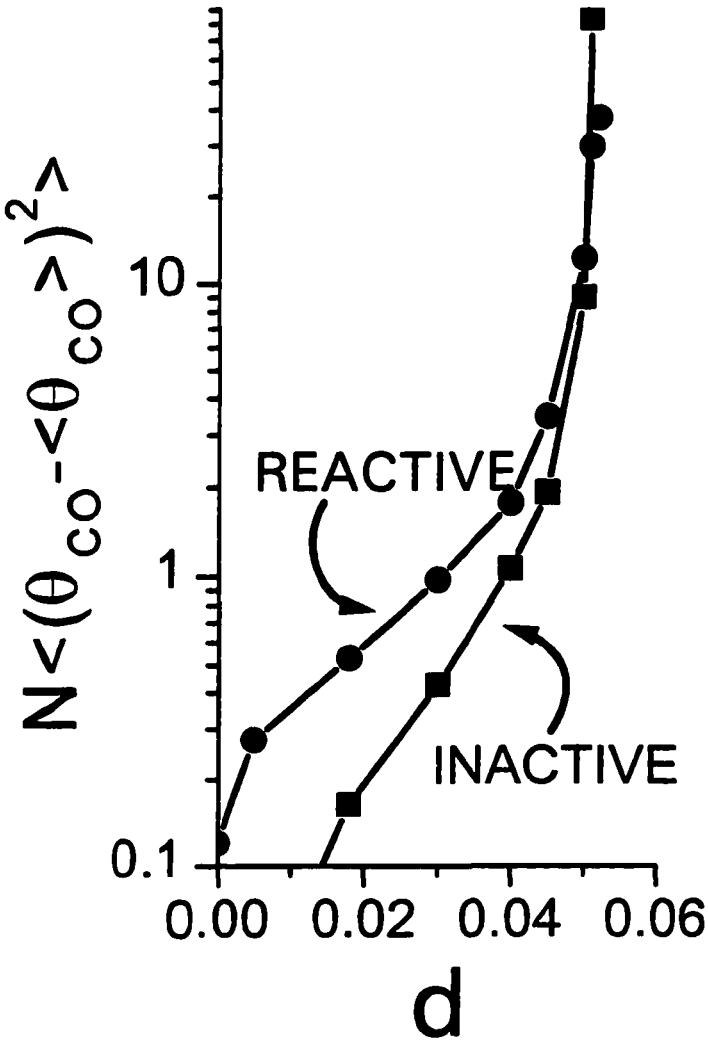

Figure 17. The amplitudes of the θ_A-fluctuations for the inactive branch are less than for the reactive branch, as can be seen here. A plot of the θ_B-fluctuations versus d looks similar. These fluctuations and the anti-correlation data, $(\langle(\theta_A - \langle\theta_A\rangle)(\theta_B - \langle\theta_B\rangle)\rangle)$, is summarized in tables 4 and 5.

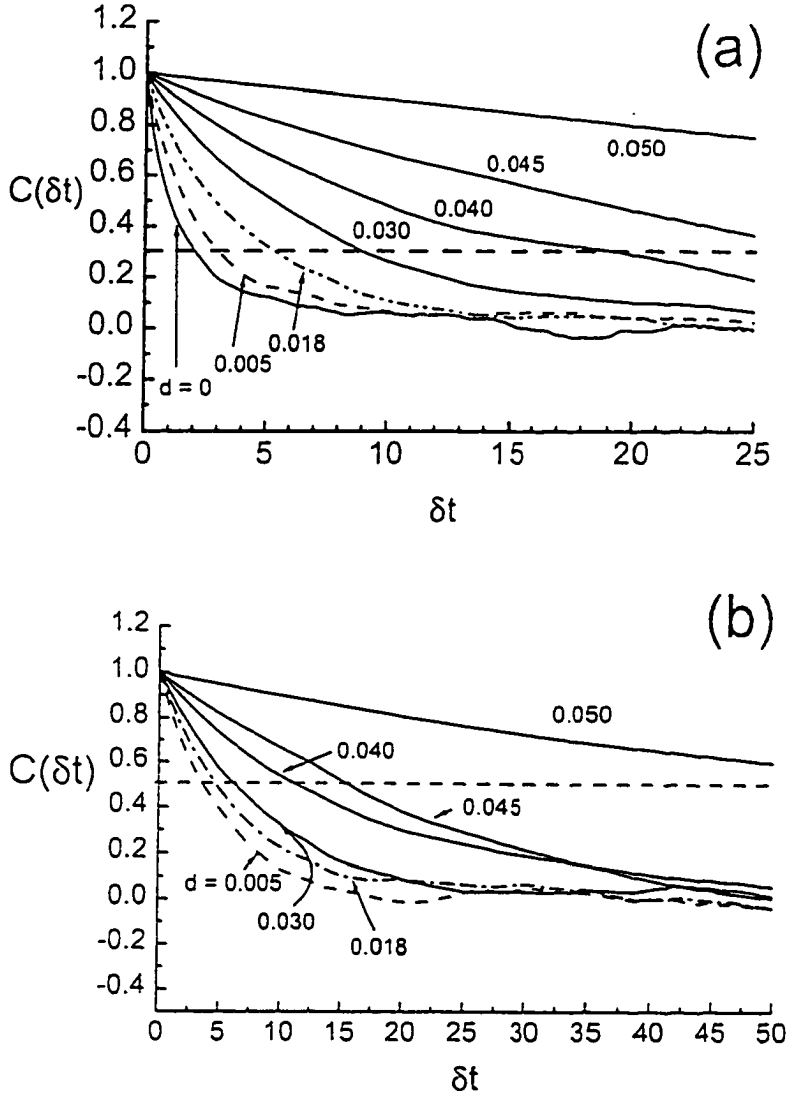

Figure 18. Plots of the function C(δt) versus δt for selected values of d, for both the (a) reactive and the (b) inactive branches for a 150×150 lattice. For each value of d, the C(δt)-plot decreases in size, from its maximum value C(δt) = 1 at δt = 0. We define the correlation time, T_{corr}, as the value of δt at which C(δt) has dropped down to C(δt) = 0.5.

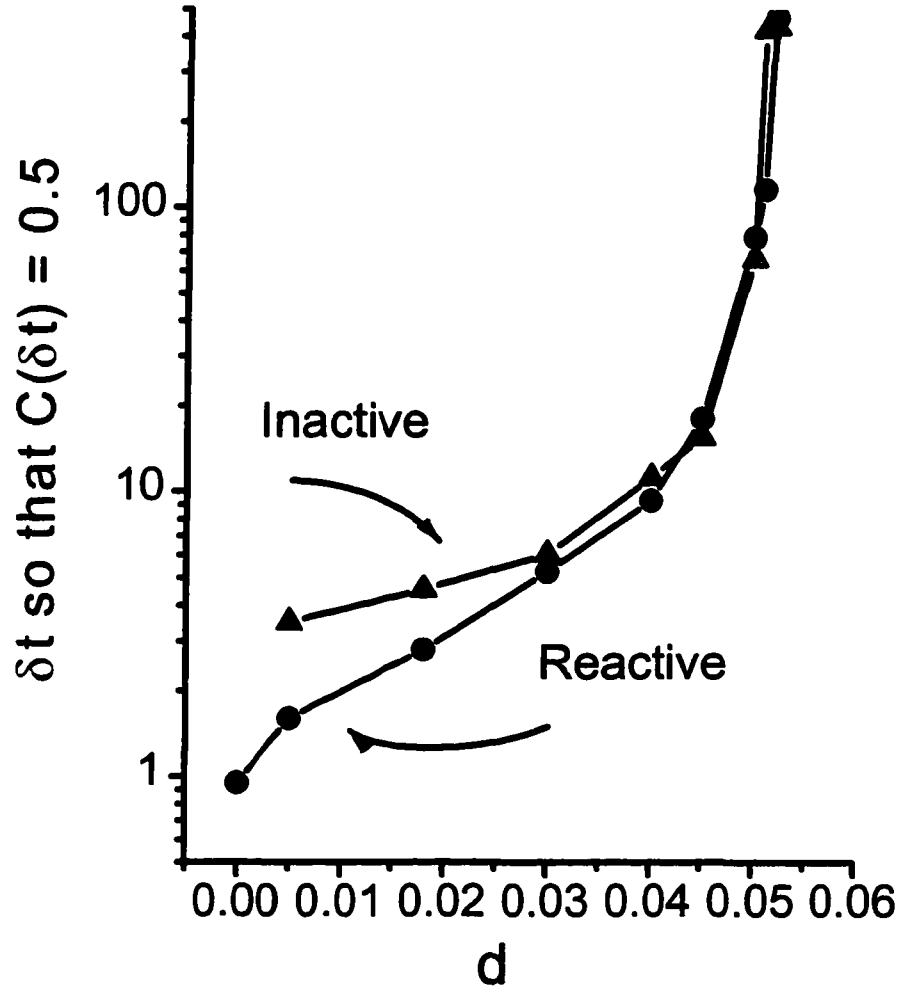

Figure 19. The correlation time T_{corr}, increases as $d \rightarrow d_c$, from the left In particular, it would approach infinity for an infinite lattice. Thus, as $d \rightarrow d_c$, the simulations must run for longer and longer times in order to get reliable statistics for the steady-state lattice.

Table 4. Fluctuation amplitudes and the anti-correlation data for 150×150 lattice for the reactive steady-state.

d	P_A	$\langle\theta_A\rangle$	$\langle\theta_B\rangle$	$N\langle(\theta_A-\langle\theta_A\rangle)^2\rangle$	$N\langle(\theta_B-\langle\theta_B\rangle)^2\rangle$	$N\langle(\theta_A-\langle\theta_A\rangle)\times(\theta_B-\langle\theta_B\rangle)\rangle$
0.000	0.18020	0.09754	0.23550	0.1200	0.1484	-0.06070
0.005	0.27115	0.20510	0.17030	0.2743	0.1184	-0.08415
0.018	0.33585	0.31770	0.12500	0.5279	0.1232	-0.15050
0.030	0.37005	0.40320	0.09681	0.9741	0.1425	-0.26340
0.040	0.39220	0.48340	0.07389	1.7730	0.1666	-0.43310
0.045	0.40095	0.52860	0.06225	3.4550	0.2445	-0.80980
0.050	0.40915	0.58860	0.04829	12.1700	0.5912	-2.57200
0.051	0.41070	0.69130	0.02832	29.6300	0.9319	-5.16100
0.052	0.41235	0.67090	0.03199	37.2400	1.2700	-6.78200
0.053	0.41385	0.66660	0.03256	19.5400	0.6834	-3.55800

Table 5. Fluctuation amplitudes and the anti-correlation data for 150×150 lattice for the (a) inactive steady-state.

d	P_A	$\langle\theta_A\rangle$	$\langle\theta_B\rangle$	$N\langle(\theta_A-\langle\theta_A\rangle)^2\rangle$	$N\langle(\theta_B-\langle\theta_B\rangle)^2\rangle$	$N\langle(\theta_A-\langle\theta_A\rangle)\times(\theta_B-\langle\theta_B\rangle)\rangle$
0.000	0.18020	1.0000	0.0000000	0.00000	0.0000000	0.0000000
0.005	0.27115	0.9793	0.0001604	0.02877	0.0002442	-0.0005354
0.018	0.33585	0.9300	0.0016310	0.16330	0.0028040	-0.0087900
0.030	0.37005	0.8781	0.0047930	0.42520	0.0093370	-0.0347600
0.040	0.39220	0.8258	0.0094130	1.06300	0.0248800	-0.1167000
0.045	0.40095	0.7901	0.0134500	1.92100	0.0481000	-0.2454000
0.050	0.40915	0.7243	0.0227200	8.95400	0.2503000	-1.4180000
0.051	0.41070	0.6431	0.0377400	82.83000	2.9710000	-15.5700000
0.052	0.41235	0.6458	0.0365800	30.11000	1.1070000	-5.6700000
0.053	0.41385	0.6664	0.0326100	20.74000	0.7245000	-3.7790000

4.2.3 NOISE-INDUCED TRANSITIONS AND COVERAGE DISTRIBUTIONS

For a fixed value of d, one can thus see that the amplitude of the fluctuations in coverages must decrease to zero as N approaches infinity. Consequently, a large system in the reactive branch would be expected to remain in the reactive branch almost forever, and likewise for a system in the inactive branch, since small fluctuations could not induce transitions between these states. We should thus expect monomodal [A] (or [B]) concentration distributions for very large lattices.

For smaller lattices, however, it is fair to ask if the system is likely to flip back and forth between the active and inactive branches, thus producing a bimodal coverage distribution. From eq. 38, we can see two ways, which could help the system to make such transitions. First, one could decrease the system size, N, to increase fluctuation amplitudes. Secondly, letting d increase toward the critical value d_c will cause $K_{d,n}$, and hence the fluctuation amplitudes, to increase. In fact, we have observed this system-flipping for lattices of size 30x30, and an observation time of 3200, sufficiently close to d_c.

Figure 20 shows the θ_A-concentration histograms, for selected values of d and corresponding P_A(midpoint), for 30x30 lattices, each with empty initial conditions. In fact, we see that the system displays a monomodal concentration distribution for lower values of d and switches to bimodal behavior as d grows closer to d_c. The peaks of the histograms indicate the locations of the reactive steady state (low θ_A) and the inactive steady state (high θ_A). For the bimodal graphs, the relative areas of these peaks are proportional to the amount of time the system spends on either of these branches, thus indicating their relative stability—

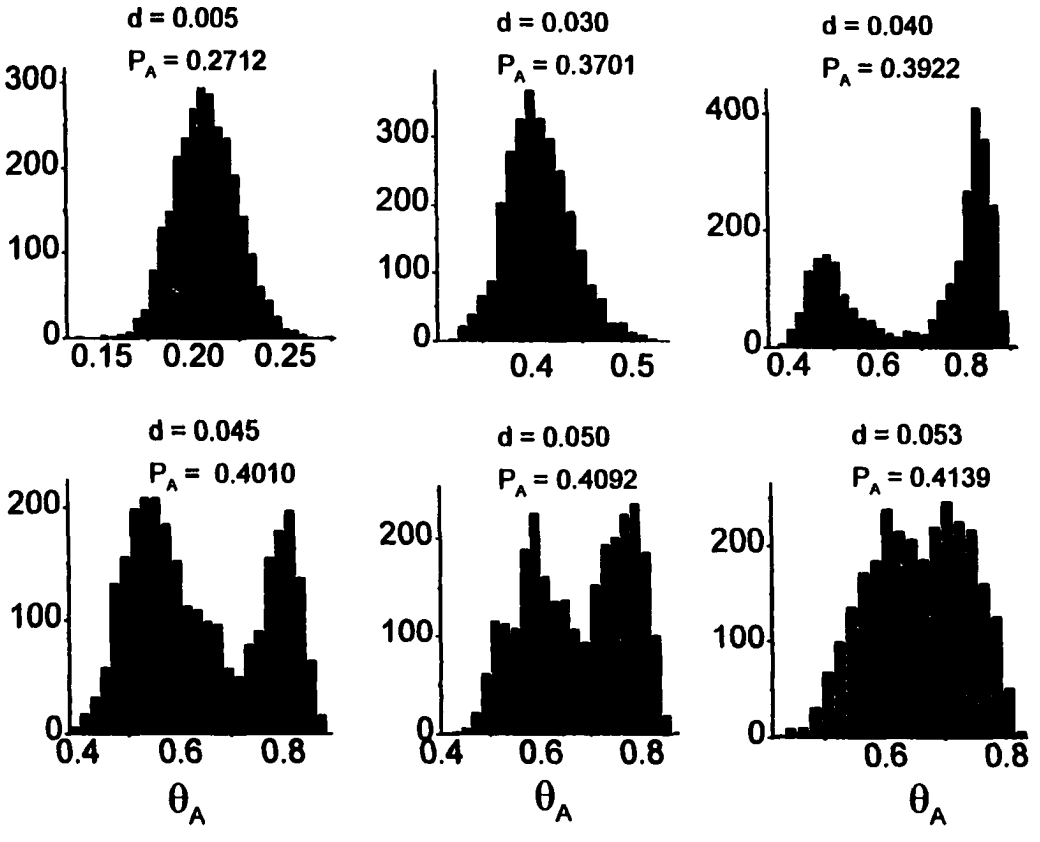

Figure 20. θ_A-concentration histograms, for selected values of d and corresponding P_A(midpoint), for 30x30 lattices, each with empty initial conditions, and run for 3200 physical time units. The system displays a monomodal concentration distribution for lower values of d and switches to bimodal behavior as d grows closer to d_c.

the larger area corresponding to the more stable branch. We observed similar behavior for a 60x60 lattice (see figure 21).

Finally, choosing a 30x30 lattice and a fixed d-value, d = 0.040, which gave a clear bimodal graph in figure 20, we now scan across the bistability region given by $0.3527 \leq P_A \leq 0.3874$, to obtain the θ_A– and θ_B–concentration distributions, for an observation time of 300,000. The result is that on the left-hand side of the bistability region, the more stable steady-state branch is the reactive one, while on the right-hand side, the more stable branch is the inactive one, as is illustrated in figures 22 and 23.

4.3 APPROXIMATE ANALYTIC TREATMENT

For the spontaneous symmetry-breaking transition, we have shown in Sec.3.3 that an approximate analytic treatment can reproduce the qualitative or gross behavior of the transition (but not the quantitative details). Thus, it is natural to ask such an analytic treatment could also elucidate qualitatively behavior near the cusp bifurcation, specifically the increase in the amplitude of coverage fluctuations, and in the correlation time. Indeed this turns out to be the case, although here we just sketch the results.

It is easiest first to consider and elucidate the increase in the correlation time (sometimes referred to as "critical slowing down"). To this end, it is instructive to consider the response of a spatially uniform reaction system to slight perturbations from the steady state. This response is described by the exact master equations given in eq. 11(a) and eq. 14. Applying the pair approximation to these equations produces a closed coupled non-linear pair of equations [5], upon which one can perform a standard linear stability analysis [13].

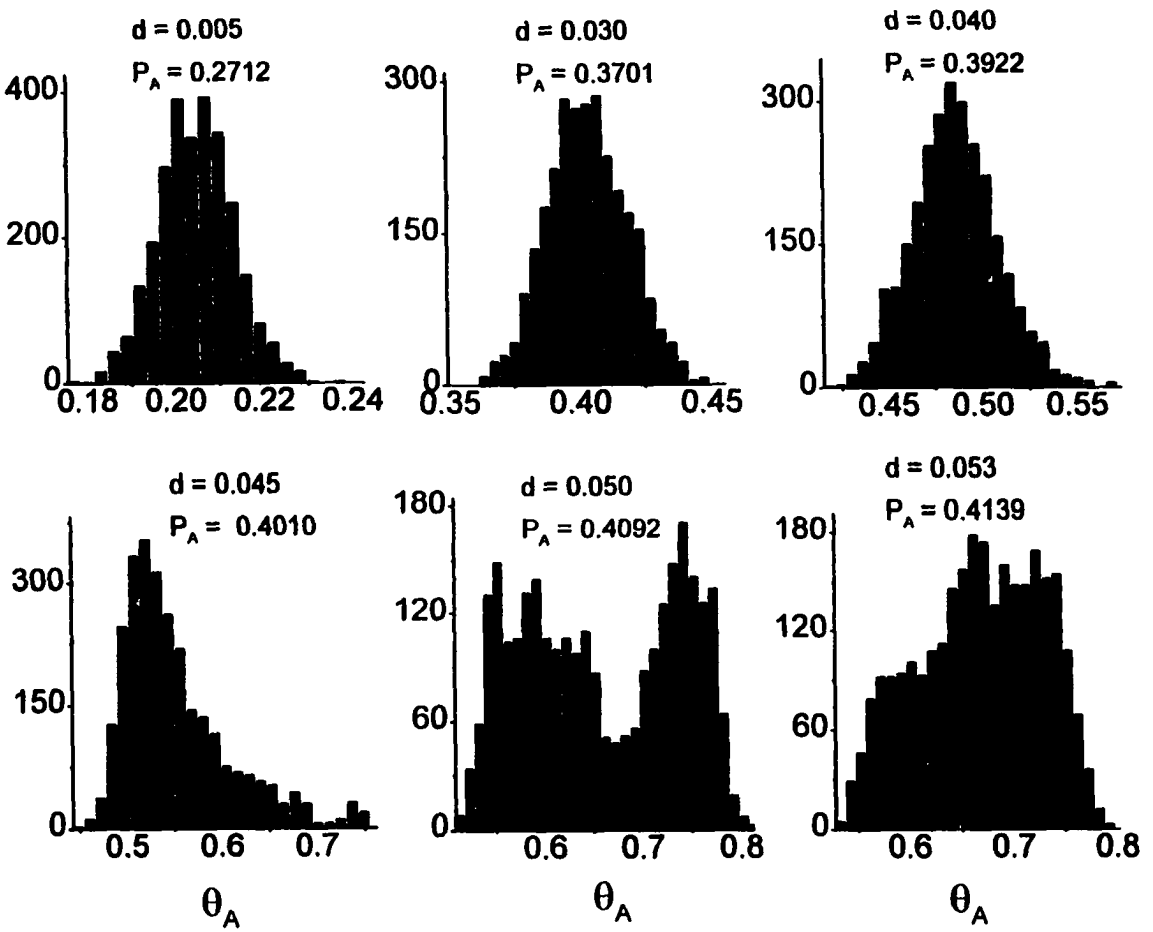

Figure 21. θ_A-concentration histograms, for selected values of d and corresponding P_A(midpoint), for 60x60 lattices, each with empty initial conditions, and run for 3200 physical time units. The system displays a monomodal concentration distribution for lower values of d and switches to bimodal behavior as d grows closer to d_c.

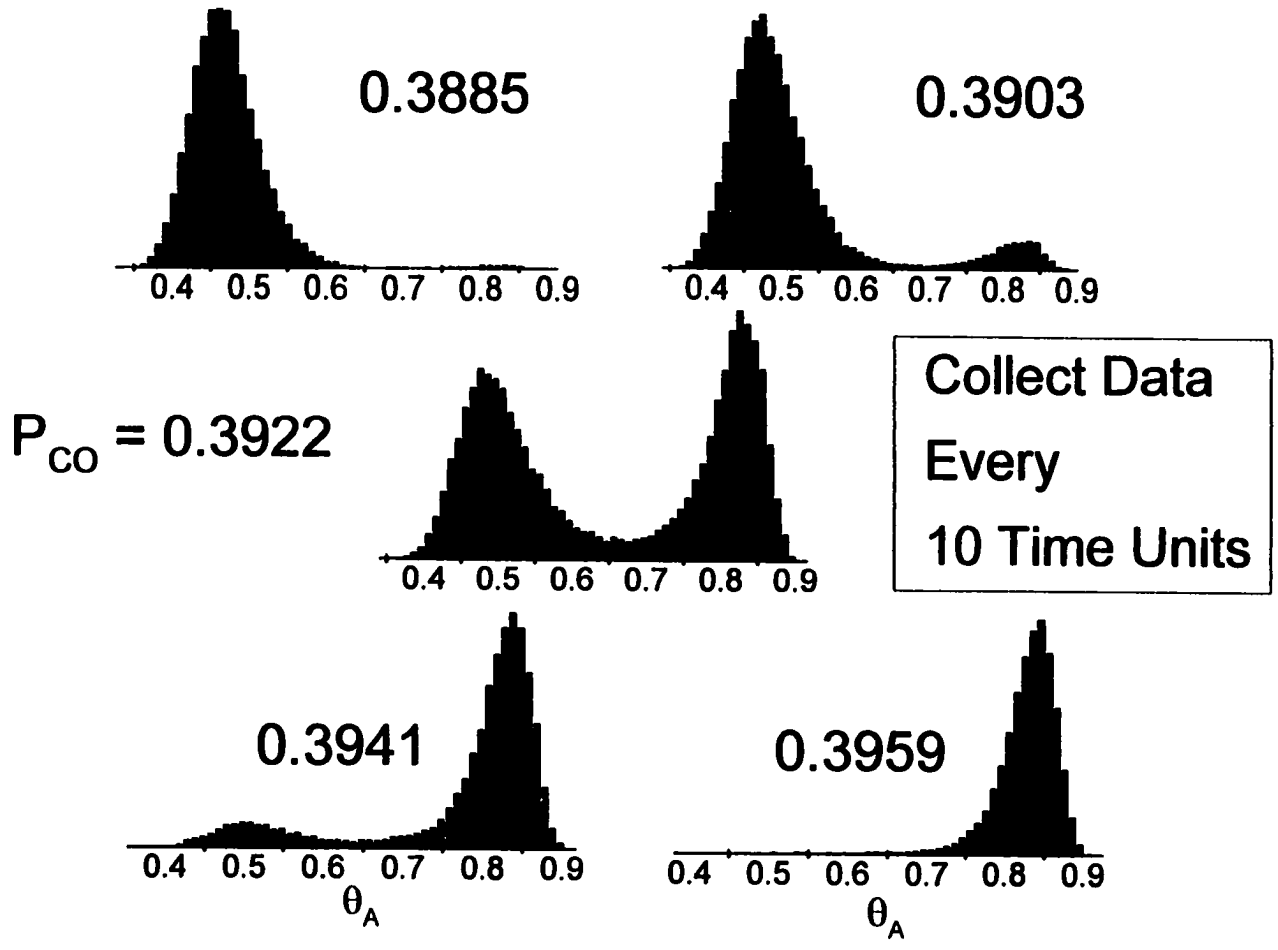

Figure 22. For a 30x30 lattice and a fixed d-value, d = 0.040, which gave a nice bimodal graph in figure 20, we now scan across the bistability region given by $0.3527 \leq P_A \leq 0.3874$, to obtain the θ_A-concentration distributions. The result is that on the left-hand side of the bistability region, the more stable steady-state branch is the reactive one, while on the right-hand side, the more stable branch is the inactive one. These simulations were run for a physical time of 300,000.

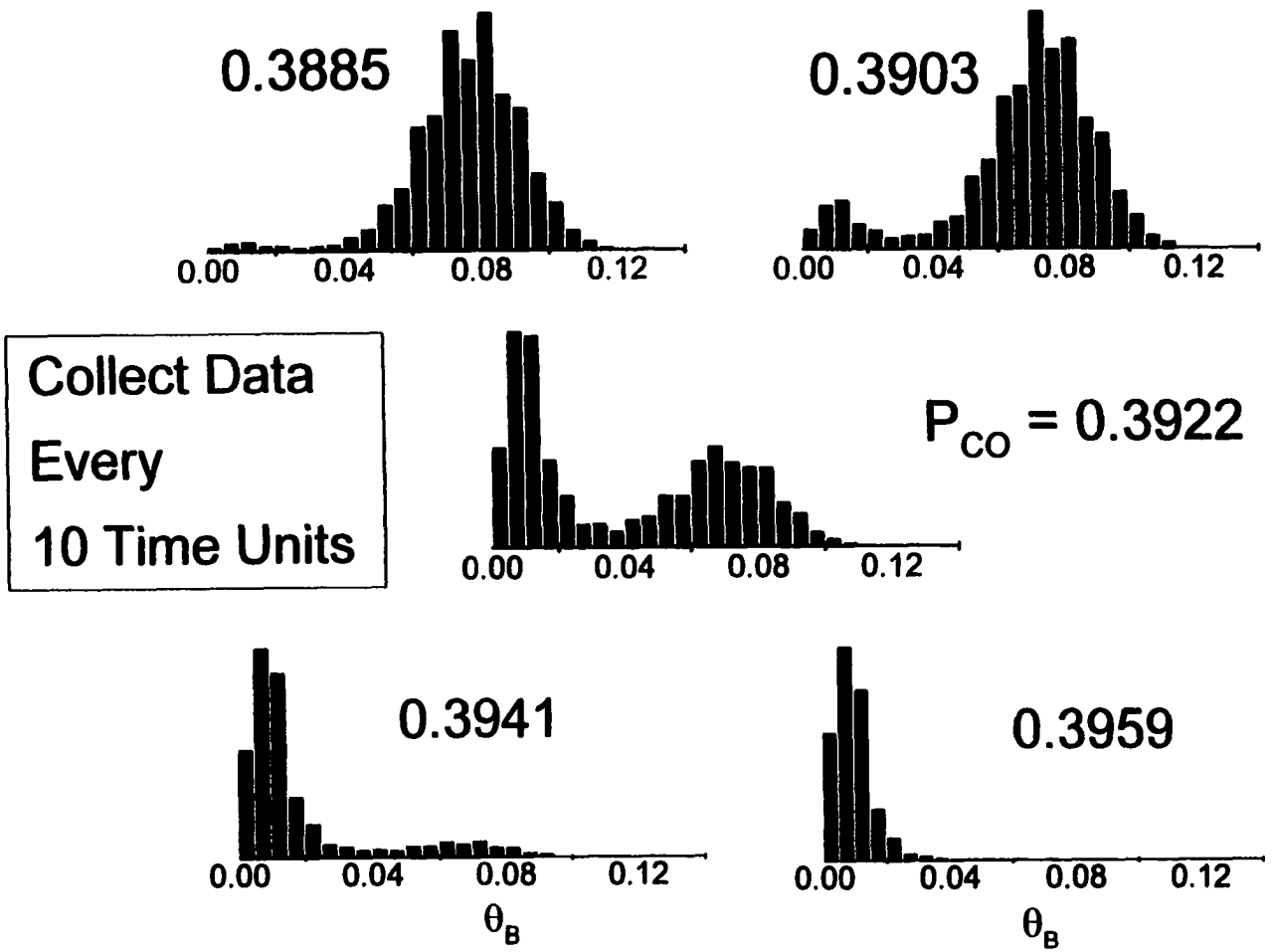

Figure 23. For a 30x30 lattice and a fixed d-value, d = 0.040, which gave a nice bimodal graph in figure 20, we now scan across the bistability region given by $0.3527 \leq P_A \leq 0.3874$, to obtain the θ_B-concentration distributions. The result is that on the left-hand side of the bistability region, the more stable steady-state branch is the reactive one, while on the right-hand side, the more stable branch is the inactive one. These simulations were run for a physical time of 300,000.

From general bifurcation theory, we know that one of the two eigenvalues describing the rate of decay to the steady state (which are obtained from the associated Jacobian matrix) must vanish at the cusp bifurcation. This corresponds to the observed critical slowing phenomenon.

It is more difficult to provide insight into the enhanced coverage fluctuations. The most convenient strategy here is to exploit the direct relationship given in Appendix A between the amplitude of these fluctuations and the spatial correlations. Then, to understand the enhanced fluctuations, it suffices to demonstrate an increase in the spatial correlation length approaching the cusp bifurcation. To this end, it is appropriate to consider the response of the reaction system to spatially localized perturbations from the steady state. This response is described by the most general form of the master equations given in Sec.2.3 (which does not assume translational invariance). Analysis of these equations is possible after using a pair approximation to provide an infinite coupled nonlinear set of equations involving only the species coverages, [Aij] and [Bij], at various sites. The technical details will not be presented here, but the basic result is that the vanishing of an eigenvalue describing decay rates in uniform systems drives the increase the spatial correlation lengths upon approaching the cusp bifurcation. Somewhat analogous behavior is observed in reaction-diffusion systems [14].

5. SUMMARY

Our detailed study of fluctuations and critical phenomena in our lattice-gas reaction model for CO-oxidation has revealed surprisingly similar behavior to that long studied in equilibrium systems (where the steady states are described by a Gibbs measure). The

similarities between behavior at a cusp bifurcation in a non-equilibrium system and at a critical point in an equilibrium system have been long recognized. However, the presence of spontaneous symmetry breaking transitions in non-equilibrium models is a novel phenomenon, and the current study provides the first detailed analysis of this issue.

ACKNOWLEDGEMENTS

This work was supported by the Division of Chemical Sciences, Office of Basic Energy Sciences, of the U.S. Department of Energy (USDOE). It was performed at Ames Laboratory, which is operated for the USDOE by Iowa State University under Contract No. W-7405-Eng-82.

APPENDIX A: FLUCTUATION–(SPATIAL) CORRELATION RELATIONS

In this section, we justify the statement made in eq. 36, that, for a translation-invariant system, the fluctuations in species concentration about its average value goes roughly as 1/N, where N is the size of the lattice. For the following discussion, we now restrict ourselves to the translation-invariant systems with periodic boundary conditions. We first define the occupation number of adspecies J by:

$$n_{\underline{\ell}}^{J} = \begin{cases} 1, & \text{if } \underline{\ell} \text{ is occupied by J;} \\ 0, & \text{else.} \end{cases} \qquad \text{eq. 39}$$

Then formally we have, for the average ensemble concentration of J species:

$$[J] = \underset{(i,j)}{\text{avg}}\,[J_{ij}] = \frac{\sum_{\underline{\ell}} \langle n^J_{\underline{\ell}} \rangle}{N} = \langle \theta_J \rangle, \quad \underline{\ell} = (i,j); \qquad \text{eq. 40}$$

Next, we note that, because of translation-invariance, the average occupation numbers are the same for all sites on the lattice. In other words, we have $\langle n^J_{\underline{\ell}} \rangle = \langle n^J_{\underline{\ell}'} \rangle$, for any two sites $\underline{\ell}$, and $\underline{\ell}'$, and using eq. 18, this yields:

$$[J] = \langle \theta_J \rangle = \frac{\sum_{\underline{\ell}} \langle n^J_{\underline{\ell}} \rangle}{N} = \frac{N \langle n^J_{\underline{\ell}'} \rangle}{N} = \langle n^J_{\underline{\ell}'} \rangle. \qquad \text{eq. 41}$$

Therefore, in the translation-invariant lattice, we have that the average ensemble concentration of the J species is equal to the average occupation number at any single site $\underline{\ell}'$ on the lattice.

Next, we observe that the probability of the event that one J-particle is located at $\underline{\ell}$, while one J′-particle is located at site $\underline{\ell}'$ is given by:

$$P_{JJ'}(\underline{\ell} - \underline{\ell}') = \langle n^J_{\underline{\ell}} \; n^{J'}_{\underline{\ell}'} \rangle \cong \langle n^J_{\underline{\ell}} \rangle \langle n^{J'}_{\underline{\ell}'} \rangle, \text{ for large } \underline{\ell} - \underline{\ell}'. \qquad \text{eq. 42}$$

In the case when J = J′, eq. 42 reduces to:

$$P_J(\underline{\ell} - \underline{\ell}') = \left\langle n^J_{\underline{\ell}}\ n^J_{\underline{\ell}'} \right\rangle \equiv \left\langle n^J_{\underline{\ell}} \right\rangle^2, \text{ for large } \underline{\ell} - \underline{\ell}'. \qquad \text{eq. 43}$$

We now make the following general computation:

$$\left\langle (\theta_J - \langle \theta_J \rangle)(\theta_{J'} - \langle \theta_{J'} \rangle) \right\rangle = \frac{1}{N^2} \sum_{\underline{\ell}'} \sum_{\underline{\ell}} \left\langle \left(n^J_{\underline{\ell}} - \left\langle n^J_{\underline{\ell}} \right\rangle\right)\left(n^{J'}_{\underline{\ell}'} - \left\langle n^{J'}_{\underline{\ell}'} \right\rangle\right) \right\rangle$$

$$= \frac{1}{N^2} \sum_{\underline{\ell}'} \sum_{\underline{\ell}} \left(\left\langle n^J_{\underline{\ell}}\ n^{J'}_{\underline{\ell}'} \right\rangle - \left\langle n^J_{\underline{\ell}} \right\rangle \left\langle n^{J'}_{\underline{\ell}'} \right\rangle \right) = \frac{1}{N^2} \sum_{\underline{\ell}'} \left(\sum_{\underline{\ell}} C_{JJ'}(\underline{\ell} - \underline{\ell}') \right), \qquad \text{eq. 44}$$

where the spatial correlation, $C_{JJ'}(\underline{\ell} - \underline{\ell}')$, between two adspecies J and J′, located at the lattice sites $\underline{\ell}$ and $\underline{\ell}'$, respectively is given by:

$$C_{JJ'}(\underline{\ell} - \underline{\ell}') = P_{JJ'}(\underline{\ell} - \underline{\ell}') - \langle \theta_J \rangle \langle \theta_{J'} \rangle \equiv 0, \text{ for large separations } \underline{\ell} - \underline{\ell}', \qquad \text{eq. 45}$$

because of eq. 42 and eq. 41. Again, in the case when J = J′, eq. 44 and eq. 45 reduce to:

$$\left\langle (\theta_J - \langle \theta_J \rangle)^2 \right\rangle = \frac{1}{N^2} \sum_{\underline{\ell}'} \sum_{\underline{\ell}} \left\langle \left(n^J_{\underline{\ell}} - \left\langle n^J_{\underline{\ell}} \right\rangle\right)\left(n^J_{\underline{\ell}'} - \left\langle n^J_{\underline{\ell}'} \right\rangle\right) \right\rangle$$

$$= \frac{1}{N^2} \sum_{\underline{\ell}'} \sum_{\underline{\ell}} \left(\left\langle n^J_{\underline{\ell}}\ n^J_{\underline{\ell}'} \right\rangle - \left\langle n^J_{\underline{\ell}} \right\rangle \left\langle n^J_{\underline{\ell}'} \right\rangle \right) = \frac{1}{N^2} \sum_{\underline{\ell}'} \left(\sum_{\underline{\ell}} C_J(\underline{\ell} - \underline{\ell}') \right), \qquad \text{eq. 46}$$

where the spatial correlation, $C_J(\underline{\ell} - \underline{\ell}')$, between two adspecies elements J, one located at site $\underline{\ell}$ and the other at $\underline{\ell}'$, is given by:

$$C_J(\underline{\ell} - \underline{\ell}') = P_J(\underline{\ell} - \underline{\ell}') - \langle\theta_J\rangle^2 \equiv 0, \text{ for large separations } \underline{\ell} - \underline{\ell}', \qquad \text{eq. 47}$$

because of eq. 43 and eq. 41.

Next, if we fix $\underline{\ell}'$ and compute the summation inside the parentheses in the last term of eq. 44, we find that this sum is independent of $\underline{\ell}'$, by the following argument. First, label each of the N sites on the lattice by the vector positions $\underline{0}, \underline{1}, \underline{2}, \ldots \underline{N\text{-}1}$. Next, define $C_{JJ'}(\underline{\ell})$ as the spatial correlation of the adspecies J and J′ located at positions $\underline{0}$ and $\underline{\ell}$, respectively (i.e. $C_{JJ'}(\underline{\ell}) = C_{JJ'}(\underline{\ell} - \underline{0})$). Finally, by translation-invariance, we have:

$$\sum_{\underline{\ell}} C_{JJ'}(\underline{\ell} - \underline{\ell}') = \sum_{\underline{\ell}} C_{JJ'}(\underline{\ell} - \underline{0}) = \sum_{\underline{\ell}} C_{JJ'}(\underline{\ell}). \qquad \text{eq. 48}$$

Hence, eq. 44 reduces to:

$$\left\langle \left(\theta_J - \langle\theta_J\rangle\right)\left(\theta_{J'} - \langle\theta_{J'}\rangle\right)\right\rangle = \frac{1}{N^2}\sum_{\underline{\ell}'}\left(\sum_{\underline{\ell}} C_{JJ'}(\underline{\ell})\right) = \frac{1}{N}\sum_{\underline{\ell}} C_{JJ'}(\underline{\ell}). \qquad \text{eq. 49}$$

If $J = J'$, and $C_J(\underline{\ell})$ is defined by $C_J(\underline{\ell}) = C_J(\underline{\ell} - \underline{0})$, then eq. 49 reduces to:

$$\left\langle \left(\theta_J - \langle\theta_J\rangle\right)^2 \right\rangle = \frac{1}{N^2}\sum_{\underline{\ell}'}\left(\sum_{\underline{\ell}} C_J(\underline{\ell})\right) = \frac{1}{N}\sum_{\underline{\ell}} C_J(\underline{\ell}), \qquad \text{eq. 50}$$

It is instructive to consider two special cases for the spatial correlations in eq. 45.

First, for randomly distributed species, we have for $J \neq J'$:

$$C_{JJ'}(\underline{\ell}) = \left\langle n^J_{\underline{\ell}}\, n^{J'}_{\underline{0}} \right\rangle - \left\langle n^J_{\underline{\ell}} \right\rangle \left\langle n^{J'}_{\underline{0}} \right\rangle = \begin{cases} 0 - \left\langle n^J_{\underline{\ell}} \right\rangle \left\langle n^{J'}_{\underline{\ell}} \right\rangle = -\left\langle \theta_J \right\rangle \left\langle \theta_{J'} \right\rangle, & \text{for } \underline{\ell} = \underline{\underline{0}}; \\ 0, & \text{for } \underline{\ell} \neq \underline{\underline{0}}. \end{cases} \quad \text{eq. 51}$$

while for $J = J'$:

$$C_J(\underline{\ell}) = \left\langle n^J_{\underline{\ell}}\, n^J_{\underline{0}} \right\rangle - \left\langle n^J_{\underline{\ell}} \right\rangle \left\langle n^J_{\underline{0}} \right\rangle = \begin{cases} \left\langle n^J_{\underline{\ell}} \right\rangle - \left\langle n^J_{\underline{\ell}} \right\rangle^2 = \left\langle \theta_J \right\rangle \left(1 - \left\langle \theta_J \right\rangle\right), & \text{for } \underline{\ell} = \underline{\underline{0}}; \\ 0, & \text{for } \underline{\ell} \neq \underline{\underline{0}}. \end{cases} \quad \text{eq. 52}$$

Thus, eq. 49 and eq. 50 reduce to:

$$\left\langle \left(\theta_J - \left\langle \theta_J \right\rangle\right)\left(\theta_{J'} - \left\langle \theta_{J'} \right\rangle\right) \right\rangle = -\frac{1}{N} \left\langle \theta_J \right\rangle \left\langle \theta_{J'} \right\rangle < 0 \,, \text{ for } J \neq J', \quad \text{eq. 53}$$

which yields that the fluctuations in $\theta_{J'}$ and θ_J are anti-correlated; and

$$\left\langle \left(\theta_J - \left\langle \theta_J \right\rangle\right)^2 \right\rangle = \frac{1}{N} \left\langle \theta_J \right\rangle \left(1 - \left\langle \theta_J \right\rangle\right) \,, \text{ for } J = J'. \quad \text{eq. 54}$$

Second, when the J-species cannot occupy NN-sites, we have:

$$C_J(\underline{\ell}) = \left\langle n^J_{\underline{\ell}}\, n^J_{\underline{0}} \right\rangle - \left\langle n^J_{\underline{\ell}} \right\rangle \left\langle n^J_{\underline{0}} \right\rangle = -\left\langle n^J_{\underline{\ell}} \right\rangle^2 = -\langle \theta_J \rangle^2, \text{ in the case } \underline{\ell} \text{ is NN to } \underline{0}. \qquad \text{eq. 55}$$

In this case, eq. 50 reduces to:

$$\left\langle \left(\theta_J - \langle \theta_J \rangle\right)^2 \right\rangle = \frac{1}{N}\langle \theta_J \rangle (1 - \langle \theta_J \rangle) - 4\langle \theta_J \rangle^2 + (\|\underline{\ell}\| > 1 \text{ terms}) \qquad \text{eq. 56}$$

APPENDIX B: PROBABILITY RELATIONSHIPS FOR NON-UNIFORM SYSTEMS

We prove the two relations given in eq. 2 of Section 2.2, namely that:

$$\frac{[A_{ij}]}{[Z_{ij}]} = \frac{[A]}{[Z]} \quad \text{and} \quad \frac{[E_{ij}]}{[Z_{ij}]} = \frac{[E]}{[Z]}.$$

These may be proved as follows. First, spatial uniformity of A's yields:

$$\frac{[A_{ij}]}{[Z_{ij}]} = K, \quad \text{a constant, for every (i, j) pair.} \qquad \text{eq. 57}$$

Second, the definition of any coverage goes as follows:

$$[A] = \frac{\sum_{i,j} \left\langle n^A_{ij} \right\rangle}{N} = \frac{\sum_{i,j} [A_{ij}]}{N}. \qquad \text{eq. 58}$$

Therefore, we have:

$$\frac{[A]}{[Z]} = \frac{\left(\frac{\sum_{i,j}[A_{ij}]}{N}\right)}{\left(\frac{\sum_{i,j}[Z_{ij}]}{N}\right)} = \frac{\sum_{i,j}[A_{ij}]}{\sum_{i,j}[Z_{ij}]} = \frac{\sum_{i,j}K*[Z_{ij}]}{\sum_{i,j}[Z_{ij}]} = K = \frac{[A_{ij}]}{[Z_{ij}]}, \qquad \text{eq. 59}$$

where the third and fifth equalities in eq. 59 are obtained by taking advantage of eq. 57. Thus, the left-hand relation of eq. 2 is proved. For the right-hand relation of eq. 2, we use eq. 59 and eq. 1(b) as follows:

$$\frac{[E]}{[Z]} = \frac{[Z]-[A]}{[Z]} = 1-\frac{[A]}{[Z]} = 1-\frac{[A_{ij}]}{[Z_{ij}]} = \frac{[Z_{ij}]-[A_{ij}]}{[Z_{ij}]} = \frac{[E_{ij}]}{[Z_{ij}]}, \qquad \text{eq. 60}$$

and eq. 2 is proved.

REFERENCES

[1] Weinberg; Binder and Landau. Ref.2 from Privman MS.

[2] Evans and Tammaro, Springer 1998.

[3] E.V. Albano, Hetero. Chem. Rev. **3**, 389 (1996); V.P. Zhdanov and B. Kasemo, Surf. Sci. Rep. **20**, 111 (1994); J.W. Evans, Langmuir **7**, 2514 (1991).

[4] Yu Suchorski, J. Beben, E. W. James, J. W. Evans, and R. Imbihl; "Fluctuation-induced transitions in a bistable surface reaction: catalytic CO oxidation on a Pt field emitter tip; Phys. Rev. Letters; Vol. 82, No. 9, pp. 1907-1910 (1999)

[5] E. W. James, C. Song, and J. W. Evans; "Co-oxidation Model with superlattice ordering of adsorbed oxygen I. Steady-state bifurcations; submitted to Journal of Chemical Physics

[6] R.M. Ziff, E. Gulari, and Y. Barshad, Phys. Rev. Lett. **50**, 2553 (1986).

[7] Ref.12 in Privman MS.

[8] C.R. Brundle, R.J. Behm, and J.A. Barker, J. Vac. Sci. Technol. A **2**, 1038 (1984); S.L. Chang and P.A. Thiel, Phys. Rev. Lett. **59**, 296 (1987).

[9] V.P. Zhdanov and B. Kasemo, Surf. Sci. **412/413**, 527 (1998).

[10] J.W. Evans and T.R. Ray, Phys. Rev. E **50**, 4301 (1994).

[11] M. Tammaro, M. Sabella, and J.W. Evans, J. Chem. Phys. **103**, 10277 (1995).

[12] M. Tammaro and J.W. Evans, J. Chem. Phys. **108**, 762 (1998).

[13] P.G. Drazin, Nonlinear Systems (Cambridge UP, Cambridge, 1992).

[14] A.S. Mikhailov and A. Yu Loskutov, Foundations of Synergetics II, (Springer, Berlin, 1996).

CHAPTER 4. FLUCTUATION-INDUCED TRANSITIONS IN A BISTABLE SURFACE REACTION: CATALYTIC CO OXIDATION ON A PT FIELD EMITTER TIP

A paper published in Physical Review Letters

Yu Suchorski[1], J. Beben[2], E.W. James[3], J.W. Evans[3] and R. Imbihl[1]

ABSTRACT

Fluctuations which arise in catalytic CO oxidation on a Pt field emitter tip have been studied with field electron microscopy as the imaging method. Fluctuation-driven transitions between the active and the inactive branch of the reaction are found to occur sufficiently close to the bifurcation point terminating the bistable range. The experimental results are modeled with Monte Carlo simulations of a lattice-gas reaction model incorporating rapid CO diffusion.

PACS numbers: 61.16Di, 82.20Mj, 82.20Wi, 82.65Jv

---

[1]Institut für Physikalische Chemie und Elektrochemie, Universität Hannover, Callinstr. 3 - 3a, D-30167 Hannover, Germany

[2]Institute of Experimental Physics, University of Wroclaw, pl. Maxa Borna 9, PL-50-204 Wroclaw, Poland

[3]Ames Laboratory and Department of Mathematics, Iowa State University, Ames, Iowa 50011, USA

Fluctuations are always present in chemical reaction systems due to the stochastic nature of the elementary processes including reaction and diffusion. In small scale systems, these fluctuations can become prominent and, as a consequence, one may observe new types of behavior not predicted by macroscopic (mean-field) rate laws [1-3]. In bistable systems, for example, such rate laws predict that the system resides on one of two steady-state branches for an indefinite period of time, whereas noise can cause a finite system to fluctuate between these two "stable" states. Mainly because of discrepancies from the predictions of macroscopic rate laws, noisy systems have attracted considerable theoretical interest [1-3]. There have also been experimental studies, e.g., of photosensitive reactions subject to external noise [3], and of intermittency in single-molecule spectroscopy studies [4], but few studies of the effect of fluctuations due to internal noise in non-linear reaction-diffusion (RD) systems.

In heterogeneous catalysis, sufficiently small systems to be strongly influenced by fluctuations (i.e., a few hundred up to a few thousand reacting particles) are provided by the facets of a field emitter tip [5], by nanostructured composite surfaces [6], and by the small metal particles (10-100 Å) of a supported catalyst [7]. Since supported catalysts represent the workhorse of real catalysis, an understanding of the reaction behavior of small systems bears also very practical ramifications.

In this Letter, we report on the observation of fluctuation-induced transitions in the bistable CO + O_2 reaction on a Pt field emitter tip. We compare these observations with results from Monte Carlo simulations of a surface reaction model which realistically describes key features of CO-oxidation including rapid CO diffusion (cf. Ref.[8]).

We employ field ion microscopy (FIM) with its high resolution of 3-4 Å (Fig. 1a) to identify the surface crystallography of the area probed by field electron microscopy (FEM) under reaction conditions with a much lower resolution of 20 Å [9]. The FEM video-images (40 ms/frame) were digitized with 8 bit resolution. In the following, we focus on a 20x200 $Å^2$ area in the vicinity of the (110) facet, indicated by the window in Fig. 1a. We note that the imaging field of 0.4 V/Å associated with FEM does not lead to detectable effects on the reaction [10].

The bifurcation diagram for catalytic CO oxidation for the [001]-oriented tip used in our experiments is displayed in Fig. 1c. The reaction exhibits two branches which coexist in the bistable range: an active branch in which the surface is predominantly oxygen covered so that CO can still adsorb and react, and an inactive branch on which a high CO coverage inhibits O_2 adsorption and hence poisons the reaction [11]. Remarkably, although the various orientations on the tip differ quite strongly in their reactivity (due to different oxygen sticking coefficients) [11], fast CO diffusion apparently ties the different facets together so that the tip behaves as one dynamical system.

In the following, we vary the temperature as bifurcation parameter (for fixed p_{CO} and pO_2) in the bistable region as indicated by the horizontal dashed line in Fig. 1c. A hysteresis results, as displayed in the inset of Fig. 1c. Local time series are obtained by integrating the FEM brightness in a small 20x20 $Å^2$ area inside the window marked in Fig. 1a. The local brightness in FEM depends mainly on the oxygen coverage which mostly affects work function changes (the intensity is low when the surface is oxygen covered, and it is high for a bare or CO-covered surface). The different time series displayed in Fig. 2a correspond to a

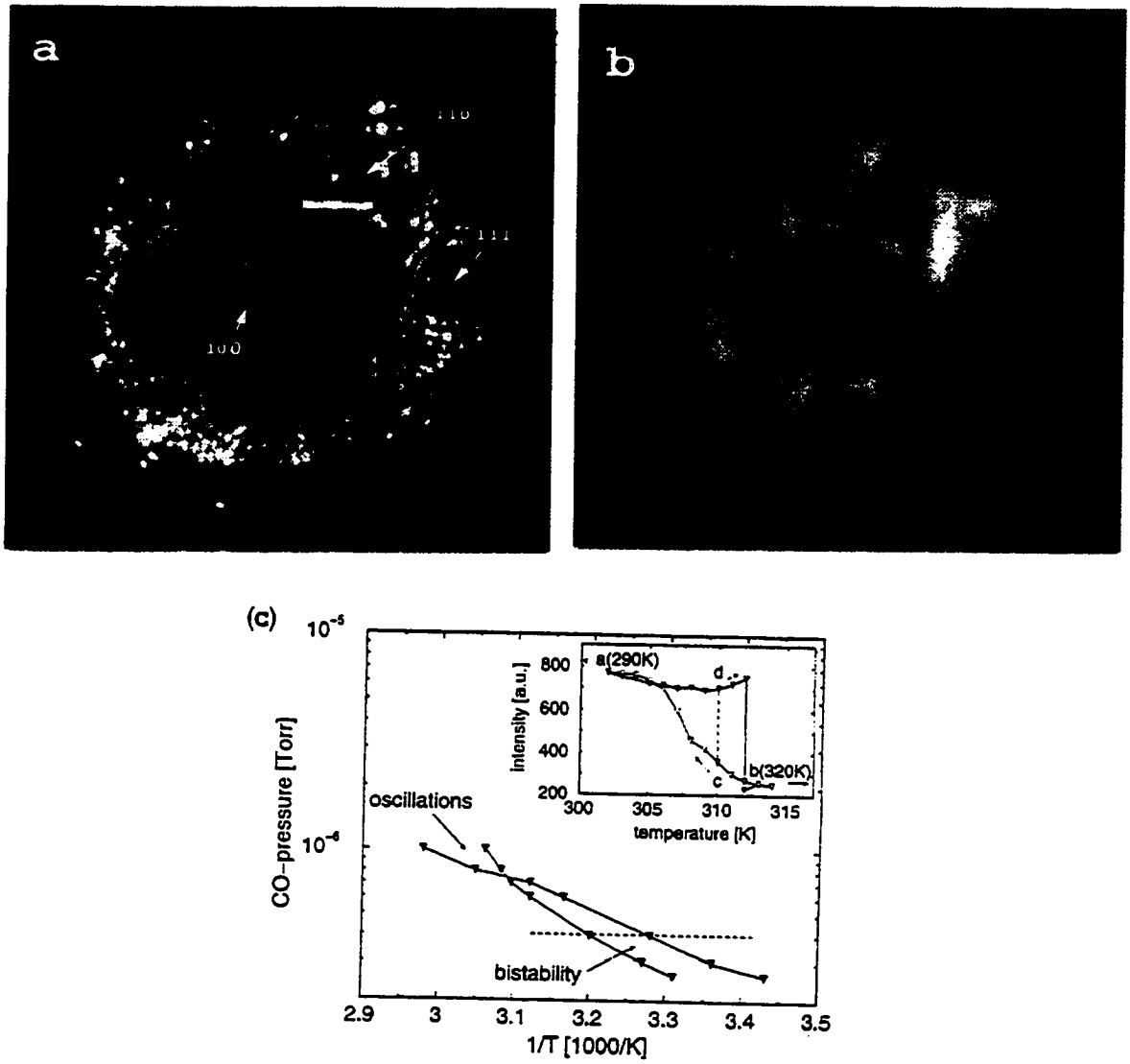

Figure 1. Catalytic CO oxidation on a Pt field emitter tip. (a) FIM image showing the crystallography of the Pt tip (T=78 K, imaging gas Ne, field strength F=3.6 V $Å^{-1}$). The rectangular window indicates the area in which fluctuations were studied.(b) FEM image of the same area (same scale) shown in (a) under reaction conditions (T=310 K, pO_2=4.0x10^{-4} Torr, p_{CO}=4x10^{-7} Torr , F= 0.4 V $Å^{-1}$). (c) Bifurcation diagram for catalytic CO oxidation on a [100]-oriented Pt tip at pO_2=4.0x10^{-4} Torr. The horizontal dashed line at p_{CO}=4x10^{-7} Torr marks the range in which the fluctuations were studied. The inset shows the hysteresis in local FEM brightness (20x20$Å^2$) for the area marked in (a) upon cyclic variation of T: filled triangles - heating, empty triangles - cooling.

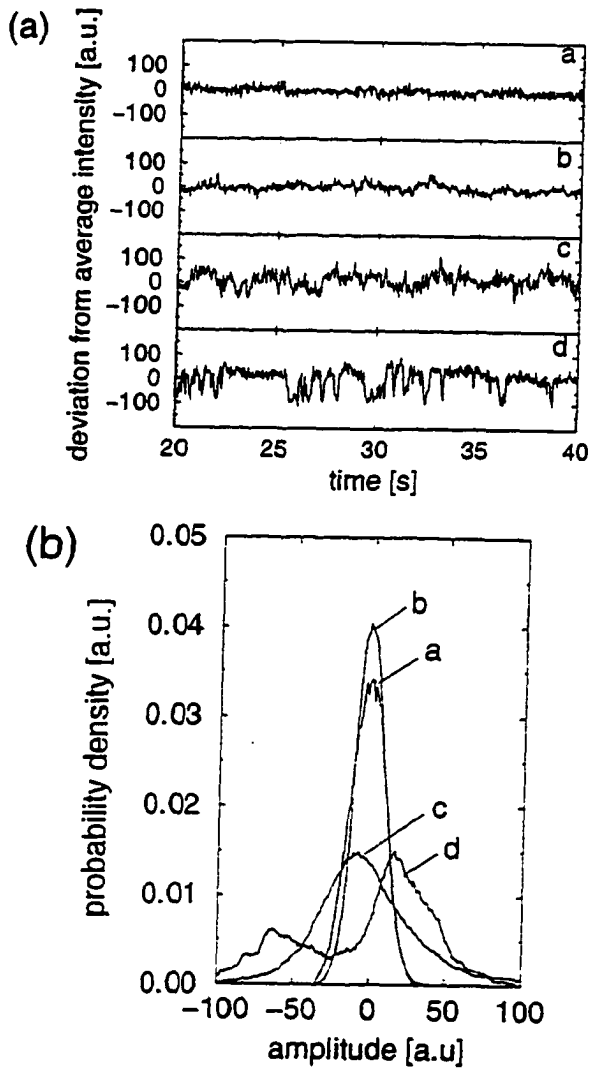

Figure 2. Fluctuations in catalytic CO oxidation on Pt under different reaction conditions. (a) Time series of the local (20x20 $Å^2$) FEM brightness in the area marked in Fig. 1a. The data were recorded at different points marked on the hysteresis loop in the inset of Fig. 1c. (b) Probability distributions corresponding to the time series shown in (a).

stable CO-covered (inactive) and a stable oxygen covered (active) surface in the monostable range (a,b in Fig.1c) and to states in the bistable range (c,d in Fig.1c) of the reaction.

From the time series, probability distributions of the intensity fluctuations have been constructed (Fig. 2b). In the monostable ranges (a,b) relatively narrow distributions of roughly Gaussian shape are found, but in the bistable range the distributions become rather broad. On the active branch, the peak just broadens and becomes slightly asymmetric (c), but on the inactive branch (d) the distribution actually becomes bimodal. This bimodal distribution is evidence for fluctuation (noise)-induced transitions between the two "stable" states, where the system is typically in one of these states, and spends comparatively little time in transition between them. We emphasize for smaller p_{CO} (i.e., further from the bifurcation point terminating the bistable range), the distributions remain roughly Gaussian even in the bistable range, i.e., no transitions were observed.

For the same p_{O2}, p_{CO}-parameters, fluctuations have also been studied on several other facets of the Pt tip [12]. In the bistable range, one typically finds strongly broadened probability distributions with the shape and asymmetry depending on the specific orientation, but a clear bimodal distribution was only seen in the vicinity of Pt(110). Spatial correlations in the fluctuations in this range typically extend over 100-200 Å on a single facet (reaching into the vicinal planes) [12], but they do not extend between different facets. Thus, although strong coupling via CO diffusion leads to identical bifurcation behavior, the fluctuations on different facets still retain local characteristics.

Next, we turn to the theoretical modeling. The most relevant previous work considered transitions induced by external noise in bistable systems described by simple potential models [2], fluctuations in homogeneous chemical reactions [3], and even a noise-

induced transition to bistability in a deterministically monostable surface reaction model [13]. However, to model the observed behavior, we need a realistic model for CO-oxidation incorporating internal noise resulting from stochastic nature of adsorption, desorption, reaction, and diffusion. The model must account for the fact that rapid CO diffusion plays an important role in quenching fluctuations [8,14], but that adspecies interactions which induce spatial ordering [15], as well bifurcation behavior, can compensate by enhancing fluctuations. Atomistic lattice-gas (LG) models have such potential, but most simulations of CO-oxidation are based upon ZGB (Ziff, Gulari, Barshad) model [16], and are unsuitable for comparison with experiments because they exhibit unrealistic oxygen-poisoning, and neglect essential processes like CO diffusion.

Thus, here we present results from Monte Carlo simulations of a refined LG model for CO-oxidation on surfaces which incorporates the following key features:

(i) CO(gas) adsorption onto single empty sites at rate p_{CO}. CO(ads) hops very rapidly to other empty sites on the surface, so it is assumed randomly distributed on sites not occupied by O(ads). CO(ads) also desorbs from the surface at rate d.

(ii) O_2(gas) adsorption dissociatively at diagonal nearest-neighbor (NN) empty sites at rate p_{O2}, provided that the additional six sites adjacent to these are not occupied by O(ads). This "8-site rule" [17] reflects the very strong NN O(ads)-O(ads) repulsions. O(ads) is also immobile and cannot desorb, so O(ads) never occupies adjacent sites.

(iii) Each adjacent pair of CO(ads) and O(ads) can react at rate k to form CO_2(gas).

Since CO(ads) is randomized, we adopt a "hybrid" approach [8]: CO(ads) is described by a single mean-field like parameter, the coverage of CO(ads), but the distribution of O(ads) is described by a full lattice-gas simulation on a square grid of adsorption sites.

Our model is still simplistic, but including infinite NN O-O repulsions introduces expected superlattice O-ordering [18], and eliminates artificial ZGB-type O-poisoning [16]. Also, O(ads) interior to c(2x2) O-domains is reactive as found in some experiments [19]; the total reaction rate is in fact given exactly by $4k\theta_{CO}\theta_O/(1-\theta_O)$. Desorption is included in the model since, although T is low in these experiments compared to single-crystal studies, the surface coverages are high (due to slower reaction), which reduces the activation barrier for desorption [20]. The model does not support oscillatory kinetics, but it is only applied to describe experimental behavior in the bistable region.

We first present simulation results for large systems, setting $p_{CO} + p_{O2} = k = 1$. The model supports bistability (i.e., a stable reactive state with low θ_{CO} coexists with a relatively inactive state with higher θ_{CO}) for sufficiently low d. The width of the bistable region decreases with increasing d, vanishing at a critical value of $d_c \approx 0.054$, which corresponds to a cusp-bifurcation. See Fig. 3a. Behavior near this bifurcation point is similar to that near a thermodynamic critical point in that the amplitudes of the RMS fluctuations in θ_{CO} and θ_O increase as d increases towards d_c (cf. Fig. 3b) Also, the fluctuations in θ_{CO} are anti-correlated with those in θ_O (i.e., when θ_{CO} increases, θ_O tends to decrease). We further find critical slowing down approaching the critical point, i.e., an increase in decay times of the time-autocorrelation functions obtained from the coverage fluctuations.

For large systems, such as single-crystal surfaces, these fluctuations are not sufficient to induce transitions between the stable steady states, i.e., one has true bistability, but such transitions are possible for small systems as seen in the experiments. Here, we show that our model for a "small" 60×60 site lattice (with periodic boundary conditions) both mimics and

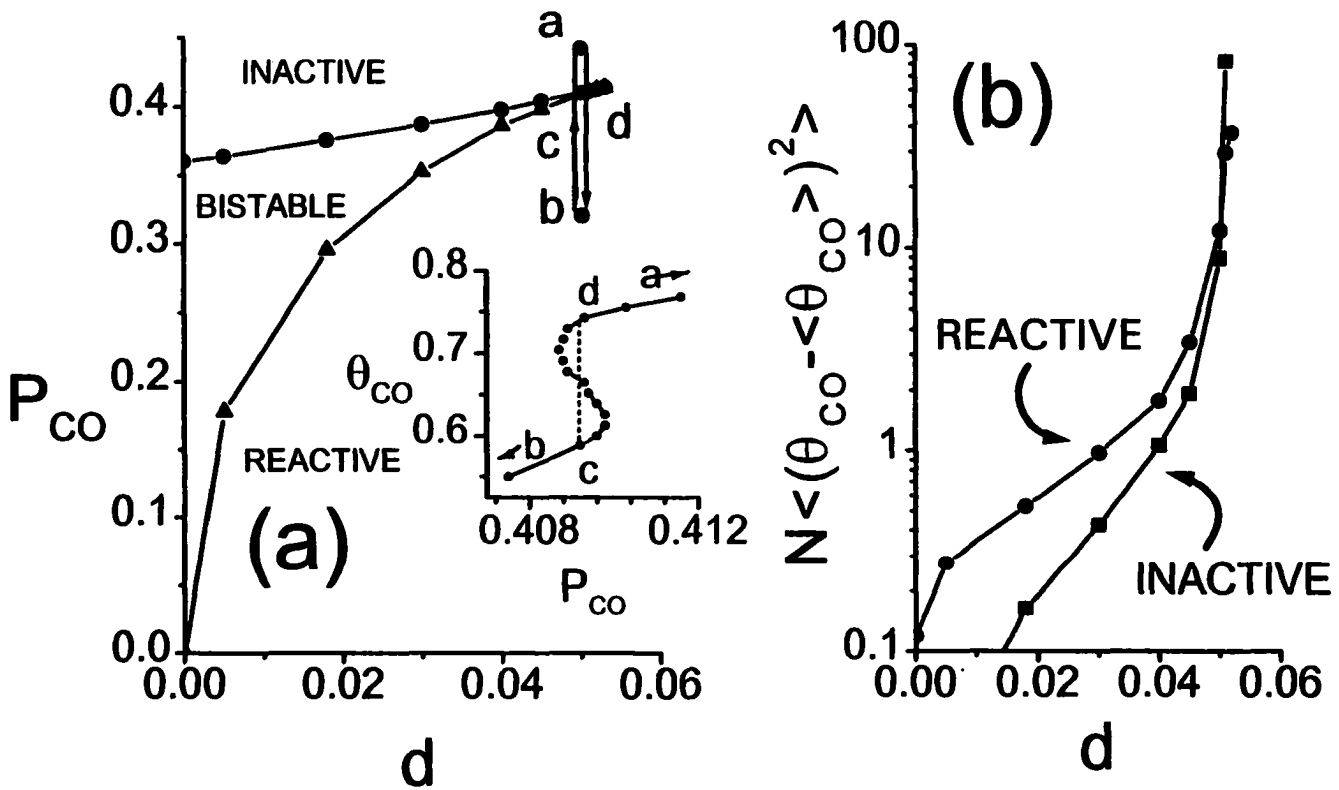

Figure 3: (a) Bifurcation or phase diagram for our reaction model showing the bistability region. The inset shows hysteresis in θ_{CO} for fixed d=0.05. In the experiment (Fig. 1c) the temperature corresponds to d. (b) Amplitude of fluctuations in θ_{CO} for the reactive and inactive branches at the midpoint of the bistability region. N denotes the system size in number of sites.

elucidates this behavior. To this end, we examine the form of the θ_{CO}-distribution in four specific states, as p_{CO} is varied cyclically through the bistable region (for fixed d). For d=0.05 ìcloseî to d_c, the distribution is monomodal in both the monostable regions, but it has a bimodal or distorted monomodal form in the middle of the bistable region (for an observation time of 3200 time units). See curves a-d in Fig.4. The former is expected. The latter indicates the occurrence of transitions between the bistable states, differences between cases (b) and (d) occurring since transitions do not occur frequently on the time scale of observation. However, for d=0.04 well below d_c, the distribution (not shown) is monomodal even in the middle of the bistable region (i.e., the system does not make transitions between the two states). All these aspects of fluctuation behavior are seen in the experiments.

Clearly, for our model, fluctuation-induced transitions between the bistable states become more likely closer to the critical point d_c, as the amplitude of the fluctuations increases (see Fig. 3b). In the middle of the bistable region, for our observation time, the transition from monomodal to bimodal distributions occurs for $d \approx 0.045$ for a 60×60 site system, but it occurs earlier for smaller systems, e.g., at d≈0.040 for a 30×30 site system. Very close to d_c, it becomes difficult resolve the bimodal distribution because the fluctuations become large, and the distinction between the two steady states diminishes.

In conclusion, we have demonstrated experimentally and theoretically that fluctuation-induced transitions can occur in a bistable surface reaction: (i) if the system is sufficiently small; and (ii) if the system is in close proximity to a critical point where bistability vanishes and fluctuations diverge. These results are important for understanding the reaction behavior of small sized (nanoscale) systems which can be found in many

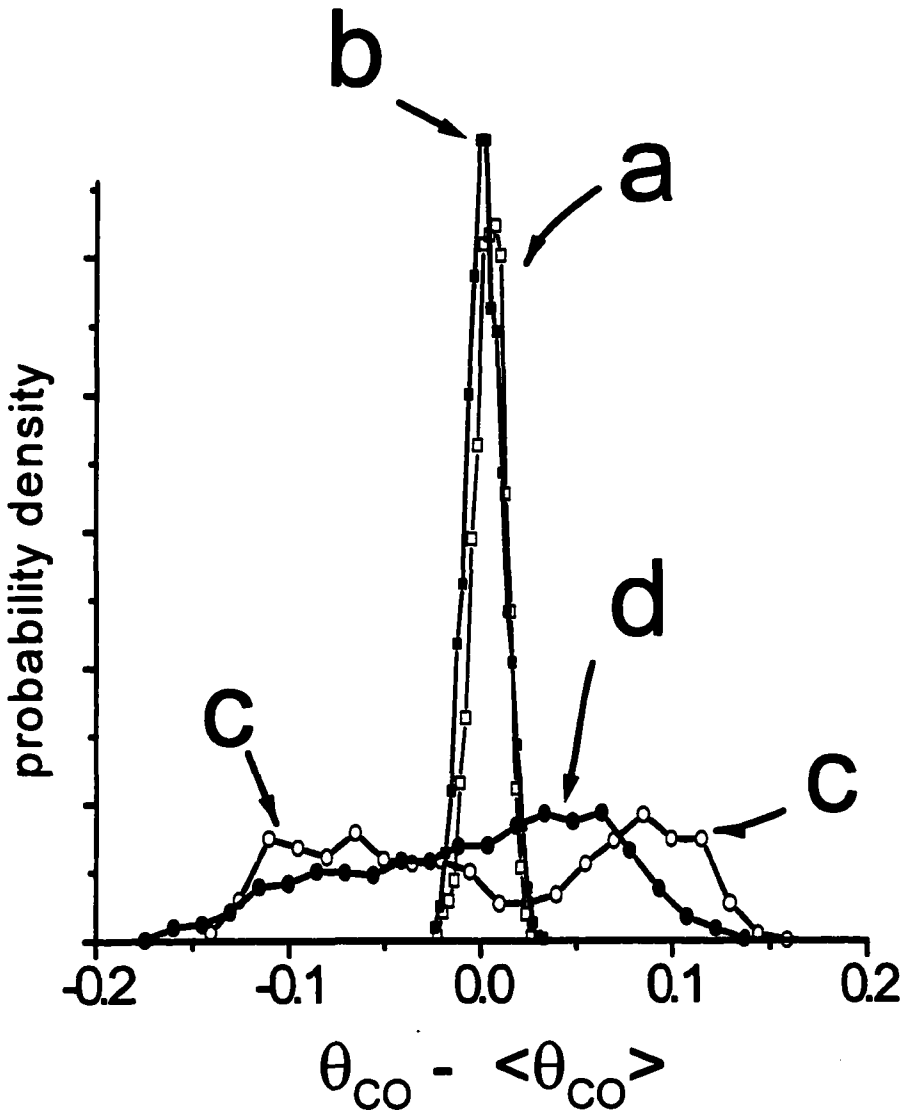

Figure 4: Probability distributions for θ_{CO} on a 60x60 lattice with d= 0.050 for points marked on the hysteresis loop in Fig.3a

different areas in chemistry and biochemistry. EWJ and JWE were supported by the Division of Chemical Sciences, USDOE, through Ames Laboratory (operated by ISU under Contract No. W-7405-Eng-82).

REFERENCES

[1] N. G. van Kampen, Stochastic processes in physics and chemistry, (North Holland, Amsterdam, 1987).

[2] W. Horsthemke, R. Lefever, Noise-induced transitions (Springer, Berlin, 1984); P. Hanggi, et al., Rev. Mod. Phys. 62, 251 (1990); A.S. Mikhailov and A. Yu. Loskutov, Foundations of synergetics II, 2nd Ed. (Springer, Berlin, 1996);

[3] M.O. Vlad and J. Ross, J. Chem. Phys. 100, 7268, 7279, 7295 (1994); A. S. Mikhailov, Z. Phys. B 41, 277 (1981).

[4] Single-molecule optical detection, imaging, and spectroscopy, T. Basche et al., Eds. (VCH, Weinheim, 1997).

[5] Yu. Suchorski, J. Beben and R. Imbihl, Surf. Sci. 405, L477 (1998).

[6] P. W. Jacobs, S. J. Wind, F. H. Ribeiro and G. A. Somorjai, Surf. Sci. 372, L249 (1997).

[7] C. N. Satterfield, Heterogeneous Catalysis in Practice (McGraw - Hill, New York, 1980).

[8] M. Tammaro, et al., J. Chem. Phys. 103, 10277 (1995); 108, 762 (1998).

[9] E.W. Müller and T.T. Tsong, Field Ion Microscopy, Elsevier, New York (1969).

[10] Yu. Suchorski, et al., Surf. Sci. 401, 392 (1998).

[11] R. Imbihl and G. Ertl, Chem. Rev. 95, 697 (1995).

[12] Yu. Suchorski, J. Beben and R. Imbihl, Prog. Surf. Sci., in press (1998).

[13] K. Fichthorn, E. Gulari, and R.M. Ziff, Phys. Rev. Lett. 63, 1527 (1989).

[14] J. W. Evans and T. R. Ray, Phys. Rev. E 50, 4302 (1994).

[15] For mixed adlayers, $<(\theta_J - <\theta_J>)^2>$ is given by the integrated spatial correlations for species J, divided by system size. Thus, increased spatial ordering implies increased fluctuations. See Appendix C in Ref. 8.

[16] R. M. Ziff, E. Gulari, and Y. Barshad, Phys. Rev. Lett. 56, 2553 (1986).

[17] C. R. Brundle, R. J. Behm, and J. A. Barker, J. Vac. Sci. Technol. A 2, 1038 (1984); S.-L. Chang and P. A. Thiel, Phys. Rev. Lett. 59, 296 (1987).

[18] The reactive state displays transition from short- to long-range c(2x2) O-order (so fluctuations diverge), as p_{CO} decreases and θ_O increases above a critical value.

[19] M. Xu, J. Liu, and F. Zaera, J. Chem. Phys. 104, 8825 (1996).

[20] R. J. Behm, et al., J. Chem. Phys. 78, 7438 (1983).

CHAPTER 5. RELAXATION EFFECTS IN RANDOM SEQUENTIAL ADSORPTION: APPLICATION TO CHEMISORPTION SYSTEMS

A paper accepted for publication in a Special Issue of: Colloids and Surfaces A: "Adhesion of Submicron Particles on Solid Surfaces", edited by V. Privman

E.W. James,[1,2] Da-Jiang Liu,[1] and J.W. Evans[1,2]

Ames Laboratory[1] and Department of Mathematics[2],

Iowa State University, Ames, Iowa 50011

ABSTRACT

We consider the effect of slow relaxation processes in two models for irreversible chemisorption which incorporate superlattice ordering of the adsorbed layer on a square lattice of adsorption sites. The first model involves adsorption of monomers onto single empty sites, and the second involves dissociative adsorption of dimers onto diagonally adjacent empty sites, where adsorption in both models occurs subject to the constraint that no adjacent pairs of occupied sites can be created. These adsorption processes produce adlayers comprised of disordered "checkerboard" or c(2×2) domains, adsorption continuing until a non-equilibrium "jammed" state is reached where no further space is available for adsorption. We focus on characterizing the evolution from this jammed state as a result of slow surface diffusion, or slow desorption (or reaction) processes. These relaxation processes open up further adsorption sites which are immediately filled in the presence of continued

adsorption. In all cases, evolution involves Lifshitz-Cahn-Allen-type coarsening of the c(2×2) domains.

Keywords: random sequential adsorption, chemisorption, diffusion, desorption, reaction, relaxation.

1. INTRODUCTION

Chemisorption onto single crystal surfaces constitutes a particularly important class of adsorption processes, which have been studied extensively using the techniques of modern ultra-high vacuum surface science [1]. The general scenario, applicable to many systems, is that molecules adsorb at a periodic array of localized adsorption sites, they diffuse or hop between nearby sites, and they can also possibly desorb from the surface. The fraction of occupied sites corresponds to the coverage, and is denoted by $\theta \leq 1$ (measured in monolayers). A simplistic, but useful heuristic rule is that the activation barrier for surface diffusion is about 20% of that for desorption. Thus, one expects a range of lower surface temperatures where desorption is inoperative, but diffusion is still active. The actual situation is complicated by presence of interactions between nearby adsorbed species (or adspecies), which strongly influence both diffusion and desorption, and which control the equilibrium structure of the adsorbed layer (or adlayer). Statistical mechanical lattice-gas models, together with the associated sophisticated concepts and techniques, have been applied to study not just phase transitions in equilibrated chemisorbed adlayers [2], but also to characterize the dynamics of adlayer equilibration (typically at constant coverage in the absence of desorption) [3]. In addition, there has been considerable analysis of both the

adsorption kinetics [4,5], and of the kinetics of desorption (the latter typically from equilibrated adlayers at higher temperatures) [6].

One important feature of chemisorption systems, which is of central relevance to this study, is that often an "ensemble" of more than one empty site is required for adsorption [1,5,7]. This constraint could reflect simple steric (i.e., size) effects, or indicate the presence of effectively infinite short-range repulsions between adspecies. Such interactions often produce so called superlattice ordering in the equilibrium (and non-equilibrium) states of the adlayer [2]. Here, we have adopted the surface chemistry terminology "superlattice ordering", which means that adspecies assume a locally periodic arrangement with unit cell larger than that of the underlying lattice of adsorption sites. In the extreme situation of very low temperature, where adsorbed species are immobile, it is clear that the adsorption process will continue until there are no further available ensembles of (more than one) empty site. At this point, the adlayer will remain indefinitely in a non-equilibrium "jammed" state with coverage $\theta_J<\theta_{max}$ [5,8], where θ_{max} is the maximum possible adlayer coverage subject to the constraints imposed by any infinite repulsive interactions.

These types of far-from-equilibrium adsorption processes have been analyzed extensively as part of a collection of problems referred to as of "Random Sequential Adsorption" (RSA). Usually, the focus of these studies is on very large lattices where edge effects are negligible [5,8]. The first such studies go back to the 1930's where J.K. Roberts considered the irreversible random adsorption of diatomic molecules (oxygen, nitrogen, etc.) or "dimers" on nearest-neighbor (NN) empty sites of a square lattice [9]. In Robert's model, the jammed state consists of a distribution of isolated empty sites (each of which has no empty neighbors) with $\theta_J=0.906823$ [5,10], which should be compared with $\theta_{max}=1$.

Recently, attention has turned to a "canonical" model for RSA of monomers at single empty sites on a square lattice with NN exclusion. We shall also consider a similar "eight-site model" for RSA of dimers at diagonal or next NN empty sites on a square lattice, also with NN exclusion [5]. Both models exhibit checkerboard or c(2×2) superlattice ordering, where $\theta_{max}=1/2$. Sophisticated analyses of both the adsorption kinetics and jammed state structure for such models have been developed utilizing approximate truncation of exact hierarchical rate equations, formal expansion techniques, and (kinetic) Monte Carlo simulations [5,8].

Recently, there has been some interest modifying these RSA models to incorporate "relaxation" due to diffusion or desorption processes, and in characterizing the resultant evolution of the (near) jammed adlayer [11]. In this paper, we will focus somewhat narrowly on such relaxation processes in the regime where rates for relaxation are far below rates for adsorption, i.e., an "adiabatic limit" for relaxation. In Sec.2, we discuss in more detail the two RSA models with NN exclusion on a square lattice, mentioned above, as these will be utilized in this work. We also review recent work on RSA models with relaxation, and motivate the relaxation mechanisms chosen here. In Sec.3, we consider diffusional relaxation for both RSA models, where diffusion involves hopping of adspecies to adjacent empty sites subject to the constraint that no NN pairs of occupied sites can be formed. In Sec.4, we consider relaxation induced by random desorption of monomers, which could be regarded either as simple non-reactive desorption, or desorption induced by reaction with a coadsorbed species not incorporated explicitly into the model. In both cases, we characterize in detail adlayer evolution during relaxation, which involves coarsening, and make some natural

comparisons between behavior for the different relaxation mechanisms. A brief summary is presented in Sec.5, and a brief discussion of analogous processes on linear lattices is presented in the Appendix.

2. BACKGROUND ON RSA MODELS AND RELAXATION PROCESSES

2.1 RSA MODELS WITH SUPERLATTICE ORDERING OF THE ADLAYER

As noted above, unlike Robert's model [9], more recent RSA studies have focused on models which exclude the occupancy of nearby sites, and thus induce superlattice ordering of the adlayer [5]. This feature more realistically describes a number of chemisorption systems, where one has (effectively) infinite repulsive interactions between nearby chemisorbed species. In this work, we consider only models with exclusion of NN occupancy on a square lattice of adsorption sites. Below, the lattice constant is set to unity. This constraint induces "checkerboard" or c(2×2) superlattice ordering [1] with $\theta_{max}=1/2$. The c(2×2) domains have a "degeneracy" of two, with adspecies in domains of different phase residing on one of two interpenetrating "sublattices". (The latter terminology is adopted from statistical mechanics, although it is potentially confusing here as adspecies populating a single sublattice exhibit superlattice ordering!) Adjacent c(2×2) domains of different phase are separated by "domain boundaries". For completeness, we note that the equilibrium state of an adlayer with infinite NN repulsions on a square lattice is described by the so called hard-square model, which undergoes a transition from short-range order to long-range c(2×2) order above a critical coverage of 0.367743 [12,13]. Below, we find it convenient to borrow the standard schematic representation used for the hard-square model which replaces "circular adspecies" by "hard-squares" which are diamonds with side length $\sqrt{2}$ times the surface lattice constant. This

representation will be used in subsequent sections showing snapshots of adlayer configurations generated by simulations, where diamonds of one phase will be shaded black, and those of the other will be shaded gray.

In the simplest canonical model for RSA with NN exclusion, irreversible random adsorption of monomers occurs at single empty sites on a square lattice, provided all four neighbors are empty [5]. Thus, an ensemble with a total of five empty sites is required for adsorption. See Fig.1a. This model, which is often simply called RSA with NN exclusion, was first applied to describe the adsorption of H_2O on Fe(100) [14], although the actual process is likely more complicated. However, the model should reasonably apply to describe low temperature adsorption onto single sites of molecules with strong NN repulsions and negligible longer range interactions. Adsorption of Cl on Ag(100) provides such an example [13]. Next, we characterize in some detail the jammed state for this model. Analytic approximation was first used to determine that $\theta_J \approx 0.364$ [15], which is well below $\theta_{max}=½$ for perfect c(2×2) ordering. Recent more sophisticated studies have used formal expansion methods, resummation, and simulation to determine more accurately $\theta_J \approx 0.364132$ [5,10]. The jammed state consists of c(2×2) domains which are completely free of internal defects, and separated only by domain boundaries. Using the schematic representation of the hard-square model, domain boundaries are entirely composed of diagonal uncovered strips of width $1/\sqrt{2}$, and of various lengths $n\sqrt{2}$, where $n \geq 1$. See Fig.1b. (What would be identified as a horizontal or vertical portion of domain boundary in a schematic with circular adspecies becomes a zig-zag stretch of segments of diagonal domain boundary each of length $\sqrt{2}$,

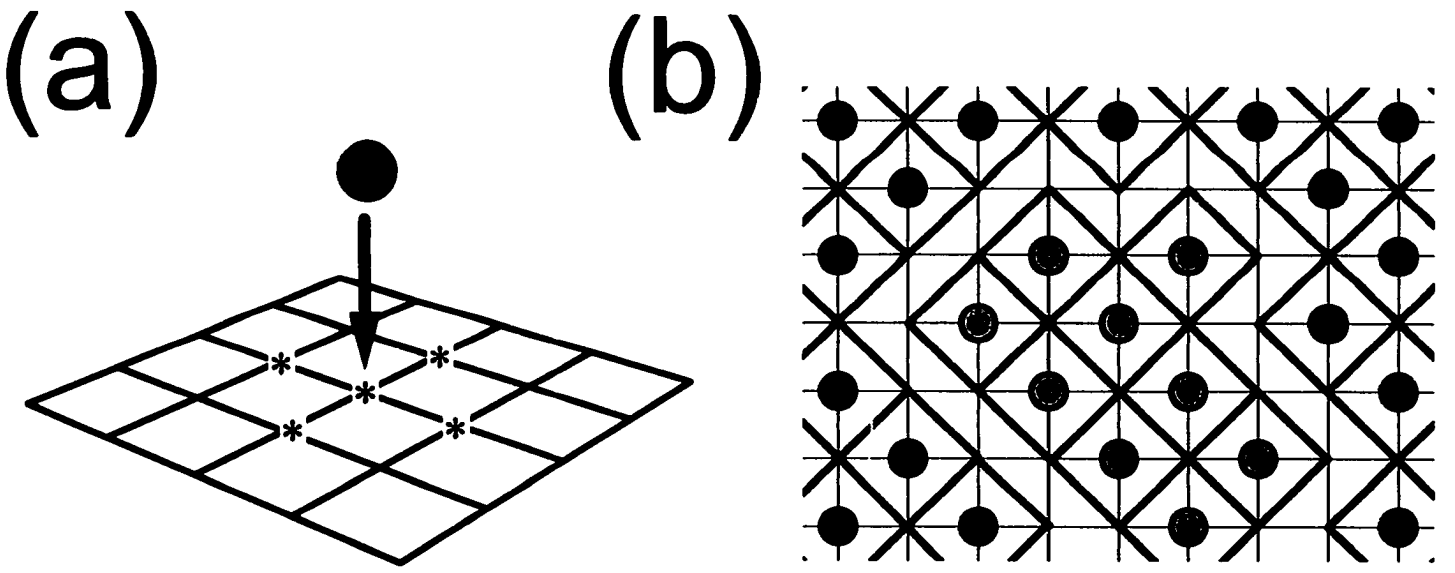

Figure 1. RSA of monomers with NN exclusion. Schematic of: (a) the adsorption rule, where the * indicate the ensemble of five empty adsorption sites; (b) the jammed state structure, where adspecies in c(2×2) domains of different phase are denoted by black and gray circles. The corresponding diamonds in the hard-square representation are also shown

alternating between the two possible orientations.) Further characterization of the geometry of c(2×2) domains in the jammed state is also available [16].

A similar RSA model with NN exclusion is the so called eight-site model. This model describes the dissociative adsorption of diatomics (or dimers) onto diagonal NN empty sites on a square lattice, subject to the constraint that the additional six neighboring sites are also empty [17]. Thus, an ensemble with a total of eight empty sites is required for adsorption. See Fig.2a. This model was first proposed to describe the dissociative adsorption of O_2 on Ni(100) [17]. Subsequently, it was found to provide a useful description of the short-range c(2×2) ordering observed upon deposition of O_2 on Pd(100) at low temperatures and "higher" pressures [18-20]. Next, we characterize the jammed state for this model. From simulations, we find that $\theta_J \approx 0.36157$ (cf. Ref. [20]), quite close to the value for the canonical model. In contrast to the canonical model, individual c(2×2) domains in the jammed state now contain (isolated) internal defects, which we define precisely as unoccupied sites surrounded by four diagonally adjacent occupied sites. In the hard-square representation, these appear as isolated uncovered diamonds surrounded by all four occupied diagonal neighboring diamonds. The density of these is $D \approx 0.00984$. Domain boundaries are also modified from the simple structure described above for the canonical RSA model, now being "decorated" by isolated "external" defects. See Fig.2b. Further characterization of the c(2×2) domain geometry can be found in Ref.[16].

Finally, we comment on the similarity in θ_J-values for the two models. Since each adsorption event in the eight-site model guarantees that two adspecies will be in the same c(2×2) domain. This results in larger domains than in the canonical model [16]. This feature

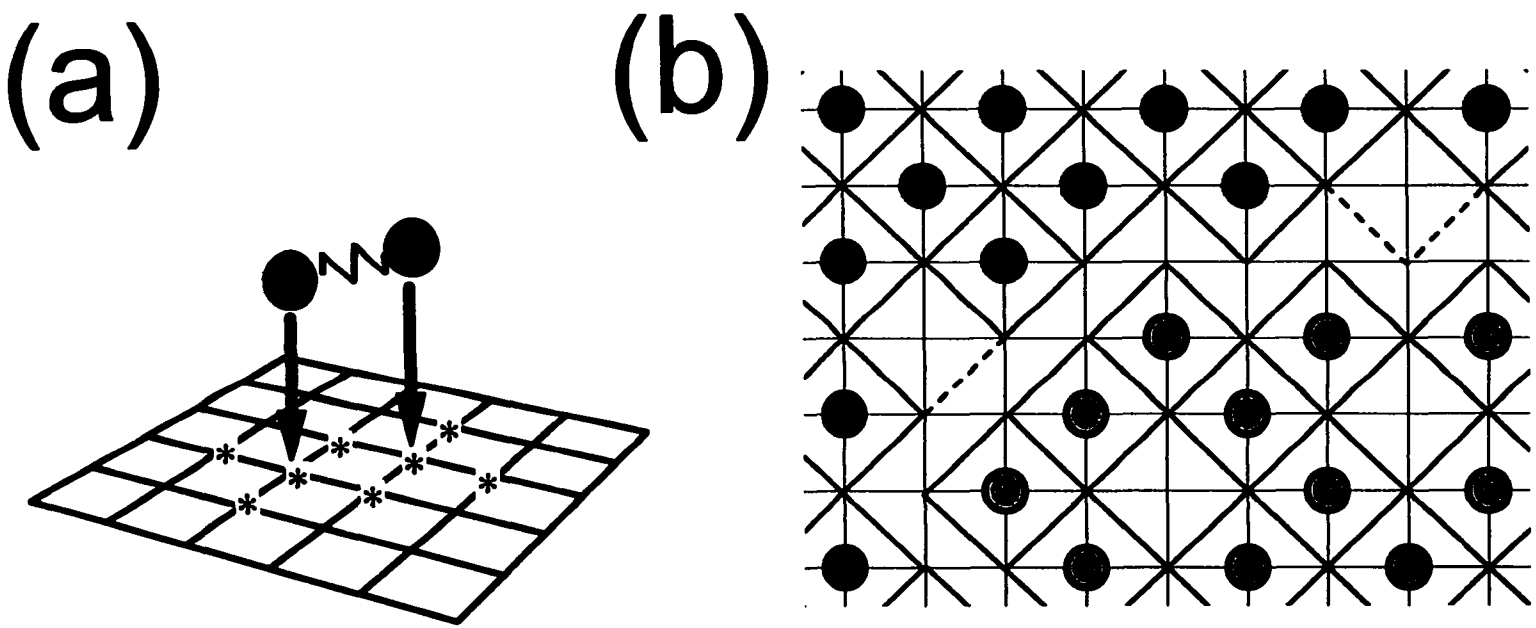

Figure 2. Eight-site model for RSA of dimers. Schematic of: (a) the adsorption rule, where the * indicate the ensemble of eight empty adsorption sites; (b) the jammed state structure, using the format of Fig.1. Note the two internal defects in the lower c(2×2) domain, and the two external defects (indicated by dashed lines) decorating the domain boundary.

tends to increase θ_J. However, the counterbalancing effect is that c(2×2) domains in the jammed state of the eight-site model contain internal defects, and domain boundaries are now decorated by external defects, which tends to lower θ_J. The net result is a slightly lower θ_J than in the canonical model.

2.2 RELAXATION MECHANISMS

The assumption in standard RSA models of negligible desorption should often be well satisfied in chemisorption systems at lower temperatures. In contrast, the assumption that chemisorbed molecules are immobile is an idealization, which should be scrutinized. In fact, even if chemisorbed species are effectively immobile on the typical shorter time-scale of adsorption, mobility is likely significant over longer times. Thus, it is natural to examine the influence of some degree of surface mobility or diffusion on Random Sequential Adsorption processes. For the models described above, one naturally allows single atoms to hop (one at a time) to adjacent empty sites, provided no neighboring pairs of occupied sites are thus created. Recent efforts along these lines were pioneered by Privman and coworkers [11], who considered the effect of diffusional relaxation for a number of simple RSA models. These models included RSA of dimers on adjacent sites of a linear lattice (where the dimers did not dissociated, and thus diffused intact) [21], RSA of monomers with NN exclusion on a square lattice [22], and a model equivalent to RSA of monomers with NN and diagonal NN exclusion on a square lattice [23]. In their work, a non-zero (but typically small) ratio for diffusional hopping to adsorption rates was specified. Then, initially, adsorption proceeds roughly as for RSA without mobility, thus creating a near-jammed state. Subsequently, the near-jammed state evolves due to diffusional relaxation to allow further adsorption and an

increase in the coverage towards some ideal upper limit for perfect ordering. For models with superlattice ordering, coarsening of the degenerate domains was observed to occur during this process, and the dynamic scaling laws were ascertained [11].

We have noted above that (non-reactive) desorption is not expected to be operative in a regime where chemisorbed species are effectively immobile. However, it is possible that desorption mediated by reaction with a second coadsorbed species could occur in this regime. A classic example is removal of relatively immobile adsorbed oxygen by reaction with highly mobile coadsorbed CO, i.e., catalytic CO-oxidation on surfaces [24]. To be more specific, consider behavior where one starts with an empty surface, which is then exposed both to O_2, which adsorbs according to the eight-site rule, and to CO, which adsorbs onto single empty sites. Furthermore, suppose that the partial pressure of O_2 is far higher than that for CO, so then, initially, one has effectively RSA of oxygen to form an immobile adlayer in a near-jammed state. Subsequently, CO adsorption at a lower rate produces a low concentration of highly mobile adsorbed CO, which react with and remove adsorbed oxygen. This potentially opens up more ensembles of empty sites for oxygen adsorption, which then likely occurs before adsorption of CO due to the higher partial pressure of O_2. This overall process leads to evolution or relaxation of the near jammed state of the oxygen adlayer, effectively as if the adsorbed oxygen were being slowly removed by non-reactive desorption [25].

The coarsening behavior which occurs during this relaxation process was recently quantified in a lattice-gas reaction model for CO-oxidation incorporating the above adsorption rules, where adsorbed oxygen is immobile, and adsorbed CO is treated as infinitely mobile [25,26]. Thus, adsorbed CO forms a uniform and randomized adlayer

(neglecting CO-CO and CO-O interactions). This leads to the random removal of adsorbed O by reaction (at some finite rate) with adjacent adsorbed CO. Another recent study considered a CO-oxidation model also with the eight-site adsorption rule for oxygen, but which incorporated non-random removal of adsorbed O due to "instantaneous reaction" upon first contact with rapidly diffusing CO (which necessarily forms a very dilute, mobile adlayer) [27].

2.3 RSA WITH VERY SLOW RELAXATION

In this study, we shall consider the effect of relaxation via either diffusion or desorption for the two RSA models described in Sec.2.1, but only in the regime where rates for processes leading to relaxation are far smaller than the adsorption rate. (It seems natural to provide a detailed analysis of this limiting case as a benchmark for the more general case where the ratio of relaxation to adsorption rates is not vanishingly small. However, we do expect that these two cases exhibit qualitatively similar behavior. This can be confirmed by comparing our results below with those in Ref.[11].) In the limiting regime, the overall adsorption process occurs in two distinct stages: (i) rapid formation of the jammed RSA state; and (ii) slow relaxation from this state, which we shall see involves a coarsening process and further adsorption. More specifically, in stage (ii), after each relaxation event, one checks to determine if further adsorption is possible, and if so performs such adsorption before allowing subsequent relaxation. Thus, the adlayer always remains in a jammed state during this evolution. As indicated above, it is natural to define "internal defects" as empty sites, which are surrounded by four diagonal occupied sites, and to denote their density by D. Thus D is identically zero for relaxation in the canonical RSA model, but not in the eight-site

model. In the hard square representation, the uncovered surface not associated with internal defects corresponds to domain boundary. Thus, for both models, the total fractional area of domain boundary is given by

$$F=1-2D-2\theta. \qquad (1)$$

This quantity will decrease during coarsening.

For an infinite system, the quantities θ, D, and thus F, are "self-averaged" (and thus uniquely defined) in a single realization of the initial state and subsequent relaxation process. For finite systems (with periodic boundary conditions), these quantities should be interpreted as ensemble averages over many realizations. However, since spatial correlations in RSA processes have a very short range, fluctuations in the initial values are small for large lattices. Of course, fluctuations in F grow as this quantity decreases during coarsening, but still a single realization of the relaxation process on a very large lattice is typically sufficient to assess scaling.

3. DIFFUSIONAL RELAXATION

Here, we examine evolution or relaxation from jammed states of the canonical and eight-site RSA models on a square lattice induced by hopping of single adsorbed species (one at a time) to adjacent empty sites, subject to the constraint that no NN occupied pairs are formed. (Since in the eight-site model, dimer adsorption is dissociative, single adatoms rather dimers hop.) As noted in Sec.2.3, after each hop, one immediately checks for and if possible implements further adsorption. First, we make some general observations regarding the local

processes associated with such evolution. Clearly, adspecies interior to perfect c(2×2) domains are immobile or "frozen". Examination of Fig.2 shows that adspecies adjacent to internal defects are also frozen, so the internal defects themselves are frozen. Furthermore, from Fig.1 or Fig.2, adspecies along perfect diagonal portions of domain boundary are frozen as well. Thus, only rather restricted motion of certain other adspecies adjacent to domain boundaries is possible. However, it is this motion which leads to wandering of the domain boundaries and to subsequent coarsening.

3.1 RSA OF MONOMERS WITH NN EXCLUSION

During evolution under diffusional relaxation, the jammed state of the adlayer retains the same characteristics as the "initial" jammed state created by RSA, which was described in Sec.2.1. Thus, the surface remains completely covered by perfect defect-free c(2×2) domains, except for domain boundaries which are composed of diagonal uncovered strips of width $1/\sqrt{2}$ (using the hard-square representation). See Fig.1b. The only adspecies which can hop are those at the inside corners of the domain boundaries at bends between the two possible orientations. These adspecies hop horizontally or vertically, crossing over to a domain of the opposite phase. Further sites are made available for adsorption as follows. Consider a curved portion of the domain boundary bordered by two bends in the same direction. Then, adspecies can hop from the inside to the outside, opening up sites for adsorption, and resulting in displacement and shortening of the domain boundary. See Fig.3. This scenario was identified by Privman [11] for the canonical model with a non-vanishing ratio of hopping to adsorption rates. We emphasize that this shortening process is more

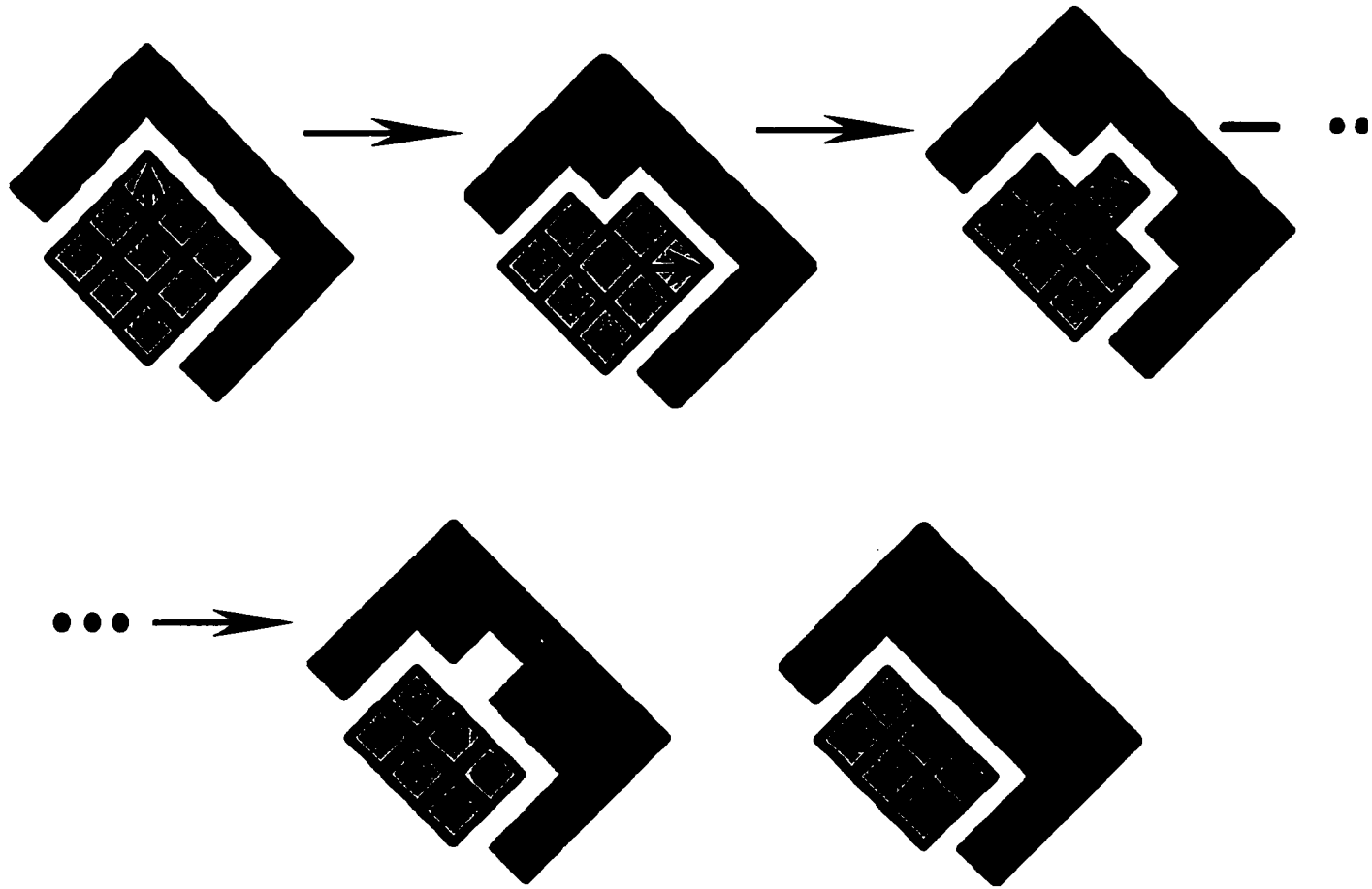

Figure 3. Schematic (using the hard-square representation) of the steps involved in the shrinking of a curved portion of domain boundary for diffusional relaxation in RSA of monomers with NN exclusion. Arrows indicate diffusive hops of adspecies.

efficient (requiring less adspecies hops), and thus should occur with a higher mean velocity, for larger domain boundary curvatures.

For finite lattices of 2L×2L sites with periodic boundary conditions, the system "almost always" evolves to a single c(2×2) domain with coverage of ½. The reason for the caveat is that for L≥3, there is a finite probability to reach a frozen configuration with a diagonal stripe of one phase imbedded in a domain of the other phase, so the ensemble average of the final coverage should be slightly below ½. However, for large L, this anomalous outcome can presumably be neglected, so as a result of coarsening, the coverage should approach ½, and the fractional area of domain boundary, $F=1-2\theta$, should vanish. With this in mind, we next present simulation results for a large system. Fig.4 shows simulated configurations for a portion of the initial jammed state, and for subsequent large-scale coarsened configurations on a 1024×1024 lattice. These simulations reveal the scaling behavior

$$F=1-2\theta \sim t^{-\alpha}, \text{ for large } t, \text{ where } \alpha=0.49, \qquad (2)$$

suggesting an asymptotic value of $\alpha=1/2$. See Fig.5. Analogous behavior was found in Ref.[22] for a non-vanishing ratio of hopping to adsorption rates. Of course, this behavior corresponds to an increase in the typical linear dimension (or chord length) of domains like $t^{1/2}$. This in turn suggests that behavior is analogous to Lifshitz-Cahn-Allen (LCA) coarsening in Hamiltonian systems [28], where domain boundary motion is driven by

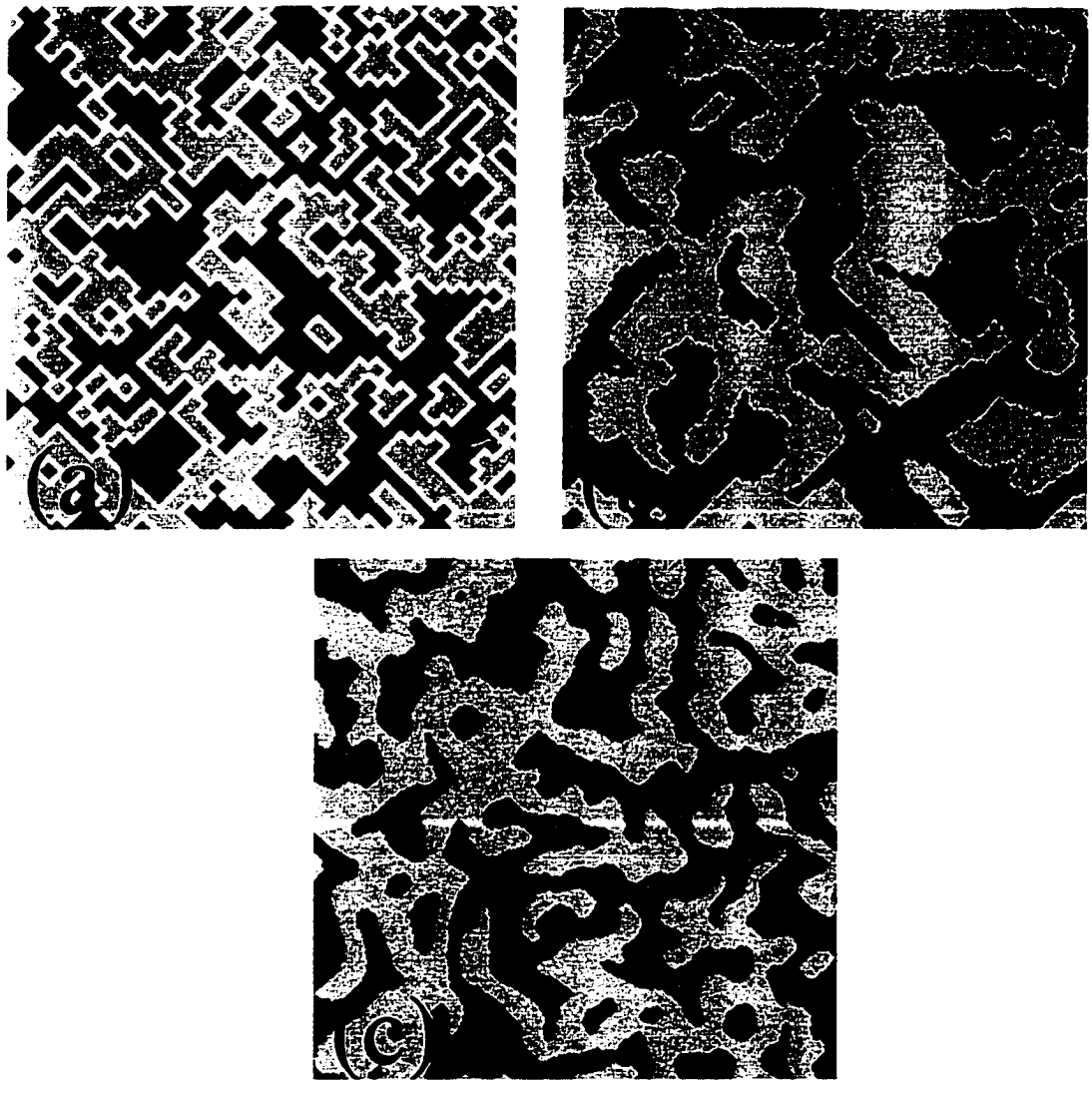

Figure 4. Snapshots of configurations during coarsening via diffusional relaxation for RSA of monomers with NN exclusion: (a) 64×64 lattice at t=0; (b) 256×256 lattice at t=100; (c) 1024×1024 lattice at t=1000.

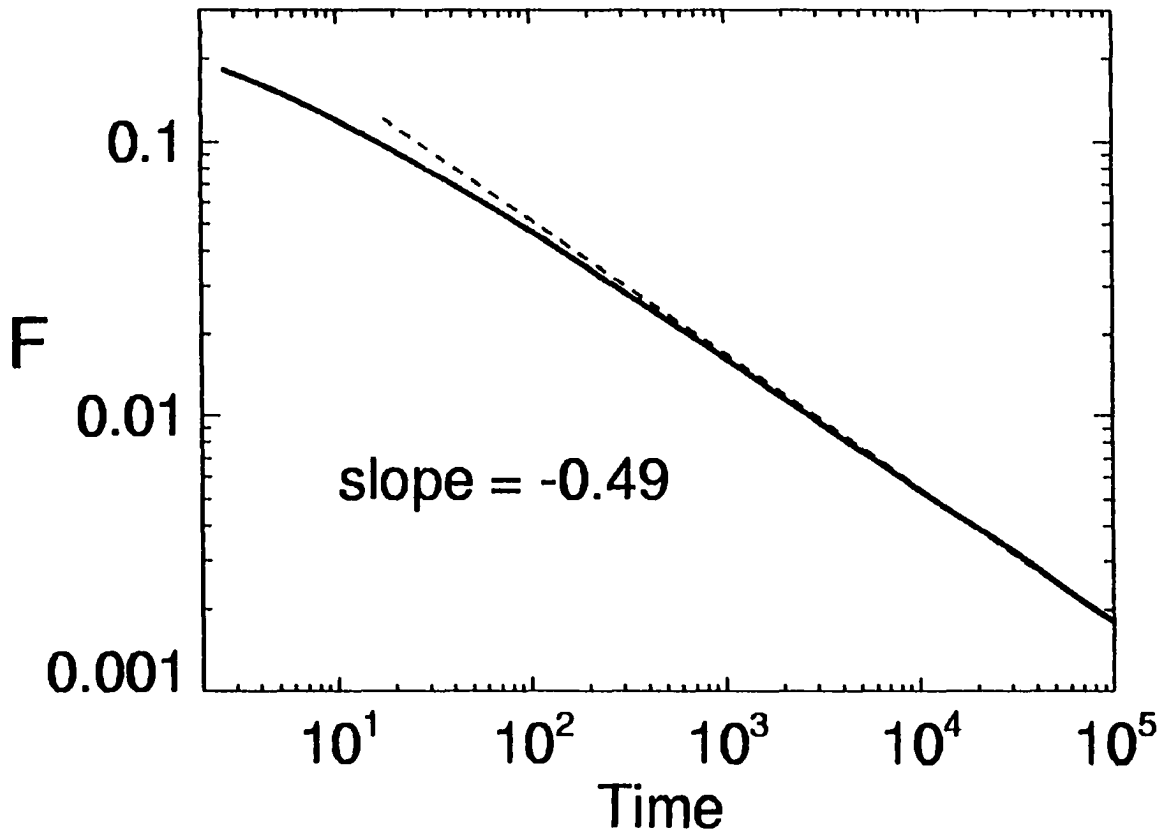

Figure 5. Log-log plot of the decrease of the fractional area of domain boundary, F, with time for diffusional relaxation in RSA of monomers with NN exclusion.

curvature. Indeed, this should be expected from the above characterization of the local processes leading to shortening of domain boundaries.

A natural and standard test for LCA-type behavior is to consider the evolution of a large near-circular domain of one phase embedded in an "infinite" region of the second phase (see Fig.6). Domain boundary propagation at a normal velocity proportional to the curvature implies that the area, A, of the embedded domain or "island" should decrease linearly with time. Indeed, the results for A versus t shown in Fig.7 demonstrate that this relation is very well satisfied. Finally, we note that it is natural to compare this behavior in the RSA model incorporating diffusional relaxation with that for the hard-square model incorporating the same diffusion process (but with no adsorption). We find that the rate of decay of area in the RSA model is about twice that in the hard-square model. This is not surprising since it is clear from the above discussion that the adsorption process enhances the bias toward shortening of domain boundaries. More specifically, evolution through the sequence of configurations shown in Fig.3 is irreversible, the last adsorbed diamond providing the "lock-piece" preventing the reverse evolution. A more detailed comparison between relaxation with and without adsorption will be presented elsewhere.

3.2 EIGHT-SITE MODEL FOR RSA OF DIMERS WITH NN EXCLUSION

During evolution under diffusional relaxation, the jammed state of the adlayer again retains the characteristics of the "initial" jammed state created by RSA, as described in Sec.2.1. Thus, the c(2×2) domains now include frozen internal defects, and domain boundaries are composed of diagonal strips of width $1/\sqrt{2}$, but decorated by isolated external defects. See Fig.2b. Now, mobile adspecies include not just those at the corners of domain

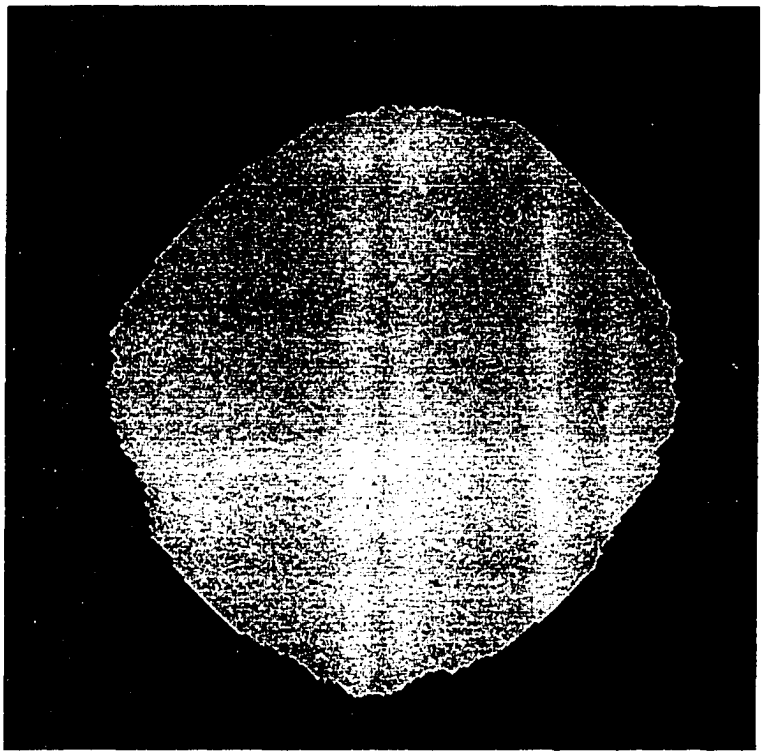

Figure 6. Configuration of a shrinking near-circular c(2×2) domain embedded in a domain of the opposite phase for diffusional relaxation in RSA of monomers with NN exclusion. The initial diameter was about 820 lattice spacing, compared with about 390 for the configuration shown which has a 512×512 field of view.

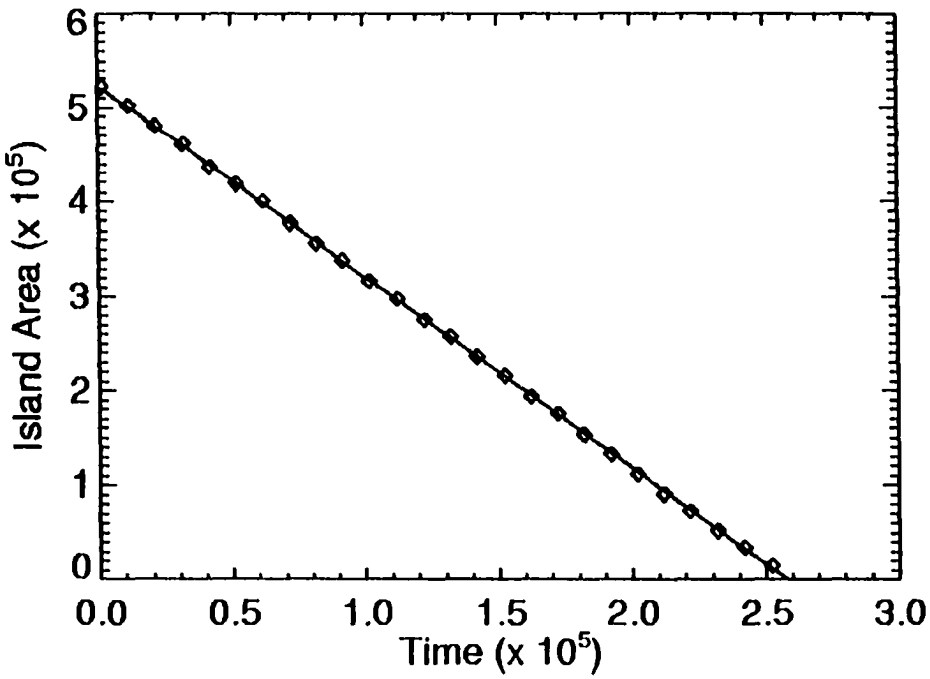

Figure 7. Linear decrease with time, t, of the area of the embedded domain or "island" shown in Fig.6 for diffusional relaxation in RSA of monomers with NN exclusion.

boundaries (as in the monomer model of Sec.3.1), but also adspecies along domain boundaries adjacent to external defects. Further sites are made available for adsorption by the type of sequences of events at curved portions of domain boundaries shown in Fig.8. As in the monomer model, this leads to a shortening of such portions of domain boundaries (with greater efficiency for larger curvatures). Note also that evolution through the sequence of configurations shown in Fig.8 is irreversible, adsorption providing the "lock-piece" preventing reversal.

For finite lattices of 2L×2L sites with periodic boundary conditions, the system "almost always" evolves to a single c(2×2) domain, but unlike the monomer model, this domain includes a finite density of frozen isolated defects, $D_\infty(L)>0$. As in the monomer model, anomalous states with frozen domain boundaries are possible. However, again this outcome can presumably be neglected for large L, and then the fractional area of domain boundary, $F=1-2D-2\theta$, should vanish. However, the coverage, $\theta_F(L) = \frac{1}{2}-D_\infty(L)$, in the final frozen state remains below ½. Interestingly, we find that $D_\infty(L)$ apparently vanishes (like $L^{-1/2}$), as $L\to\infty$. This reflects the feature that in larger systems, domain boundaries tend to sweep by a given location on the surface many times. Each sweep allows some movement of defects, which ultimately leads to a reduction in the defect density. A more detailed discussion and analysis of this subtle phenomenon will be presented separately [29].

Next, we present simulation results for a large system. Fig.9 shows simulated large-scale coarsened configurations on a 1024×1024 lattice. These simulations reveal the scaling behavior (see Fig.10)

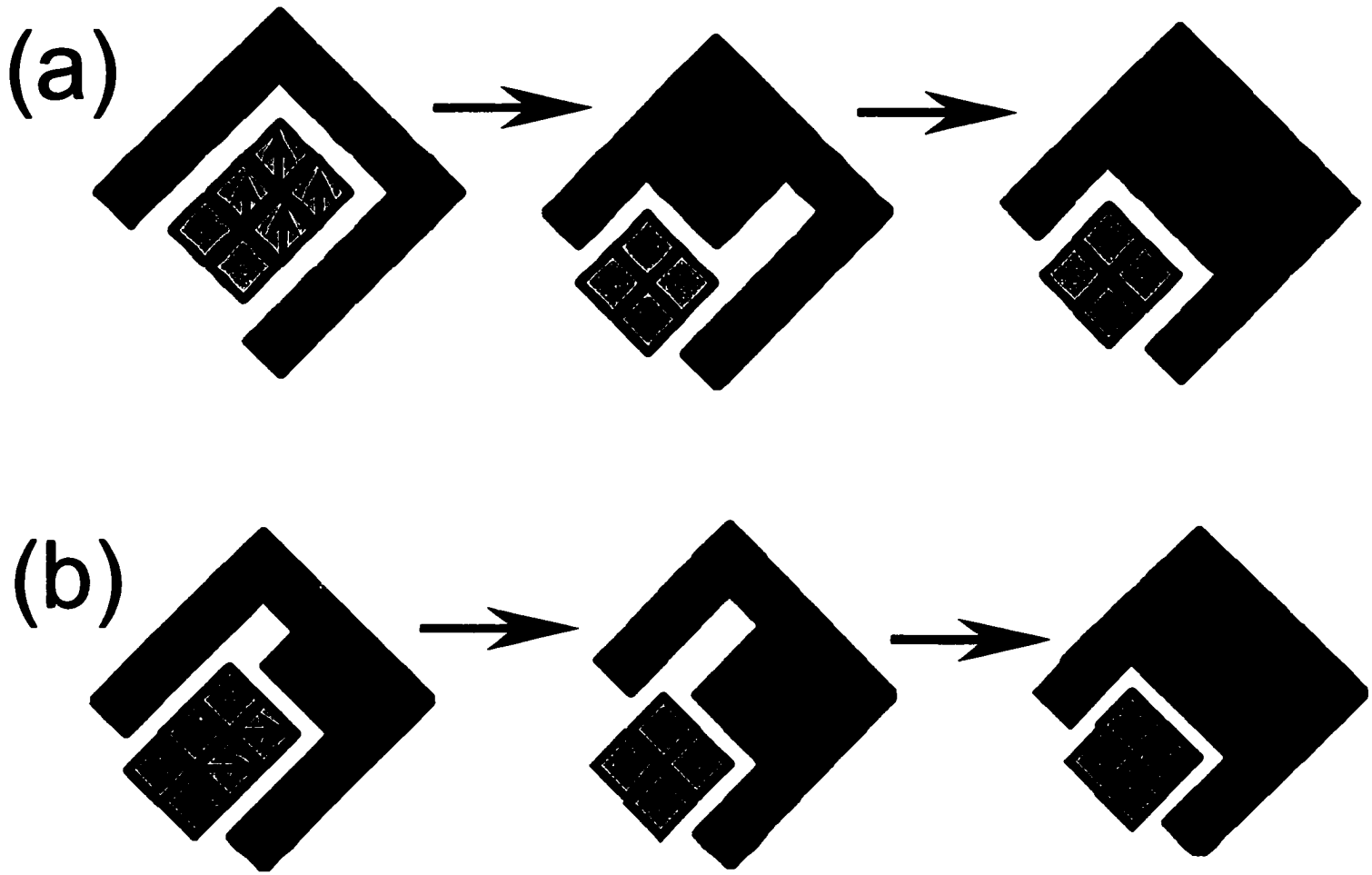

Figure 8. Schematic (using the hard-square representation) of the steps involved in shrinking of curved portion of domain boundary for diffusional relaxation in the eight-site model for RSA of dimers. Example (a) involves four consecutive diffusive hops (indicated by arrows), followed by one dimer deposition event. Example (b) involves two consecutive diffusive hops, followed by one dimer deposition event.

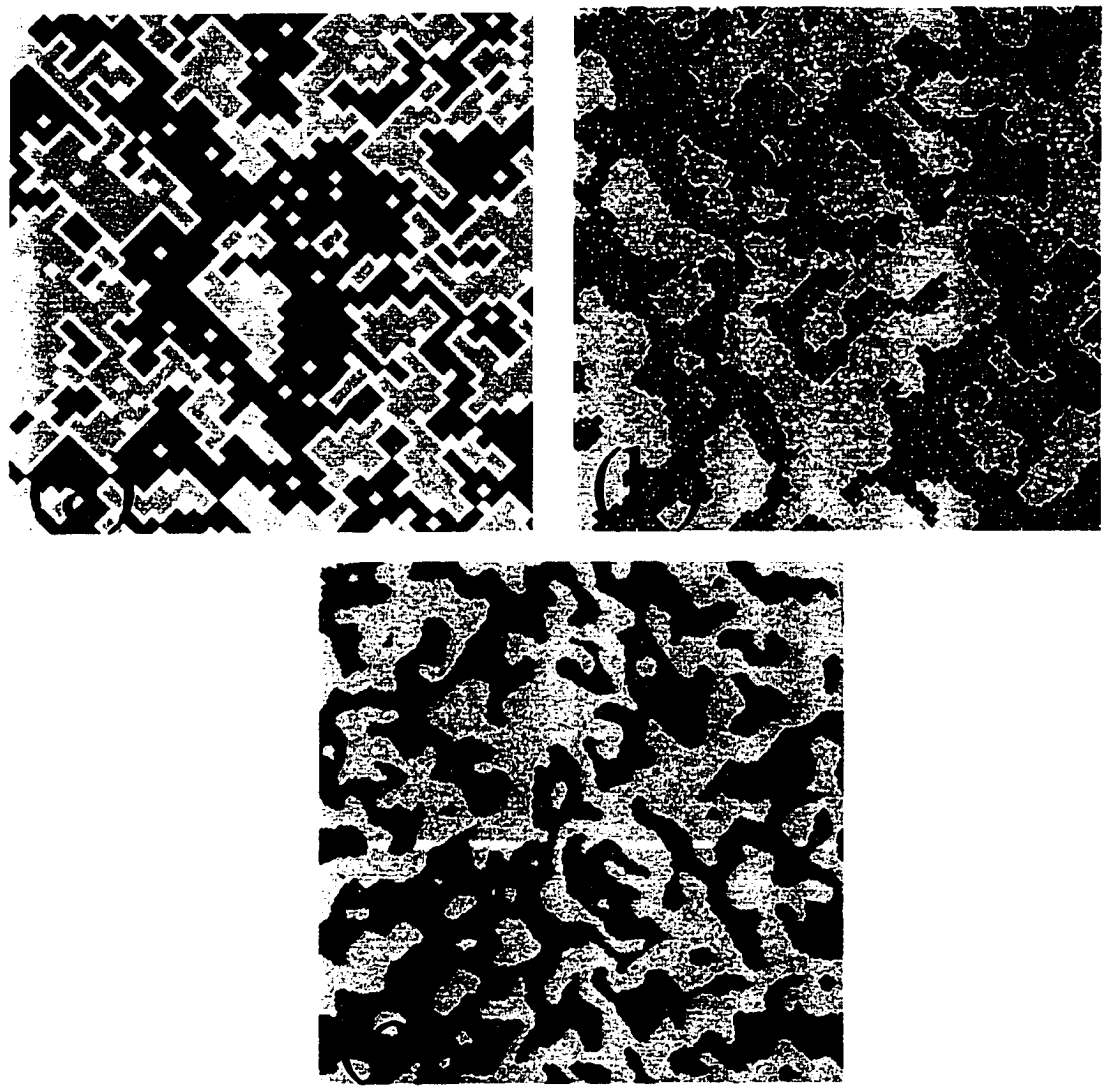

Figure 9. Snapshots of configurations during coarsening via diffusional relaxation in the eight-site model for RSA of dimers: (a) 64×64 lattice at t=0; (b) 256×256 lattice at t=100; (c) 1024×1024 lattice at t=1000.

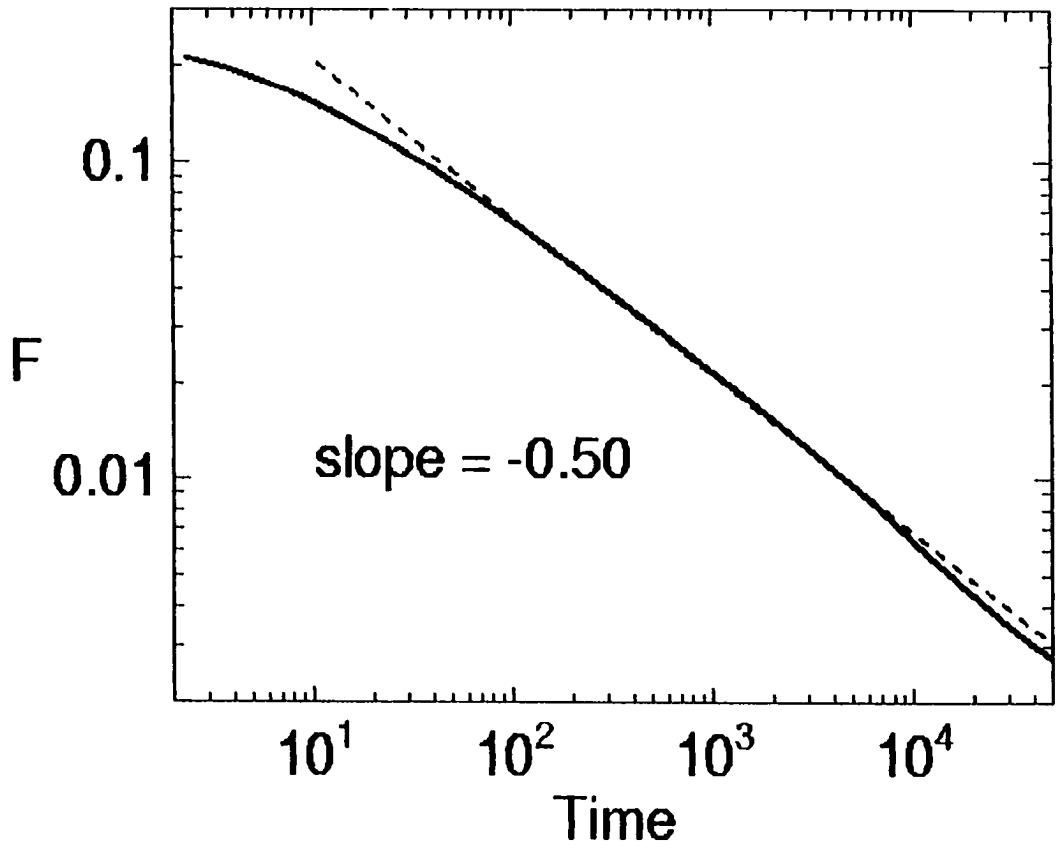

Figure 10. Log-log plot of the decrease of F with time for diffusional relaxation in the eight-site model for RSA of dimers with NN exclusion.

$$F=1-2D-2\theta \sim t^{-\alpha}, \text{ for large t, where } \alpha \approx 0.50, \quad (3)$$

again suggesting an asymptotic value of $\alpha=1/2$. As for the model in Sec.3.1, this behavior reflects an increase in the typical linear dimension of domains like $t^{1/2}$, again suggests the expected Lifshitz-Cahn-Allen (LCA) type coarsening.

4. RELAXATION DUE TO DESORPTION (OR REACTION)

Here, we examine evolution or relaxation from jammed states of the canonical and eight-site RSA models on a square lattice induced by slow random removal of adsorbed species where, after each removal event, one immediately checks for and if possible implements further adsorption.

4.1 RSA OF MONOMERS WITH NN EXCLUSION

At first glance, relaxation by removal in this RSA model appears quite different from relaxation by diffusion (Sec.3.1), since all adspecies interior to c(2×2) domains, as well as those along domain boundaries, can be removed. However, if an interior adspecies is removed, then it is immediately replaced (before any subsequent diffusion) by another in the same location due to rapid adsorption. Furthermore, the same applies for adspecies along domain boundaries, except for those at corners (in the hard-square representation). If an adspecies at such a corner is removed, then with equal probability, it is replaced with another in the same location, or by one across the domain boundary. Thus, it is clear that this model has effectively equivalent dynamics to that in Sec.3.1 with diffusional relaxation.

4.2 EIGHT-SITE MODEL FOR RSA OF DIMERS WITH NN EXCLUSION

For adsorption of dimers, in contrast to monomers (see Sec.4.1), there is a significant difference between relaxation by diffusion and by desorption. For dimer adsorption, if an adspecies in the interior of a c(2×2) domain is removed by desorption, and if it has all four diagonal neighbors occupied, then an isolated internal defect is created which cannot be (immediately) filled. If an adspecies is removed diagonally adjacent to an internal defect, then dimer adsorption can occur filling both the original internal defect and the site newly opened by desorption. Thus, there is dynamic adsorption-desorption equilibrium of internal defects, in contrast to the model with diffusional relaxation where they are frozen. Domain boundaries have the same structure as for the model with diffusional relaxation discussed in Sec.3.2. However, evolution at these domain boundaries is somewhat different, relaxation via desorption allowing more varied pathways for evolution [25]. Also, the irreversible character of evolution for diffusional relaxation (as discussed in connection with Fig.8) is lost for relaxation via desorption.

For finite lattices of 2L×2L sites with periodic boundary conditions, the system always evolves to a single c(2×2) domain, which includes isolated defects with density $D_\infty(L)>0$, in dynamic equilibrium. Not surprisingly, we find that $D_\infty \approx 0.0747$ depends only weakly on L [25]. Anomalous frozen states including a domain boundary are not possible in this model. Also, it is clear that once the system evolves to a single jammed c(2×2) domain, subsequently adsorption (and thus desorption) will occur only on the sublattice associated with that domain. We exploit this feature below. Thus, in summary, for this model the fractional area of domain boundary, $F=1-2D-2\theta$, will vanish, but the final coverage, ½-

$D_\infty \approx 0.42534$, will remain well below ½. Next, we present simulation results for a large 800×800 site system. Fig.11 shows one snapshot of a portion of a coarsened configuration clearly revealing the "high" density of internal defects. Simulations reveal the scaling behavior (see Fig.12)

$$F=1-2D-2\theta \sim t^{-\alpha}, \text{ where } \alpha \approx 0.47 \text{ for } 15<t<250, \quad (4)$$

suggesting an asymptotic value of $\alpha=1/2$, again consistent with the expected Lifshitz-Cahn-Allen (LCA) type coarsening.

To close this section, we provide an analysis of the density, D_∞, of internal defects in the final state. The above discussion noted that all the "action" within a single domain is on one sublattice for c(2×2) ordering. Thus, to determine D_∞, it is suffices to consider the following "sublattice problem". Start with square grid, which is completely occupied except for isolated defects. Then, randomly remove single adspecies, and immediately adsorb dimers at any adjacent empty pairs of sites thus created. This model evolves through jammed states, with only isolated vacancies, until reaching a dynamic equilibrium where the fraction of vacancies equals $D^*= 0.1493$. One might think of this model as a natural variation of Robert's classic model for RSA of dimers on adjacent sites [9], where the fraction of vacancies in the jammed state on a square lattice is 0.09318 (cf. Sec.1). Finally, one can trivially relate the defect density in the sublattice problem to the defect density of interest in the original problem via $D_\infty=D^*/2=0.0747$. Further discussion of this problem, including some simple estimates of D_∞, can be found in Ref.[25].

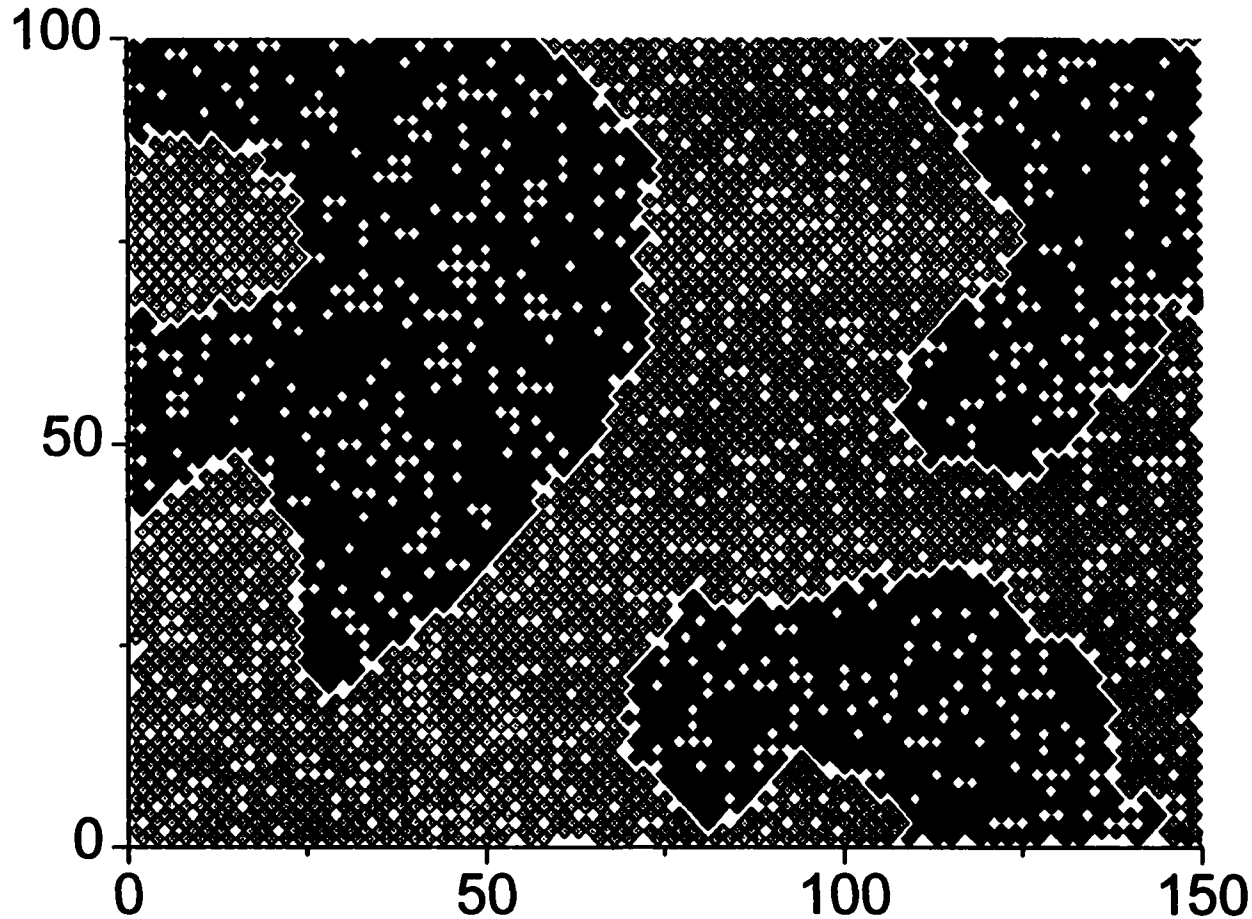

Figure 11. Snapshot of a portion of a coarsened configuration at t=110 for relaxation via desorption in the eight-site model for RSA of dimers. Note the high density of internal defects.

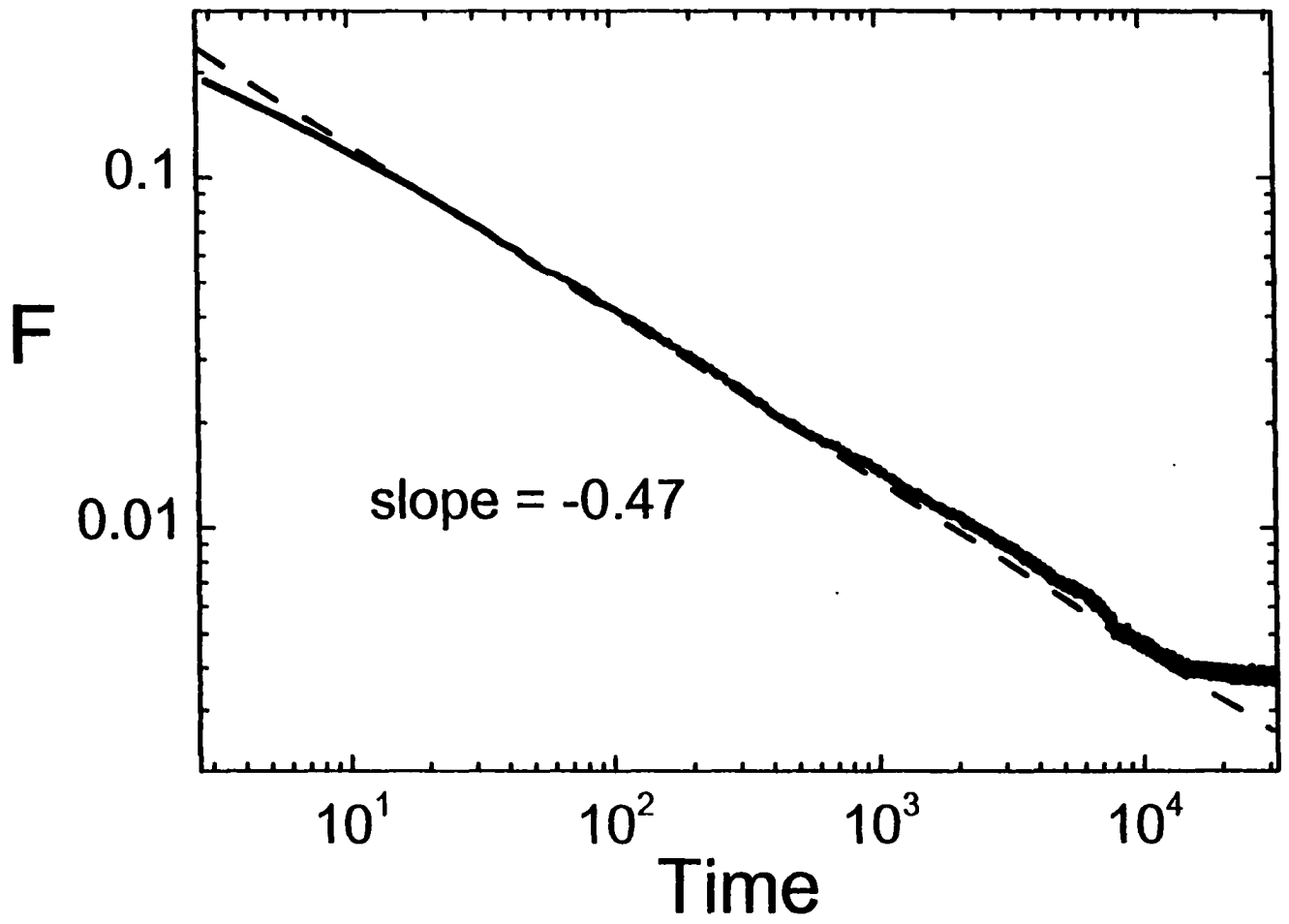

Figure 12. Log-log plot of the decrease of F with t for relaxation via desorption in the eight-site model for RSA of dimers.

5. SUMMARY

In this paper, we have considered the relaxation due to slow diffusion processes, and due to slow desorption or reaction processes, of adlayers formed in RSA models with NN exclusion on a square lattice. These studies were motivated by an interest in relaxation processes in chemisorption systems. For this reason, we relegate to the Appendix, a discussion of the analogous processes on a linear lattice. In all cases, we found coarsening of c(2×2) domains, analogous to Lifshitz-Cahn-Allen coarsening in Hamiltonian systems. Behavior was also consistent to previous observations by Privman and coworkers [11] for a model with "faster" relaxation at a rate comparable to adsorption. For the eight-site model involving dimer adsorption, there is a significant difference between relaxation via desorption and via diffusion. For the former, the internal defects within c(2×2) domains achieve a dynamic equilibrium with a significant non-zero density. For the latter, the defects are frozen, but appear to be annealed away in large systems as a result of the wandering of domain boundaries. Note that the annealing of frozen defects by diffusional relaxation was observed in another RSA model which was equivalent to adsorption of monomers on a square lattice with NN and diagonal NN exclusion [23].

ACKNOWLEDGEMENTS

This work was supported by the Office of Basic Energy Sciences, Division of Chemical Sciences, of the U.S. Department of Energy (USDOE). It was performed at Ames Laboratory, which is operated for the USDOE by Iowa State University under Contract No. W-7405-Eng-82.

APPENDIX: RELAXATION EFFECTS IN RSA ON LINEAR LATTICES

In this Appendix, we present a brief discussion of relaxation for RSA processes on linear lattices, which are the direct analogues of the canonical model and the eight-site model on square lattices.

First, consider the canonical model for RSA with NN exclusion on a linear lattice, which involves irreversible adsorption on momomers on single empty sites provided both neighbors are empty [5]. Thus, an ensemble of three empty sites is required for adsorption. This RSA problem can be solved exactly to determine that $\theta_J = \frac{1}{2}(1-e^{-2}) \approx 0.4323$. Also, this model is actually equivalent to RSA of dimers onto adjacent empty sites. See Fig.13a. Under slow diffusional relaxation, adspecies hop to adjacent empty sites provided no adjacent occupied pairs are thus created. Further adsorption occurs when any triples of empty sites are thus created, and the coverage evolves toward ½. It is easier to visualize this process in the "dimer representation", where after adsorption, dimers slowly hop intact to adjacent empty sites (see Fig.13a). This results in diffusion of isolated vacancies (V), and whenever two reach adjacent sites, they immediately "annihilate" as a result of further dimer adsorption. This type of diffusion-mediated V+V→ "inert" reaction has been studied extensively [30], as has diffusional relaxation of dimer RSA (for a finite ratio of adsorption to diffusion rates) [21]. The basic result is that the concentration of vacancies decreases like $t^{-1/2}$, rather than the mean-field kinetics prediction of t^{-1}. This is easily checked using results for 1D random walks to assess the mean collision time for adjacent V's. Thus, the mean length of double-spaced domains increases like $t^{1/2}$. Relaxation by slow desorption in the RSA model is essentially equivalent to relaxation by diffusion (as in the 2D case).

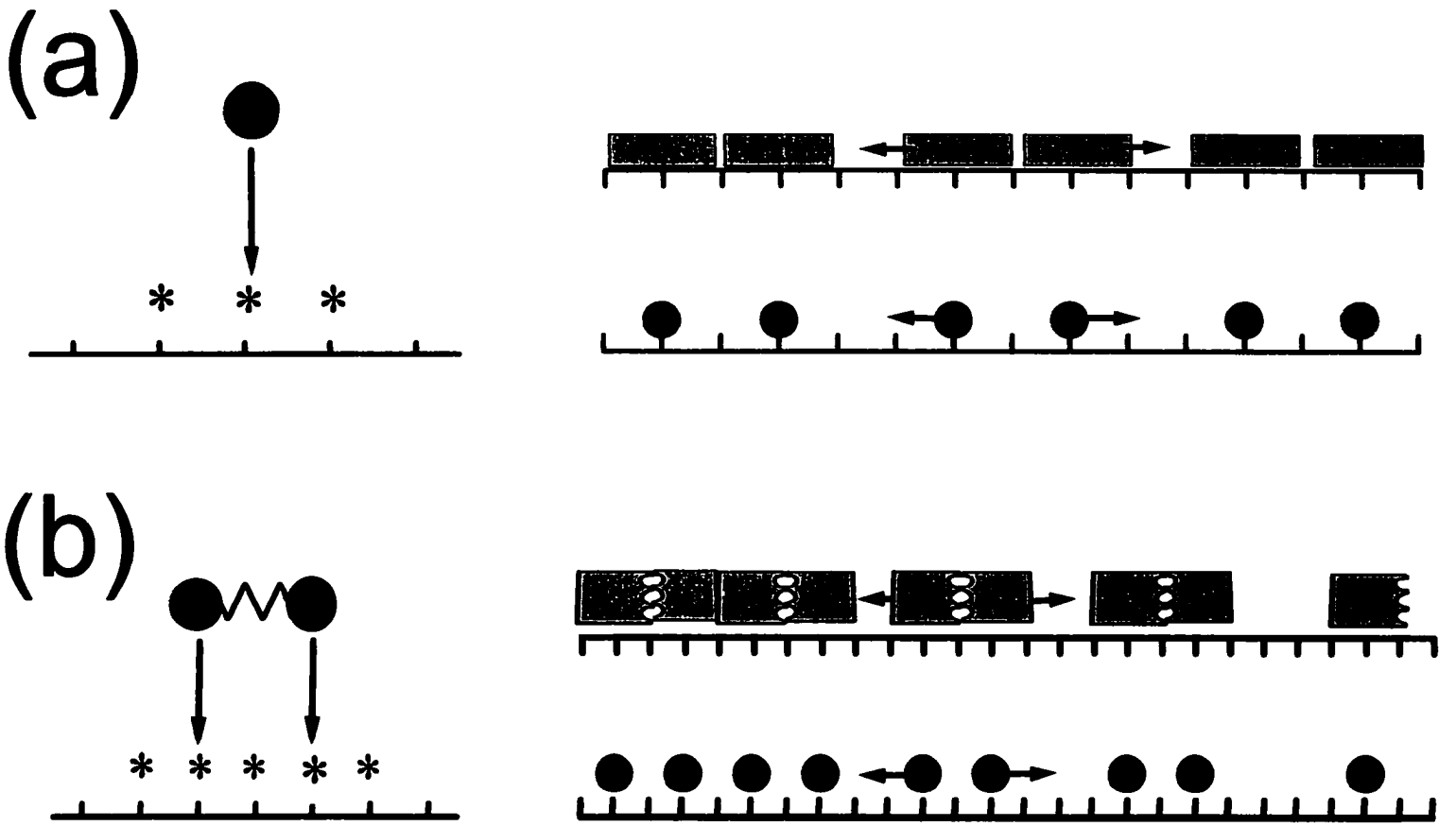

Figure 13. Diffusional relaxation in RSA models on a linear lattice: (a) RSA of monomers with NN exclusion (right), and diffusion processes leading to further adsorption (left). The corresponding "dimer representations" is also shown. (b) The five-site model for RSA of dimers (right), and an example of diffusion processes (left). The corresponding "tetramer representation" is also shown.

Second, consider a "five-site model" for dissociative RSA of dimers onto second NN sites, subject to NN exclusion. Thus, an ensemble of five empty sites is required for adsorption. See Fig.13b. This RSA problem can be solved exactly to determine that $\theta_J \approx 0.4019$ [20]. Also, this five-site model is equivalent to RSA of tetramers onto adjacent quartets of empty sites, where singlet, pairs, and triplets of vacancies (V) remain in the jammed state (Fig.13b). Slow diffusional relaxation occurs in the five-site model by hopping of the constituent atoms in the dissociated dimers to adjacent empty sites, subject to NN exclusion. There are no frozen internal defects, as in the 2D case. In the "tetramer representation", diffusional relaxation corresponds to scission of the tetramers into halves and hopping of the "dimer pieces", which also results in diffusion of the V's (see Fig.13b). Whenever four V's reach consecutive sites, they are "annihilated" by subsequent tetramer deposition. This type of diffusion-mediated $kV \rightarrow$ "inert" reaction has also been considered previously [31], as has the related diffusional relaxation of k-mer RSA (for a finite ratio of adsorption to diffusion rates, and for intact diffusion of the entire k-mers) [11, 32]. The basic conclusion is that for $k>3$, the concentration of vacancies decreases according to the mean-field prediction like $t^{-1/(k-1)}$. Thus, for our model where $k=4$, one should expect a decrease like $t^{-1/3}$, and we have performed simulations to confirm this claim.

Relaxation by slow desorption for this five-site model is distinct from diffusional relaxation, and for long times involves a dynamic adsorption-desorption equilibrium, just as in the 2D case. However, unlike the 2D case, there is no mechanism to promote or maintain population of one of the two sublattices (which here consist of every second site). Thus, coarsening is not induced.

REFERENCES

[1] G.A. Somorjai, Introduction to Surface Chemistry and Catalysis, Wiley, New York, 1994.

[2] W.H. Weinberg, Ann. Rev. Phys. Chem. **34** (1983) 217; K. Binder and D.P. Landau, Adv. Chem. Phys. **26** (1989) 91.

[3] J.D. Gunton and K. Kaski, Surf. Sci. **144** (1984) 290.

[4] H.C. Kang and W.H. Weinberg, Surf. Sci. **299/300** (1994) 755; B. Meng and W.H. Weinberg, J. Chem. Phys. **102** (1995) 9435.

[5] J.W. Evans, Rev. Mod. Phys. **65** (1993) 1281.

[6] See B. Meng and W.H. Weinberg, J. Chem. Phys. **100** (1994) 5280, and references therein.

[7] C.T. Campbell, M.T. Paffett, and A.F. Voter, J. Vac. Sci. Technol. A **4** (1986) 1342.

[8] M.C. Bartelt and V. Privman, Int. J. Mod. Phys. **B5** (1991) 2883.

[9] J.K. Roberts, Nature **135** (1935) 1037; Proc. Roy. Soc. A **152**(1935) 473; **161**, (1937) 141; Proc. Camb. Phil. Soc. **34** (1938) 399.

[10] C.K. Gan and J.-S. Wang, J. Chem. Phys. **108** (1998) 3010.

[11] V. Privman, in D. Stauffer (Ed), Annual Reviews of Computational Physics III, World Scientific, Singapore, 1995, p.177.

[12] F.H. Ree and D.A. Chesnut, J. Chem. Phys. **45** (1996) 3983.

[13] R.Q. Hwang, E.D. Williams, N.C. Bartelt, and R.L. Park, Phys. Rev. B **37** (1988) 5870.

[14] D.J. Dwyer, G.W. Simmons, and R.P. Wei, Surf. Sci. **64** (1977) 617.

[15] J.W. Evans, D.R. Burgess, and D.K. Hoffman, J. Chem. Phys. **79** (1983) 5011.

[16] J.W. Evans and D.E. Sanders, Phys. Rev. B **39** (1989) 1587.

[17] C.R. Brundle, R.J. Behm, and J.A. Barker, J. Vac. Sci. Technol. A **2** (1984) 1038.

[18] S.-L. Chang and P.A. Thiel. Phys. Rev. Lett. **59** (1987) 296.

[19] S.-L. Chang, D.E. Sanders, J.W. Evans, and P.A. Thiel, in J.F. van der Veen and M.A. Van Hove (Eds), The Structure of Surfaces II, Proc. of the 2nd International Conference on the Structure of Surfaces (ICSOS II), Amsterdam, 22-25 June 1987, Springer, Berlin, 1988, p.231.

[20] J.W. Evans, J. Chem. Phys. **87** (1987) 3038.

[21] V. Privman and P. Nielaba, Europhys. Lett. **18** (1992) 673.

[22] J.-S. Wang, P. Nielaba, and V. Privman, Mod. Phys. Lett. B **7** (1993) 189.

[23] J.-S. Wang, P. Nielaba, and V. Privman, Physica A **199** (1993) 527.

[24] R. Imbihl, Prog. Surf. Sci. **44** (1993) 185.

[25] E.W. James, C. Song, and J.W. Evans, J. Chem. Phys. (1999) submitted.

[26] Y. Suchorski, J. Beben, E.W. James, J.W. Evans, and R. Imbihl, Phys. Rev. Lett. **82** (1999) 1907.

[27] V. Zhdanov and B. Kasemo, Surf. Sci. **412/413** (1998) 527.

[28] S.M. Allen and J.W. Cahn, Acta. Mat. **27** (1979) 1085; I.M. Lifshitz, Sov. Phys. (JETP) **15** (1962) 939.

[29] Da-Jiang Liu, E.W. James, and J.W. Evans, J. Chem. Phys. (1999) to be submitted.

[30] V. Kuzovkov and E. Kotomin, Rep. Prog. Phys. **51** (1988) 1479.

[31] K. Kang, P. Meakin, J.H. Oh, and S. Redner, J. Phys. A **17** (1984) L665.

[32] P. Nielaba and V. Privman, Mod. Phys. Lett. B **6** (1992) 533.

CHAPTER 6. GENERAL CONCLUSIONS

Monte-Carlo simulations of stochastic models can be successfully used to describe cooperative behavior in a variety of complex systems in physics, chemistry or biology. In particular, for this thesis, we use Monte Carlo simulations to describe catalytic surface reactions of a lattice gas model. We have studied such issues as the system's steady-state behavior; phase diagrams; spatial and time correlations; and fluctuations.

We incorporate the relatively new eight-site rule into our lattice-gas model studies, as well as rapid CO-diffusion. Although our model is still rather simplistic, it does incorporate some basic features of real systems, neglected in previous models. In particular, the eight-site rule causes the commonly observed superlattice ordering of adsorbed oxygen and reflects the strong repulsive short-range adspecies interactions. We also have eliminated the unrealistic feature of oxygen poisoning, for very low P_{CO} deposition rate. In addition, applying the eight-site rule yielded a new feature for the catalytic surface reaction model, which we refer to as symmetry-breaking. Finally, we successfully applied our model to elucidate the fluctuation behavior observed in CO-oxidation on a nanoscale Pt field-emitter tip.

ACKNOWLEDGEMENTS

This work was supported by the Division of Chemical Sciences, Office of Basic Energy Sciences, of the U.S. Department of Energy (USDOE). It was performed at Ames Laboratory, which is operated for the USDOE by Iowa State University under contract No. W-7405-Eng-82.

The U.S. Government has assigned a DOE Report Number IST-1879 to this thesis.